In-Beam Electron Spectroscopy of ^{254}No and ^{226}U in Conjunction with a Gas-Filled Recoil Separator

Thesis submitted in accordance with the requirements of the
University of Liverpool for the degree of Doctor in Philosophy
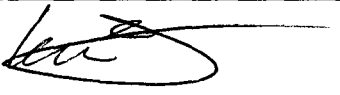
by

Richard David Humphreys

Oliver Lodge Laboratory

May 2003

To my family

Abstract

Construction of the new collinear geometry, conversion electron spectrometer SACRED was started September 1999 at the University of Jyväskylä, Finland. The spectrometer was built to replace the previous *recoil shadow* SACRED configuration. The new spectrometer was designed to meet the problems associated with the old SACRED spectrometer, those being; Doppler broadening of of line shape and the lack of a recoil tagging capability. In August 2000 the first commissioning tests of SACRED in conjunction with RITU were carried out. No serious technical difficulties were encountered and tests showed that prompt electron spectroscopy at a cross-section of 2 μbarns was possible. During 2000-2002, SACRED was utilised in a number of experiments to identify previously unseen transitions in ^{226}U and ^{254}No. This thesis details the analysis and results of those experiments and also the construction and operation of the SACRED spectrometer.

Excited yrast states in the neutron deficient nuclei ^{226}U and ^{254}No have been identified using the SACRED electron spectrometer used in conjunction with the RITU gas-filled recoil separator in three experiments performed at the Accelerator Laboratory of the University of Jyväskylä, Finland.

The energy of the $2^+ \rightarrow 0^+$ transition in ^{226}U has been measured as 81.3(6) keV and the energy of the $4^+ \rightarrow 2^+$ transition in ^{254}No has been measured as 101.1(4) keV, both for the first time, by means of electron spectroscopy. The results are close to the Harris parameter predictions of these transitions from earlier γ-decay work. Absolute values of electromagnetic decay intensities have been measured for yrast transitions in both nuclei. An unidentified peak has also been observed in the prompt conversion electron spectrum with an energy of $\approx$ 112 keV. The ^{254}No experiment also revealed a striking feature in the form of a broad distribution that peaks near 100 keV and comprises high multiplicity electron cascades, probably originating from $M1$ transitions within rotational bands built on high K states.

Acknowledgements

Firstly, I would like to thank Professor P.J. Nolan for giving me the opportunity to study at the University of Liverpool.

Thanks to my supervisor, Professor P.A. Butler for his help and patience. I would also like to thank Dr. R.-D. Herzberg and Dr. G.D. Jones for their help with many aspects of my work.

For proof-reading this thesis I would like to thank Dr.'s R.-D. Herzberg, A. Keenan, G.D Jones and M.J. Taylor.

Thanks to the hospitable students and staff at the University of Jyväskylä, Funland.

Thanks to the computer support staff at Liverpool.

Thanks to Anthony Melarangi, Tom Page, Joe Bastin, Matt Ball, Rich Sloane, Mike Taylor, Alex Keenan, Chris Fox, Cath Scholey and last and by all means least Aled Evans, for all the laughs.

Thanks to all the other students past and present

Cheers to the lads for all the games of phooty.

Finally, I gratefully acknowledge the financial support provided by the Engineering and Physical Sciences Research Council (EPSRC).

Contents

Chapter 1

Introduction

One of the driving forces of experimental nuclear physics is the discovery of new elements and the observation of their characteristics. Nuclei with $Z > 100$ (transfermium nuclei), are at the limit of Coulomb instability, and were it not for the sizable fission barrier of up to 8 MeV [So 94, Mö 94, Sm 95], afforded by the large shell correction energy, these nuclei would be unstable against spontaneous fission. Indeed the very existence of these very heavy elements is a striking example of the shell structure in nuclei which is responsible for the proposed [Ni 68] island of stability of superheavy elements at around $Z = 114$, $N = 184$. Thus large nuclei (transfermium) which are only stable as a result of the shell correction energy are characterised as belonging to the family of superheavy nuclei.

1.1   Superheavy Nuclei

There are many calculations on the location and properties of the next magic number nuclei. Calculations based on the Strutinsky [St 67] shell-correction method has led to a series of papers [MS 66, Ni 68, FN 72, Ra 76] which are in general agreement that $N = 184$ is the next neutron magic number; but for protons both $Z = 114$ and 126 are proposed as magic numbers, although more recent work based on the Strutinsky approach, favours $Z = 114$ [So 94, Mö 94, Sm 95]. In contrast, calculations based on the

relativistic mean field predict magic proton numbers: $Z = 120$[Ru 97] and 126[Cw 96] (see [Be 03] for review). Figure 1.1 illustrates these differences in the various magic number calculations. Predicted half-lives, based on the various calculations, differ by many orders of magnitude and some even predict half-lives approaching the age of the Universe, which points to the possibility of naturally occurring superheavy elements. Terrestrial and extraterrestrial materials have been investigated with no positive results and attempts to produce the predicted doubly magic nucleus $^{298}114$ using heavy-ion reactions [Og 78, Ar 85] have also been unsuccessful. This lack of success was thought to be the result of either too small a cross-section or too long or short half-lives. As production and detection techniques have steadily improved over the years, the search for superheavy nuclei away from the doubly closed neutron and proton shells has led to the discovery of many new superheavy elements. A time line charting this progress can be seen in figure 1.2.

1.2 Spectroscopy of Superheavy elements

It is clear that understanding the structure of the superheavy elements is essential for the development of the mean field theories that are used to predict nuclear properties far from stability. There are a number of experimental sources offering insight into the structure of superheavy nuclei. This can be obtained by direct measurement of the ground state properties of nuclei (see [Ho 00] for review). Equally important information can come from the study of mid-shell deformed nuclei since selected single particle orbits that lie close to the spherical shell gap in superheavy nuclei are close to the Fermi level in nuclei having large quadrupole deformation. Such information can come from radioactive decay spectroscopy or in-beam spectroscopy and the development of recoil separators for use with γ-ray detector arrays has meant that, in recent years, in-beam spectroscopy has been used for such studies. Using Recoil-Decay-Tagging (RDT), a process whereby the prompt decay process at the target, is tagged by detection of the α decay from the recoil in the focal plane of a recoil
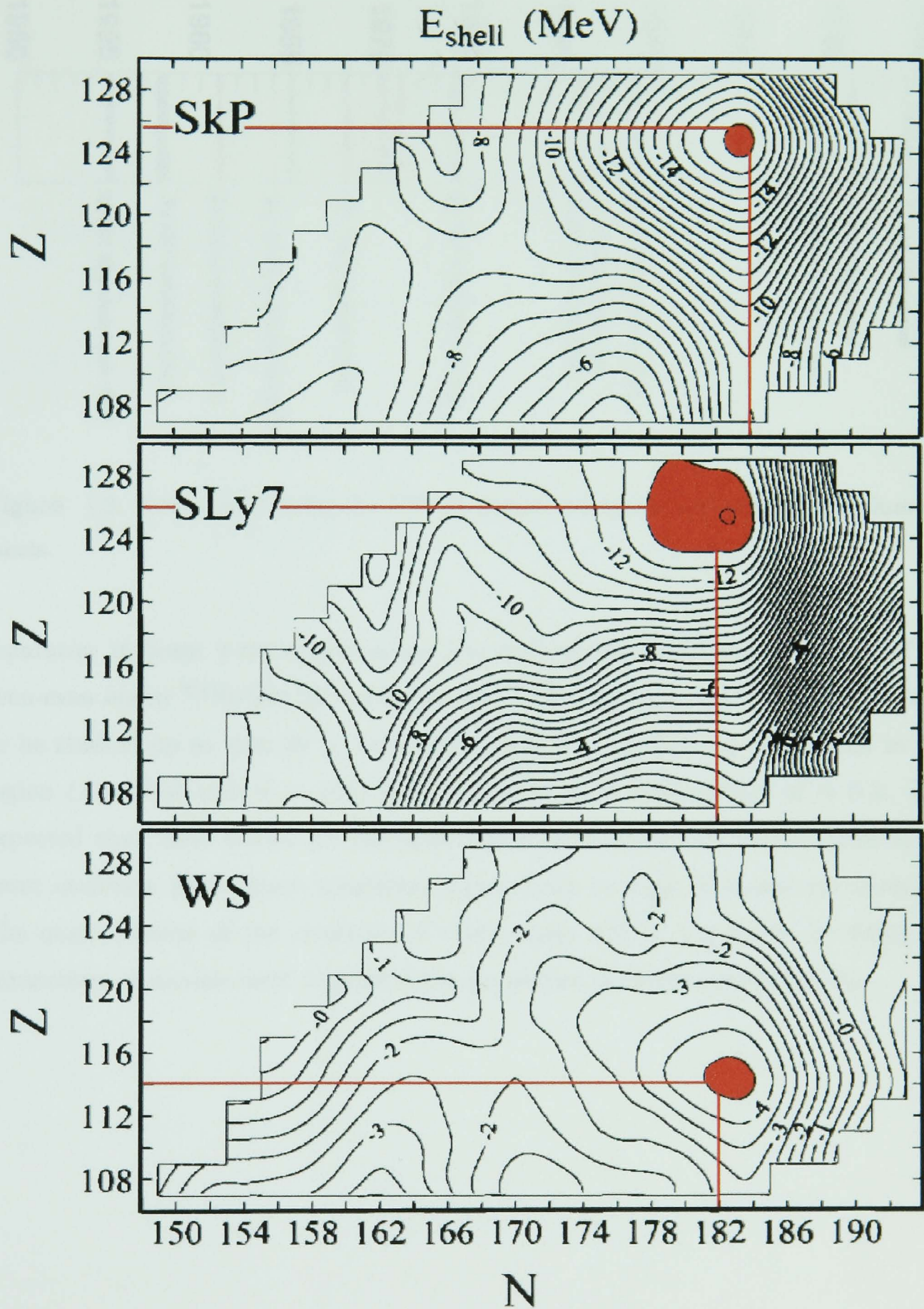
Figure 1.1: Shell energy plots for the superheavy region with positions of highest stability shown in red. SkP and SLy7 are Hartree-Fock calculations and WS is based on deformed Woods-Saxon calculations [Cw 96].
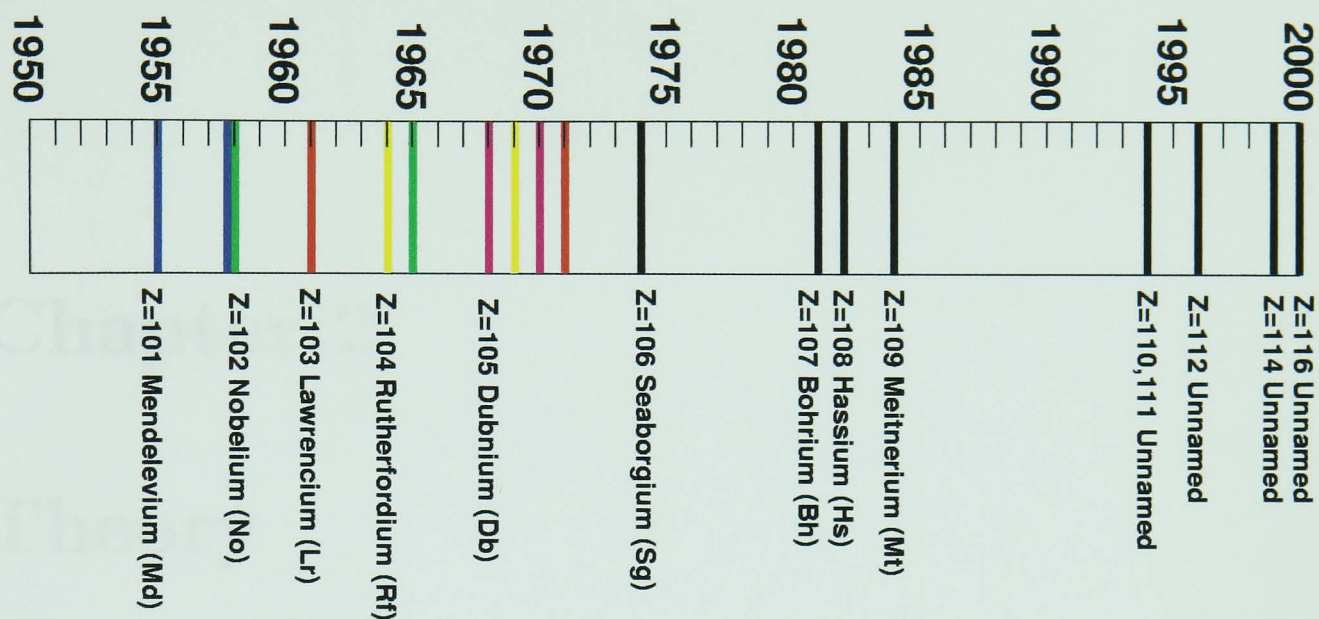
Figure 1.2: Time-line showing the IUPAC names and symbols of the transfermium elements.

separator, in-beam γ-ray spectroscopy has enabled the rotational behaviour of the even-even nuclei ^{254}No [Re 99, Le 99, Re 00], ^{252}No [He 02a] and ^{250}Fm [Ba, He 02b] to be studied up to spin 20 $\hbar$, while also confirming predictions that nuclei in this region ($Z \approx 100$ and $N \approx 150$) have a ground state deformation of ≈ 0.3. It is expected that these nuclei are the homologues of neutron rich Er-Hf nuclei in the lower oscillator shell where rotational bands built on high K states are observed. The quantification of the structure of these states will be important for fixing the parameters of models used to predict the properties of superheavy elements.

Chapter 2

Theory

2.1 The Shell Model

While the liquid drop model is successful at describing bulk nuclear properties, such as the variation in nuclear mass and the fission process, it is a classical macroscopic model and fails to account for anomalies such as discontinuities in neutron binding energy as a function of mass.

Having proved successful in explaining many details of atomic structure, the shell model was adapted to describe the nucleus. The shell model treats nucleons individually under the basic assumption that a single nucleon moves in a smooth potential well which is created by all the other nucleons in the nucleus. This assumption is permitted by the Pauli exclusion principle which prevents a nucleon having the same quantum state as another, thus allowing the nucleons to complete orbits by restricting them from orbit destroying collisions.

The shell model Hamiltonian can be represented by:

$$H = \sum_{i=1}^{A} \left[-\frac{\hbar^2}{2m} \nabla_i^2 + V(r_i) \right],$$

where the first term represents the kinetic energy of the individual nucleons and the second term represents the potential. There are several potentials available to describe the nuclear potential, these include the square well potential, the harmonic
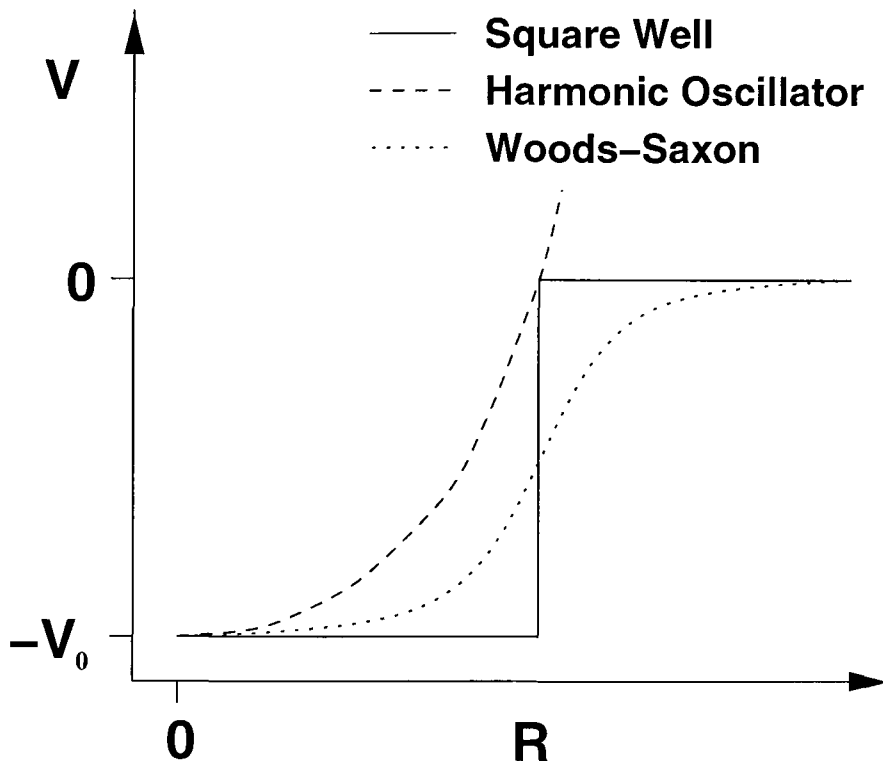
Figure 2.1: Comparison of the square well potential, harmonic oscillator potential and Woods-Saxon potential.

oscillator and the Woods-Saxon potential, all of which are represented in figure 2.1.

The Woods-Saxon [WS 54] potential is able to reproduce the magic numbers for low mass nuclei, and is expressed as:

$$V(r) = \frac{-V_0}{1 + exp\left(\frac{r-R}{a}\right)},$$

where a is a diffuseness parameter that determines how sharply the potential increases to zero and R is the radius at which $V(R) = -V_0/2$, where V_0 defines the depth of the potential. To account for higher shell closures a non central term must be added. With the addition of the spin orbit interaction the correct magic numbers are reproduced.

2.1.1 Spin-Orbit Interaction

As stated in the previous section 2.1, the Woods-Saxon potential only reproduces the magic numbers for low mass nuclei. To reproduce the higher magic numbers,

Mayer [Ma 49] and Haxel, Jensen and Suess [HJS 49], proposed, based on analogies with atomic systems, that a spin orbit interaction should be added to the nuclear potential. Hence the nuclear potential is modified to give the following:

$$V(r) \rightarrow V(r) + f(r)\mathbf{l}.\mathbf{s},$$

where $\mathbf{l}$ is the orbital angular momentum, $\mathbf{s}$ is the intrinsic spin angular momentum and $f(r)$ is the strength of the spin orbit coupling. The spin orbit interaction has the effect of splitting otherwise degenerate levels as a single nucleon has $s = \pm\frac{1}{2}$; therefore, $j = l \pm \frac{1}{2}$ (where j is the total angular momentum). Now each j state can hold $2j + 1$ identical particles, allowing the Woods-Saxon potential, used in conjunction with the spin-orbit potential, to predict the magic numbers for spherical nuclei.

2.2   Deformation

For nuclei to rotate they must be non-spherical so that they have an axis to rotate about. For deformed nuclei, assuming a constant nuclear volume, the nuclear surface is defined by a radius vector pointing from the origin to the surface and can be described by:

$$R(\theta, \phi) = C(\alpha_{\lambda\mu})R_0 \left[1 + \sum_{\lambda=1}^{\infty} \sum_{\mu=-\lambda}^{\lambda} \alpha_{\lambda\mu} Y_\lambda^\mu(\theta, \phi) \right],$$

where R_0 is the radius of a sphere of the same volume as the deformed nucleus, $\alpha_{\lambda\mu}$ are the coefficients of the spherical harmonics $Y_\lambda^\mu(\theta, \phi)$ and the factor $C(\alpha_{\lambda\mu})$ satisfies the volume conservation condition.

2.3   Pairing

The pairing interaction is a shell model refinement which is necessary to explain the experimental observations given below:

- The ground state spins and parities of all even-even nuclei are $I^\pi = 0^+$ which points to the presence of a force that couples nucleons pairwise, thus cancelling their angular momenta;

- Non-collective excitation energies of even-even nuclei show an energy gap approximately 1.5 MeV higher than in odd mass nuclei;

- Nuclear moments of inertia are systematically lower than the expected rigid body values at low spin, suggesting the nucleus may behave like a superfluid;

- The binding energies of odd-even nuclei are less than the average of the two neighbouring even-even nuclei, and the binding energies of odd-odd nuclei are even lower;

- The spin of the last nucleon determines the ground state spin of odd mass nuclei.

The pairing force describes the short range characteristics of the nuclear force between identical nucleons in the same j orbit. The pairing interaction V_{pair} can be expressed by [Ca 90]:

$$\langle j_1 j_2 J | V_{pair} | j_3 j_4 J' \rangle = -G\sqrt{\left(j_1 + \frac{1}{2}\right)\left(j_3 + \frac{1}{2}\right)}\delta_{j_1 j_2}\delta_{j_3 j_4}\delta_{J0J'0}, \qquad (2.1)$$

where $\mathbf{J}$ and $\mathbf{J'}$ are the intrinsic angular momentum vectors formed by coupling the angular momentum vectors of the two nucleons before and after the interaction respectively, G is the strength of the interaction and the subscripts refer to nucleon orbit labels. Thus it can be seen that the pairing interaction is only effective for like nucleons in equivalent orbits. The pairing interaction strength, G, is dependent upon the spatial overlap of the two nucleons and is greater for high j orbits. Therefore as nuclear mass increases the strength of the pairing force decreases as a consequence of the increased distance between the outer nucleons. The strength of the pairing force is also lower for protons due to Coulomb repulsion.

2.3.1 Pairing effects on the Fermi Surface

An important feature of the pairing interaction is that pairs of nucleons in an orbit, j, coupled to $J^\pi = 0^+$, can be *scattered* into another orbit, j' , as a pair such that they are always in time reversed orbits with $J^\pi = 0^+$. Deep below the Fermi surface scattering is forbidden by the Pauli principle as the orbits above j are filled; however, near the Fermi surface there is the probability that some of the orbits are unoccupied and scattering can occur. Now a particle can be found in more than one shell creating partial occupation near the Fermi surface. Without pairing, orbits would be filled sequentially until all the nucleons had been placed in the lowest orbits to give a sharply defined Fermi surface; but as a result of the scattering facilitated by the pairing interaction, the Fermi surface is *smeared*, as illustrated in figure 2.2.

The smearing of the Fermi surface leads to the concept of quasi-particles [Ba 57, Bo 58], which can be considered as a combination of particle and hole states. The quasi-particle energy is defined by:

$$E_i = \sqrt{(\epsilon_i - \lambda)^2 + \Delta^2},$$

and the occupation probability of a state i by a hole or a particle is given by:

$$U_i = \frac{1}{\sqrt{2}} \left[1 + \frac{(\epsilon_i - \lambda)}{\sqrt{(\epsilon_i - \lambda)^2 + \Delta^2}} \right]^{\frac{1}{2}},$$

$$V_i = \frac{1}{\sqrt{2}} \left[1 - \frac{(\epsilon_i - \lambda)}{\sqrt{(\epsilon_i - \lambda)^2 + \Delta^2}} \right]^{\frac{1}{2}},$$

where U_i^2 is the probability that the orbit i is occupied by a hole and V_i^2 is the probability that it is occupied by a particle. ϵ_i, λ and Δ are the single particle energy, Fermi energy and pair gap parameter respectively. The probabilities are normalised such that $U^2 + V^2 = 1$ and the pair gap parameter Δ and the number of particles n can be related to particle and hole occupation probabilities by:

$$\Delta = G \sum_i U_i V_i,$$
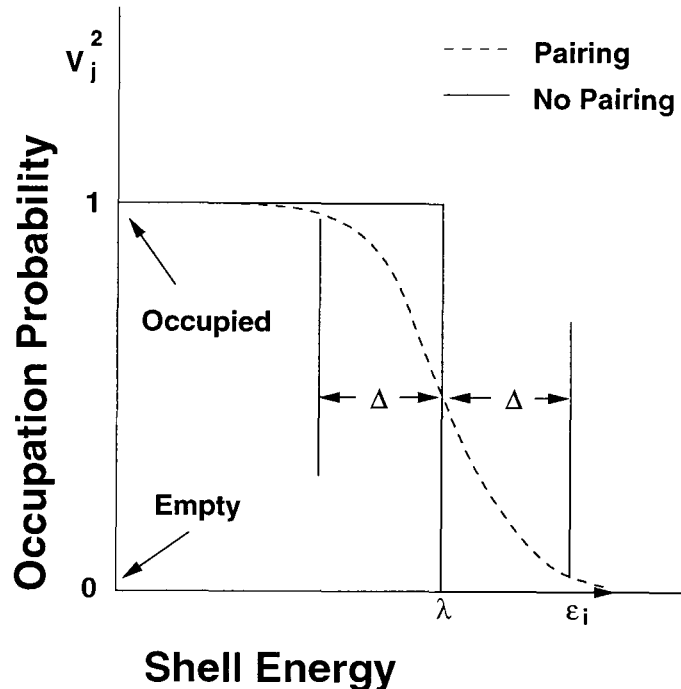
Figure 2.2: Illustration showing the smearing of the Fermi surface due to the pairing interaction.

$$n = 2 \sum_i V_i^2.$$

2.4 K-Isomers

K-isomers occur in mass regions where both neutron and proton orbitals have a large spin projection, Ω, on the symmetry axis near the Fermi surface. The result of the large spin projections is the creation of intrinsic multi-quasiparticle states with aligned spins, K, which are able to compete with collective rotational states in the production of angular momentum. The prolate deformed nucleus ^{254}No has high Ω single particle levels near the Fermi surface for both neutrons near $N = 150$ and protons near $Z = 100$; through broken pair excitations these high Ω values can add up to give high K values. For prolate nuclei the total angular momentum vector has a small projection on the rotation axis which can move about the symmetry axis,

thus conserving K, see figure 2.3. The K-isomerism arises from selection rules for K and a transition is allowed if:

$$\Delta K \leq \lambda,$$

where λ is the multipolarity of the transition. For a given transition the degree of K-forbiddenness, ν is given by:

$$\nu = \Delta K - \lambda.$$

Increased K-forbiddenness leads to increased lifetimes of the states and it has been shown empirically that for each degree of K-forbiddenness increase, the lifetime of the state increases by a factor of 20 [Lö 68]. To allow the comparison of different energies and K-forbiddenness, an expression for hindrance per degree of K-forbiddenness is defined as [WD 01]:

$$f_\nu = \left[\frac{t_{\frac{1}{2}}^\gamma}{t_{\frac{1}{2}}^W} \right]^{\frac{1}{2}} = [F_W]^{\frac{1}{\nu}},$$

where $t_{\frac{1}{2}}^\gamma$ is the partial γ-ray half-life and $t_{\frac{1}{2}}^W$ is the Weisskopf single particle estimate.

2.5 Magnetic Dipole Moments and g-factors

Gyromagnetic factors (g-factors) are coefficients affecting the magnetic dipole moment and indicate in which orbit individual nucleons reside. For a band built on a multi-quasiparticle state the intrinsic g-factor, g_K, is given by the following equation:

$$K g_K = \sum (g_\Lambda \Lambda + g_\Sigma \Sigma),$$

where Λ and Σ are the orbital angular momentum and intrinsic spin projections on the symmetry axis respectively. g_Λ and g_Σ are the associated g-factors, g_Σ is 1 for protons and 0 for neutrons and G_Σ^{free} is -3.83 for neutrons and 5.59 for protons. G_Σ^{free} is attenuated from the free values by a factor of ≈ 0.6 [Wa 94].
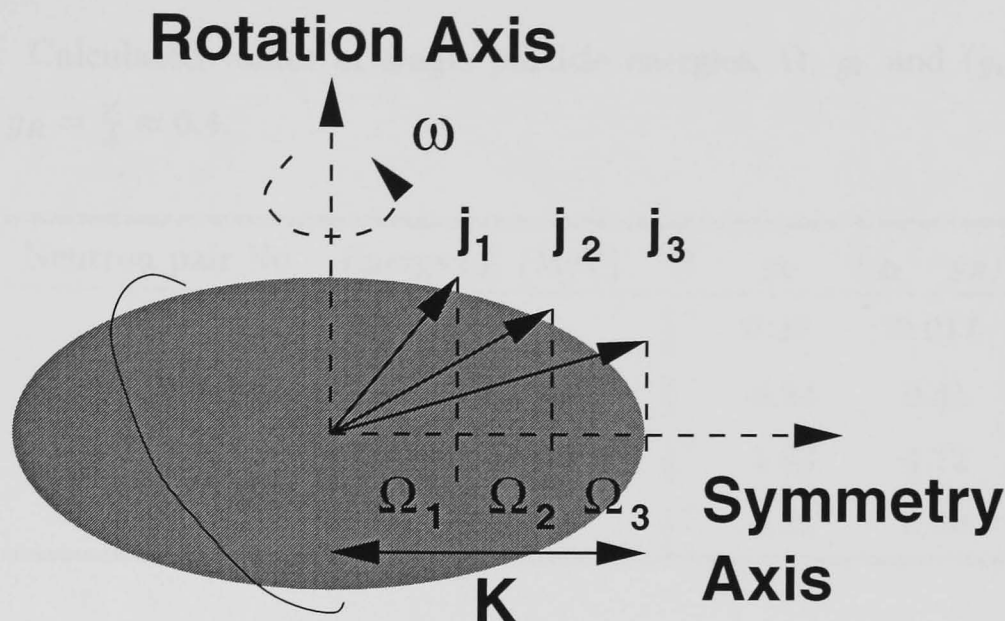
Figure 2.3: Diagram showing how projections of j on symmetry axis add to give K.

In order to model the high K bandheads in the SOLENOID Monte Carlo simulation code (see section 2.6) it is necessary to identify possible quasiparticle configurations and extract their associated g_K. From the Nilsson [Ni 69] single particle level scheme the 149th, 151st and 153rd neutrons, close to the Fermi surface, occupy the $\frac{7}{2}^+[624]_\nu$, $\frac{9}{2}^-[734]_\nu$ and $\frac{7}{2}^+[613]_\nu$ levels, respectively: the order of which is supported by the the work of Braid *et al.* [Br 71], on single particle states in odd-mass Cm isotopes. Table 2.1 shows the information used in the SOLENOID Monte Carlo simulation (see section 2.6) obtained from Woods-Saxon cranking codes [Na 85, Cw 87]. For protons it is apparent that the 101st and 103rd protons, close to the Fermi surface, are in the orbitals $\frac{7}{2}^-[514]_\pi$ and $\frac{9}{2}^+[624]_\pi$ respectively (see figure 2.4). Looking to the Nilsson diagrams for protons and neutrons in figures 2.4 and 2.5, it is clear that the high K states which are observed around the Fermi surface for $Z = 102$ ($\frac{7}{2}^-[514]_\pi$ and $\frac{9}{2}^+[624]_\pi$) are not present for neutrons at $N = 102$. Instead, because of the difference in configurations between the $1i_{\frac{13}{2}}$ and $2f_{\frac{7}{2}}$ orbitals in protons and neutrons, the homologue for neutrons is found at $N = 106$. Here the $\Omega = \frac{7}{2}$ and $\frac{9}{2}$ orbits lie close to the Fermi surface, giving a $K = 8$ two-quasiparticle combination.

Table 2.2 shows the information used in the SOLENOID Monte Carlo simulation.

Table 2.1: Calculated values of single particle energies, Ω, g_k and $(g_k - g_R)^2$, for neutrons. $g_R = \frac{Z}{A} \approx 0.4$.

Neutron pair No.	Energy$_{S.P.}$ (MeV)	Ω	g_k	$(g_k - g_R)^2$
75	-7.96	$\frac{7}{2}^+$	0.27	0.017
76	-7.53	$\frac{9}{2}^-$	-0.24	0.41
77	-6.44	$\frac{1}{2}^+$	-1.63	4.12
78	-6.34	$\frac{7}{2}^+$	-0.31	0.50

Table 2.2: Calculated values of single particle energies, Ω, g_k and $(g_k - g_R)^2$, for protons. $g_R = \frac{Z}{A} \approx 0.4$.

Proton pair No.	Energy$_{S.P.}$ (MeV)	Ω	g_k	$(g_k - g_R)^2$
52	-2.81	$\frac{7}{2}^-$	0.64	0.057
53	-2.30	$\frac{9}{2}^+$	1.29	0.79

Using the generalised Landé formula, see equation 2.3, values of g_K are calculated for the relevant lowest two quasiparticle configurations, for both protons and neutrons, and tabulated in 2.3.

$$g_K = \frac{g_1 + g_2}{2} + \frac{g_1 - g_2}{2} \left[\frac{j_1(j_1 + 1) - j_2(j_2 + 1)}{J(J + 1)} \right]. \tag{2.3}$$

2.6 SOLENOID Monte Carlo Simulation

In order to model the aspects of the SACRED detector and magnetic transport, namely the trajectory and momentum of the electrons and their interaction with the detector, a computer simulation code was used.
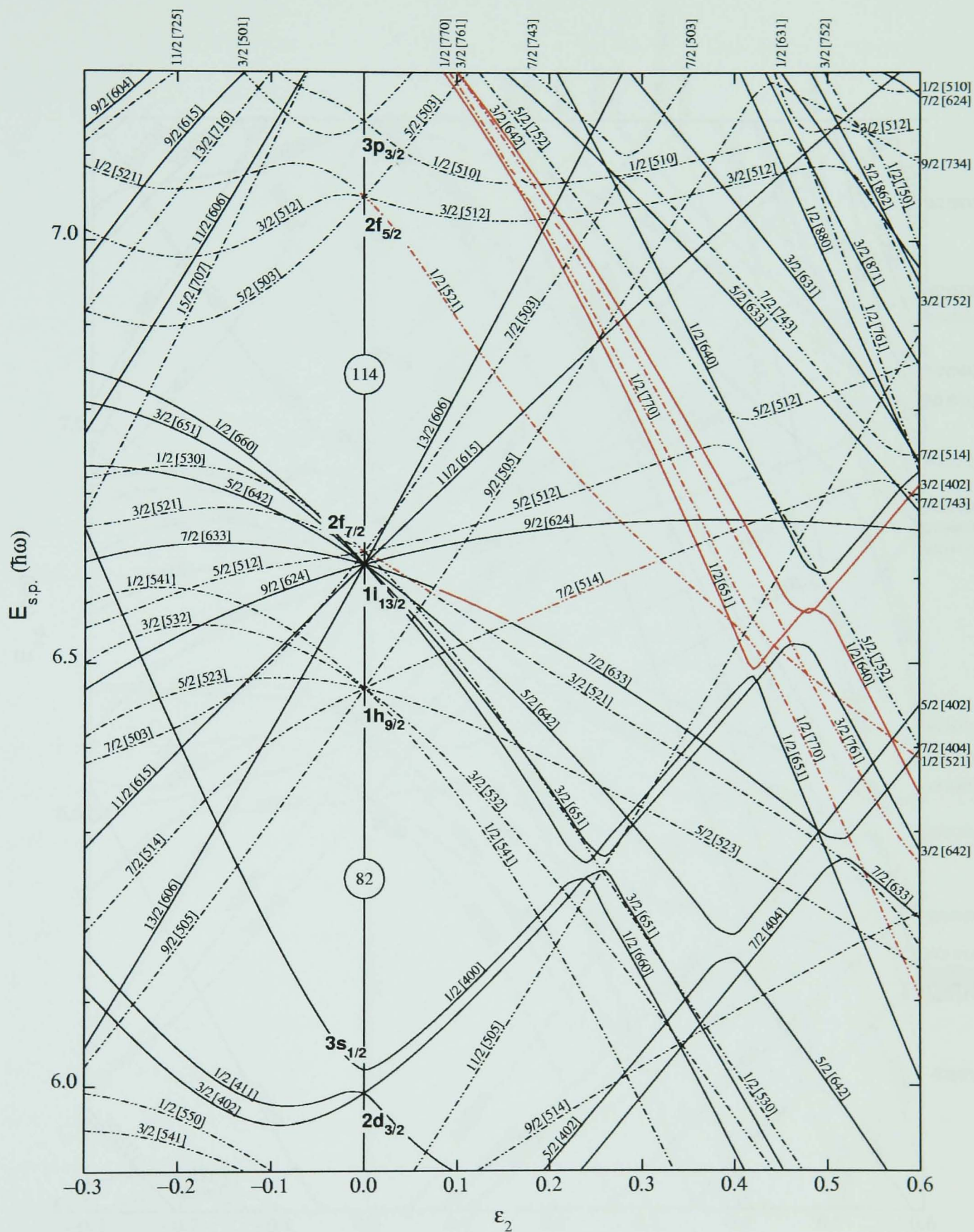
Figure 2.4: Nilsson diagram for protons, single particle orbitals that lie close to the Fermi level for ^{254}No are shown in red.
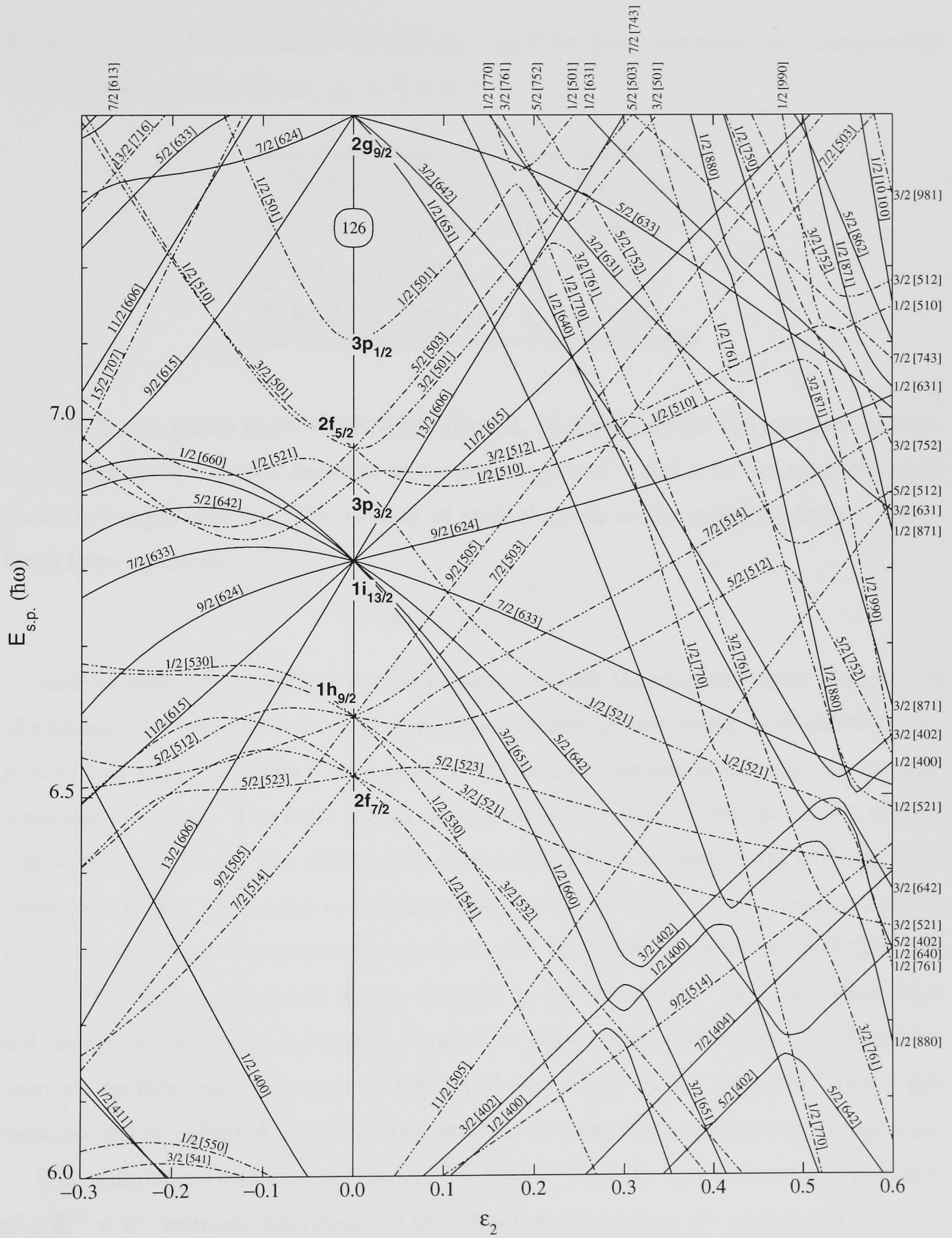
Figure 2.5: Nilsson diagram for neutrons, 82≤N≤126.

Table 2.3: Calculated values of g_k and $(g_k - g_R)^2$ for most probable two-quasiparticle ^{254}No isomer configurations. $g_R = \frac{Z}{A} \approx 0.4$.

Isomer Config.	g_k	$(g_k - g_R)^2$
$\frac{9}{2}^-[734]_\nu \otimes \frac{7}{2}^+[613]_\nu$	-0.3	0.45
$\frac{9}{2}^-[734]_\nu \otimes \frac{7}{2}^+[624]_\nu$	0	0.17
$\frac{9}{2}^+[624]_\pi \otimes \frac{7}{2}^-[514]_\pi$	1	0.37

The Monte Carlo code SOLENOID [Bu 92, Jo 93] simulates the emission of electrons from defined initial energies at random angles of θ and ϕ to the magnetic field from the target position. The motion of each electron in the magnetic field is calculated from equation:

$$F = -e(v \times B),$$

and is evaluated over the entire path taken through the magnetic field. Simulation of multiple electron cascades is of particular interest in this work; each electron trajectory can either be defined as a single event or as a cascade of electrons in a single simultaneous event. The code is also capable of simulating the detector array and its response to electrons. The differential cross section for the interaction between electrons and Si [Ku 75] is used to calculate the path of electrons in the detector, which when coupled with the empirical expression for the range of electrons in Si [Ka 95], enables the energy deposited by the electron to be calculated. This can either be a full energy deposition in a detector element, or backscatter (see section 4.7) from the detector surface into the magnetic field, and depending on the trajectory, either the electron can be reflected back onto the detector or away from the detector completely.

The simulation was used to model ^{226}U and ^{254}No with and without the presence of a $K^\pi = 8^-$ isomeric bandhead. The following parameters are required to run the simulation for e.g. ^{254}No :

- Detector resolution;

- Direct population intensities of states;

- γ-ray transition energies;

- Single particle magnetic moment g_K;

- Rotational g-factor g_R;

- Electric quadrupole moment Q_0;

- Maximum spin Ω;

- Minimum spin for $K^\pi = 8^-$ bandhead population;

- Static moment of inertia $\mathcal{J}$.

The simplest ^{254}No model is to assume that only the ground state band is populated, so that there is no other source of conversion electrons. The simulation uses the γ-ray transition energies and intensities from Reiter *et al.* [Re 99] and Leino *et al.* [Le 99] and conversion coefficient tables from Rösel *et al.* [Rö 78] to produce a conversion electron spectrum.

A more complex ^{254}No model is to assume that not only is the ^{254}No ground state band populated; but, other excited states with high-K bandheads. A $K^\pi = 8^-$ bandhead is modelled as a source of conversion electrons, which can be set as either isomeric or non-isomeric. The code requires the input of the minimum spin for which the bandhead is populated, and the population intensity of the bandhead. The energies of the excited states within the band are calculated using equation 2.4 and the energies are then randomised by applying a Gaussian distribution of $\sigma = 10$ keV, to account for the presence of many such bands having differing moments of inertia. The simulation also takes into account $M1$ and $E2$ branching, for states having $I > K + 1$, using equations 2.5, 2.6, 2.7 and 2.8:

$$E_{rot}^K(I) = \frac{\hbar^2}{2\mathcal{J}}\left[I(I+1) - K^2\right],$$

(2.4)

$$B(M1; I \to I - 1) = \frac{3}{4\pi}[g_K - g_R]^2 \mu_N^2 K^2 |\langle IK10|I - 1K\rangle|^2 \left[\mu_N^2\right], \qquad (2.5)$$

$$B(E2; I \to I - 2) = \frac{5}{16\pi}e^2 Q_0^2 |\langle IK20|I - 2K\rangle|^2 \left[e^2\mathbf{fm^4}\right], \qquad (2.6)$$

$$\lambda = \frac{B(M1)}{5.687 \times 10^{-14}E_\gamma^{-3}}, \qquad (2.7)$$

$$\lambda = \frac{B(E2)}{8.161 \times 10^{-10}E_\gamma^{-5}}, \qquad (2.8)$$

where E_γ is in MeV and $\lambda(= \frac{1}{\tau})$ is in s^{-1}.

Using the simulation it is possible to model the background produced in the electron spectra for different bandhead conditions such as different values of g_K given by different quasiparticle states, see table 2.3, and for extreme examples such as when $(g_K - g_R) = 0$.

2.7   Internal Conversion

Internal conversion is the process whereby an excited nucleus ejects an atomic electron rather than a photon. The multipole field of a decay from a nuclear state couples with an atomic shell electron wave function, and the energy of the transition is transferred to the electron which is ejected from the atomic shell with a resultant energy given by:

$$E_i = E_\gamma - B_i, \qquad (2.9)$$

where B_i is the binding energy of the electron in shell i .

As a consequence of equation 2.9, an internal conversion spectrum consists of discrete electron energy lines separated by the binding energy differences of the atomic shells. The electron energy lines are labelled with respect to their corresponding
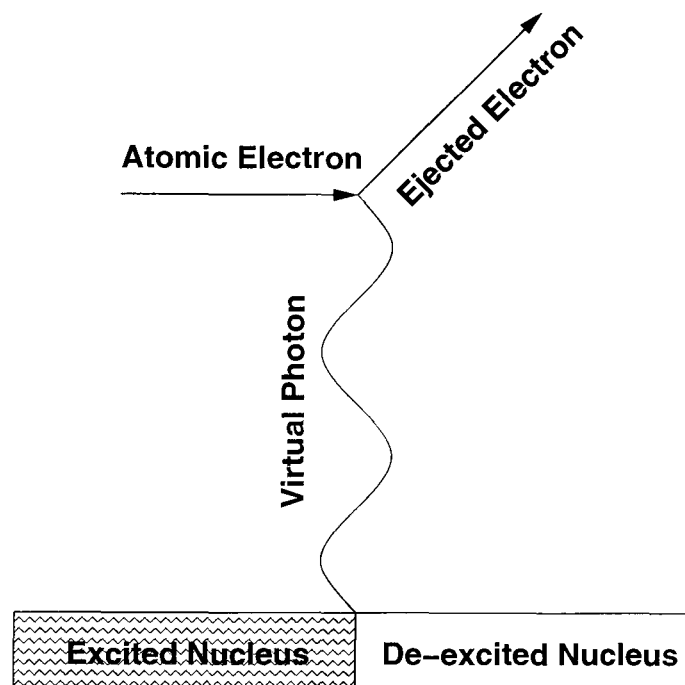
Figure 2.6: Illustration of the internal conversion process, whereby an excited nucleus can decay by emitting a virtual photon which is absorbed by an atomic electron resulting in the ejection of a conversion electron.

atomic shell and orbit. As an example the conversion electrons L_I, L_{II} and L_{III} originate from the $2s_{\frac{1}{2}}$, $2p_{\frac{1}{2}}$ and $2p_{\frac{3}{2}}$ atomic orbitals respectively.

Although the name internal conversion was coined when the process was thought to occur through the photo-electric effect, in which a γ-ray emitted from the nucleus knocks out an electron from an atomic orbital, it should not be regarded as a two step process. More precisely, the nucleus is in an excited state Ψ_i and an electron in an initial bound state ψ_i. The nucleus and electron then exchange a virtual photon, leaving the nucleus in the final state Ψ_f, and the electron in a continuum state ψ_f, as illustrated in figure 2.6. The vacancy left by the emission of a conversion electron is filled very rapidly by an electron from a higher shell, emitting an X-ray in the process. This X-ray emission can prove useful in identifying the Z of reaction products in γ-ray spectra.

2.7.1 Internal Conversion coefficients

If λ_t is the total transition probability between two nuclear states then:

$$\lambda_t = \lambda_\gamma + \lambda_e, \qquad (2.10)$$

where λ_γ is the γ radiation transition probability and λ_e is the internal conversion probability.

The internal conversion coefficient, α, is given by:

$$\alpha = \frac{\lambda_e}{\lambda_\gamma}. \qquad (2.11)$$

Using equation 2.11, equation 2.10 becomes:

$$\lambda_t = \lambda_\gamma(1 + \alpha).$$

It is also useful to define partial conversion coefficients for the different atomic orbits. The total transition probability is then written:

$$\lambda_t = \lambda_\gamma(1 + \alpha_{\mathrm{K}} + \alpha_{\mathrm{L}_I} + \alpha_{\mathrm{L}_{II}} + \alpha_{\mathrm{L}_{III}} + \alpha_{\mathrm{M}_I} + \ldots).$$

The calculation of internal conversion coefficients is a complex process and beyond the scope of this text. A full explanation of the calculation of conversion coefficients is given by Rose [Ro 58] [Ro 66].

The theoretical transition rate of an electromagnetic transition is identical for both γ-ray emission and internal conversion. This is due to both transition rates being governed by the same multipole operator and having the same nuclear matrix parts. Therefore the internal conversion coefficient is independent of the details of the nuclear structure. The coefficient will depend on the atomic number of the atom, the energy of the transition and its multipolarity. The results of non-relativistic calculations using a point nucleus [Kra 88] to evaluate internal conversion coefficients are shown below:

$$\alpha(\mathrm{E}L) \cong \frac{Z^3}{n^3}\left(\frac{L}{L+1}\right)\left(\frac{e^2}{4\pi\epsilon_0\hbar c}\right)^4\left(\frac{2m_ec^2}{\Delta E}\right)^{L+\frac{5}{2}},$$

$$\alpha(\mathrm{M}L) \cong \frac{Z^3}{n^3} \left(\frac{e^2}{4\pi\epsilon_0\hbar c}\right)^4 \left(\frac{2m_e c^2}{\Delta E}\right)^{L+\frac{3}{2}},$$

where n is the principal quantum number for the electron shell, δE, the transition energy and L the multipolarity.

Both expressions illustrate a number of features of internal conversion:

- The Z^3 dependence highlights the increasing importance of the conversion process for heavy nuclei. This dependence is due to the increasing amount of time that the $1s$, $2s$ and $2p$ electrons spend in the nucleus as its size increases, thus increasing the probability of a conversion electron being emitted;

- The conversion coefficient decreases with increasing transition energy;

- The coefficient is proportional to n^{-3}, internal conversion is less prevalent for higher shells;

- The conversion coefficient increases rapidly as the multipole order increases.

The difference in α for electric and magnetic transitions is a useful tool in distinguishing between transitions. Simple intensity measurements can be used to give a good idea of the transition and its parity.

As stated previously, the equations above are based on non-relativistic, point nucleus calculations. With the introduction of nuclear size, the partial conversion coefficients change. The effect on the inner atomic shells K and L_I is great, but this significance decreases with increasing atomic size and the effects are negligible for the L_{III} and higher shells. Calculations using relativistic effects and an extended nucleus have been performed by Hager and Seltzer [HS 68] and Rösel *et al.* [Rö 78]. Internal conversion coefficients utilised in this work are taken from the latter and can be seen in figures 2.7 and 2.8.

2.7.2 Obtaining Spectroscopic Information Using Internal Conversion Coefficients

As the previous section suggests, the observable measure of the absolute value of α enables the multipolarity and parity of a transition to be determined. This method is not often suitable as it requires both the γ-ray and conversion electron intensity to be measured. For highly converted transitions, like those investigated in this report, the measurement of the γ-ray intensities is not possible. Instead, another approach can be made using a measure of the conversion electron intensity and the ratio of partial conversion coefficients. The most common ratio used is that of K to L, as the large separation energy of the K conversion line from the other lines means that it is readily distinguished; although uncertainty in this method can arise if two multipolarites have similar K to L ratios. This method can only be applied if the transition energy is greater than the K electron binding energy. If the resolution of the spectrum is good enough to resolve the individual L sub-shells (typically separated by a few keV), then the ratio of these conversion electrons can be used to identify the transition type. In addition to being able to identify the transition type, the Z of a nucleus can also be immediately identified with conversion electron spectroscopy by measuring the energy differences between the K, L and M atomic lines.

2.8 Fusion-Evaporation Reactions

In order to produce the neutron deficient nuclei, ^{254}No and ^{226}U , a suitable production technique is needed. One mechanism for populating neutron deficient nuclei is via heavy-ion fusion-evaporation reactions. These reactions are suitable for the study of the nuclei in this work for three main reasons:

- The nuclei of interest are produced with relatively high cross sections when compared to light-ion induced reactions;

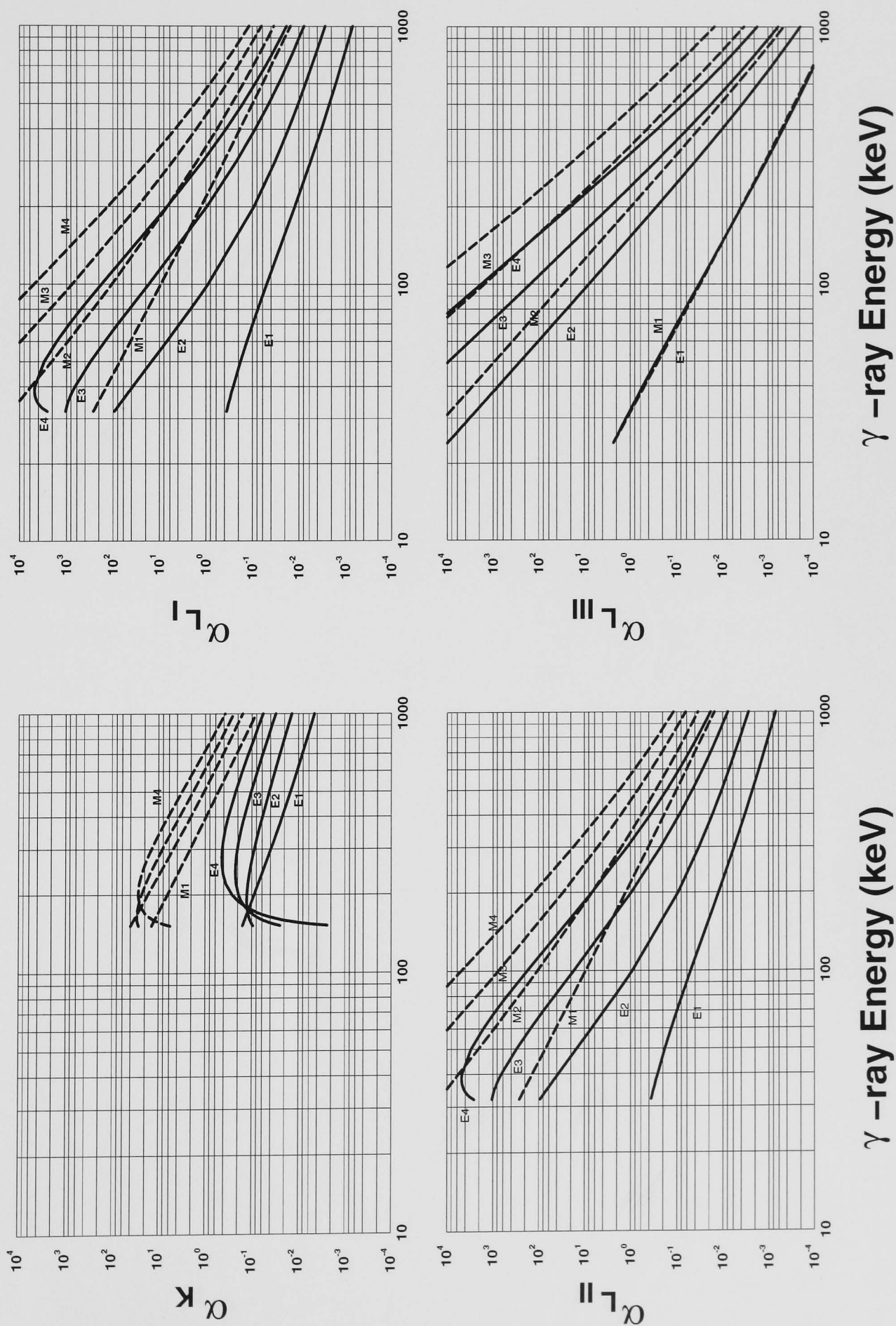- They lead to the production of neutron deficient nuclei;

Figure 2.7: Internal conversion coefficients versus γ-ray energy for $Z = 102$.
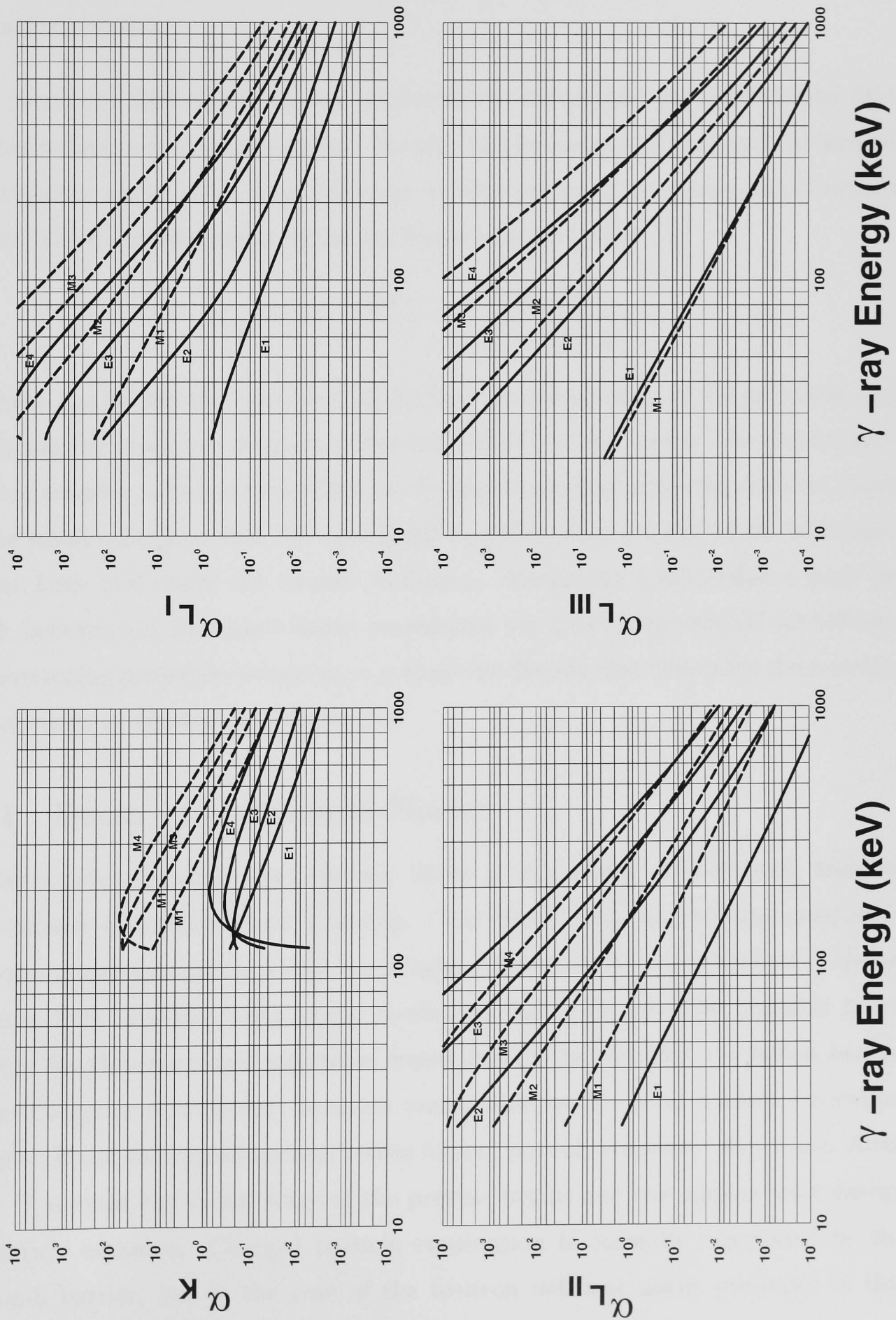
Figure 2.8: Internal conversion coefficients versus γ-ray energy for $Z = 92$.

- High angular momentum is attained by the compound nucleus and its evaporation residues.

In heavy-ion fusion-evaporation reactions, the target and projectile nuclei fuse together to form a compound nucleus. In order for the compound nucleus to be formed the projectile nuclei must have sufficient kinetic energy to overcome the Coulomb barrier. The Coulomb barrier in the lab frame is given by [Ho 78]:

$$V_{lab} = \left(\frac{A_P + A_T}{A_T}\right) \frac{1.44 Z_P Z_T}{1.2(A_P^{\frac{1}{3}} + A_T^{\frac{1}{3}} + 2)},$$

where A_P, Z_P are the mass and atomic number respectively, of the projectile and A_T, Z_T are the mass and atomic number respectively, of the target. The angular momentum transfer, which is dependent on the impact parameter for the reaction, must also be small enough so that the centrifugal repulsion does not exceed the attractive nuclear force and cause the nucleus to fission. Essentially a fine balance must be struck between the increased fission probability but decreasing survival probability with increasing projectile energy, as it is these two factors that determine the reaction cross-section, as illustrated in figure 2.9.

2.8.1 Decay of Compound Nuclei

The formation of a compound nucleus, which is in a highly excited state, leads to the emission of particles and γ quanta. The decay path can be illustrated as a variation of energy against a function of spin relative to the yrast line and is shown in figure 2.10. For the heavy nuclei studied in this work the most probable mode of decay for the compound nucleus is fission due to the fact that the fission barrier (at zero angular momentum) becomes comparable with typical nucleon excitation energies. If the compound nucleus resists fission, particle emission takes place. After $\approx 10^{-19}$ seconds the initial stage of the process begins and the nucleus loses energy by particle emission. Charged particle evaporation is normally suppressed by the Coulomb barrier, but in the case of the neutron deficient nuclei produced in this
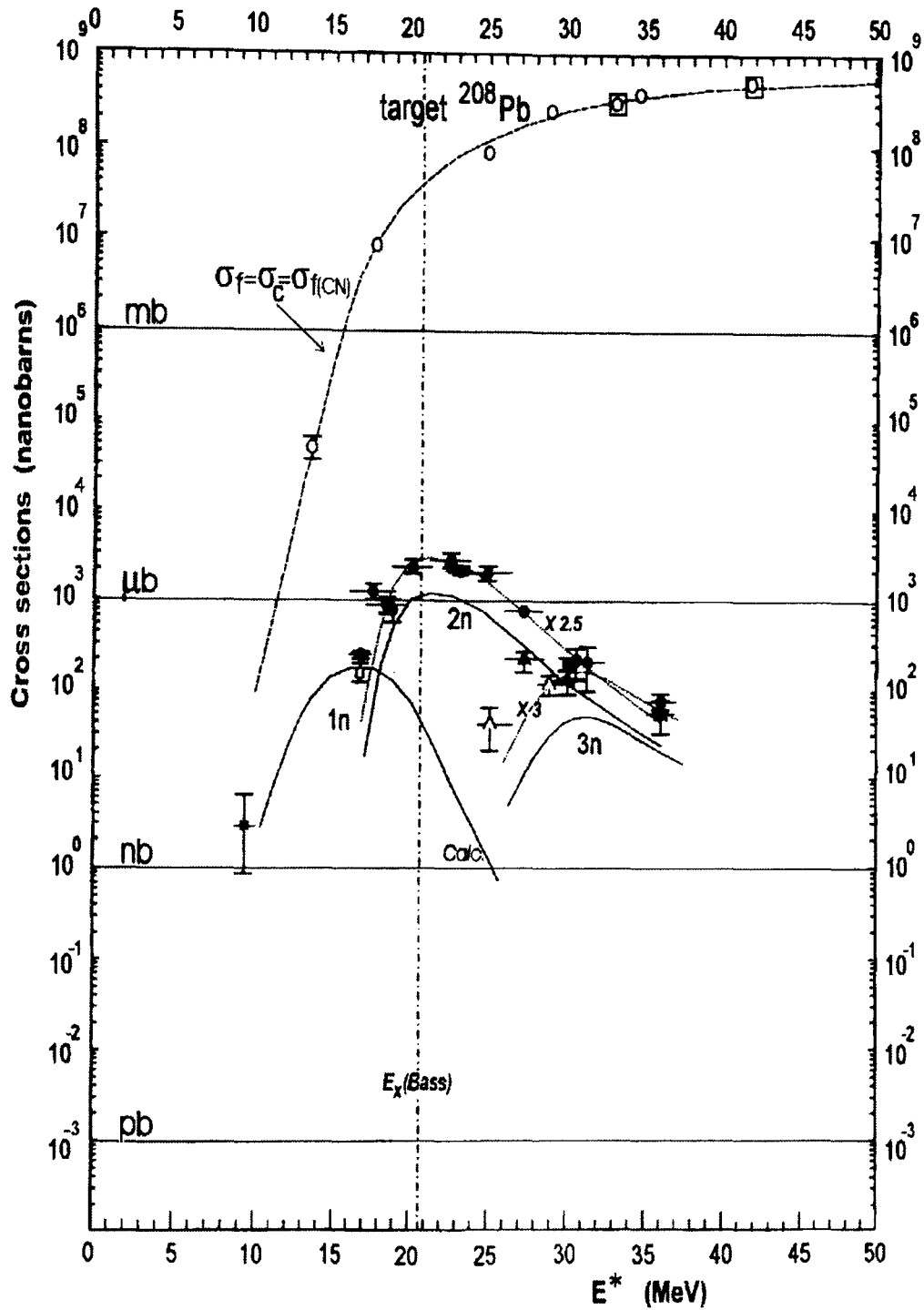
Figure 2.9: Plot of the fission cross-section σ_f and the evaporation cross-section σ_{ev} for the reaction ^{48}Ca + ^{208}Pb, showing the 1, 2 and 3n evaporation channels [It 98]. Curves without points are data taken from work by [Sh 87, Bo 82].

work, α particle and neutron evaporation form a large part of the fusion evaporation cross section. The evaporation particles carry away large amounts of energy ($\approx$ 8-10
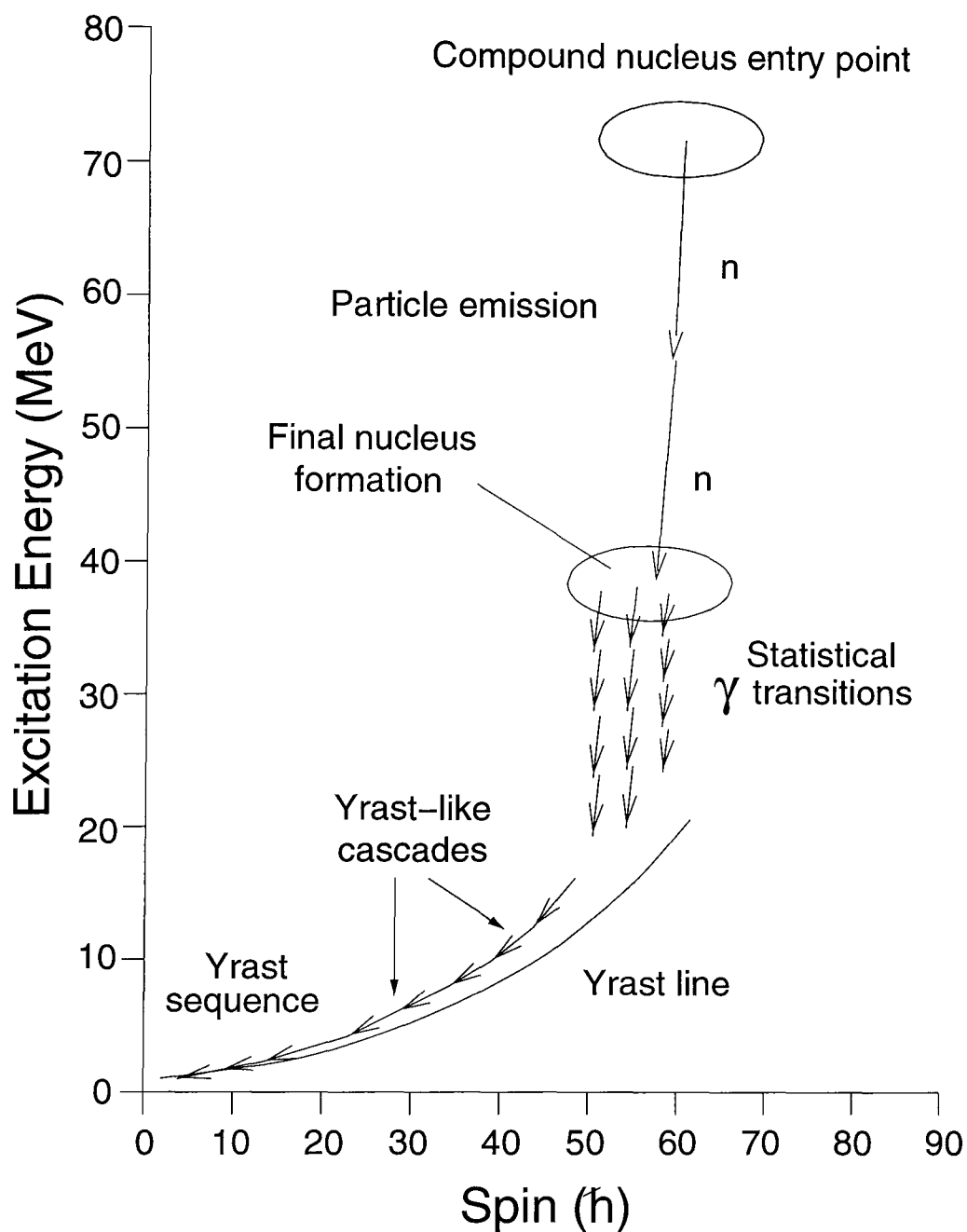
Figure 2.10: Illustration of the decay of the compound nucleus formed in heavy-ion fusion-evaporation reaction.

MeV) but little angular momentum (≈ 1 $\hbar$), hence the initial sharp descent shown in figure 2.10. Particle emission terminates when the nucleus reaches an excitation energy (≈ 8 MeV above the yrast line) where γ decay can compete with particle emission.

After $\approx 10^{-12}$ seconds the nucleus is still relatively excited but particle emission is

no longer permitted. At this point electromagnetic decay takes over and the nucleus decays by the emission of *statistical* or *cooling* γ-rays, which carry away large amounts of energy; but as with the case of particle emission, very little angular momentum.

Eventually, the cooled nucleus approaches the yrast region and the remaining excitation energy and large amounts of angular momentum are dissipated by electromagnetic transitions (or yrast-like transitions) to the ground state.

Chapter 3

The Electron Spectrometer SACRED and Experimental Details

3.1   Introduction

The study of the structure of the heaviest elements is important in order to understand the properties of the mean field when extrapolated far beyond the region of stability [Cw 96, Kru 00]. While the observation of spherical *superheavy* nuclei has proved elusive so far, the study of the structure of deformed nuclei in the middle of this *superheavy* shell can also reveal much about the parameterisation of the mean field. For example the rotational behaviour of ^{254}No [Re 99, Le 99, Re 00] and ^{252}No [He 02a] up to spin 20 $\hbar$ has been studied using γ-ray spectroscopy, in which γ-ray transitions were identified using recoil and α-decay tagging techniques. However, for the heaviest nuclei the sensitivity of γ-ray spectroscopy is reduced by the presence of internal conversion. The probability that an excited nucleus decays via internal conversion increases with increasing Z and with decreasing transition energy. For these reasons the observation of low energy transitions in the heaviest elements is not possible using germanium detector arrays. This precludes the study of odd mass

nuclei and $K \neq 0$ rotational bands in even-even nuclei where the probability of $M1$ decay becomes large compared to other electromagnetic modes. For the ground state rotational bands of well deformed even-even nuclei the transition energies between the lowest states cannot be measured using γ-ray spectroscopy and have been deduced by extrapolation from a Harris fit to the higher spin transitions. It is therefore important to measure the lower energy transitions where possible.

The electron spectrometer SACRED [Gr 03a] was designed to overcome these problems in studying the heaviest nuclei and also to reveal information additional to that obtained from γ-ray spectroscopy. The spectrometer allows the simultaneous direct detection of multiple conversion electrons emitted at the target, with high efficiency. The spectrometer is coupled to the gas-filled recoil separator RITU [Le 95] to allow the heavy recoils and their subsequent α decay to be detected, so that low cross section reactions can be studied effectively. The SACRED spectrometer in conjunction with RITU was used to measure the low-lying transitions of the ground state bands in ^{226}U and ^{254}No.

The previous SACRED spectrometer worked on the *recoil shadow* principle, whereby the 25 segment Si-PIN detector is placed perpendicular to the recoil motion and the emitted conversion electrons were transported by a ≈ 0.6 T super-conducting magnet. Details of the design and operation of the previous SACRED setup can be found in [Jo 95, Bu 96, Ca 98]. The main design goal of the new SACRED spectrometer was to minimise the large Doppler broadening associated with the previous design. In September 1999 construction was started on the new SACRED spectrometer. The new spectrometer was designed to operate in a collinear geometry; the recoils pass just a few centimetres from the detector so that the recoil beam is almost 180° to the detector and Doppler broadening is kept to a minimum. The following sections will describe the principles behind the setup and operation of the SACRED detector.

3.2 SACRED Overview

The electron spectrometer SACRED was designed to be used in conjunction with the recoil separator RITU, so that low cross-section reactions can be studied effectively. This was achieved by positioning the axis of the solenoidal field of the electron spectrometer approximately collinear to the beam axis, so that the conversion electrons of the recoiling nuclei could be detected by the electron spectrometer SACRED, and the recoils then subsequently tagged using the recoil separator RITU. A schematic illustrating the principal features of the conversion electron spectrometer is shown in figure 3.1 and a photograph of SACRED connected to RITU is shown in figure 3.2. The SACRED spectrometer consists of a Si PIN wafer, manufactured by Hamamatsu Photonics (Japan), 500 microns thick, divided into 25 elements, each connected to an individual DC coupled preamplifier. The detector is fully depleted at 100 V, applied via a 500 MΩ load resistor. The elements are arranged in a circular geometry, with outer diameter 27.6 mm, consisting of six quadranted annuli surrounding a central element. The detector and first stage amplification for the Eurisys 761R preamplifiers are mounted on a PCB, while the second stage of the Eurisys 761R preamplifiers are mounted externally to the detector vacuum housing. Electrons are transported from the target to the detector by four, water cooled, conventional conducting magnetic coils. The solenoid axis is positioned at an angle of 177.5° with respect to the beam axis, the beam passing through a hole 12 mm in diameter at a distance 25 mm from the detector, creating an approximately collinear geometry. A true collinear geometry would require an annulus at the centre of the detector, significantly reducing the detection efficiency for low energy electrons. This approximate collinear geometry offers the advantages of reducing both delta electron flux at the detector and Doppler line shape broadening. Although the geometry plays a part in the reduction of delta electrons, the majority of the flux is suppressed by an electrostatic barrier, displaced from the solenoid axis and situated between the target and detector. The displacement of the electrostatic barrier is necessary to avoid the beam hitting the barrier. In order to improve resolution the detector is cooled to a temperature of approximately -20°C
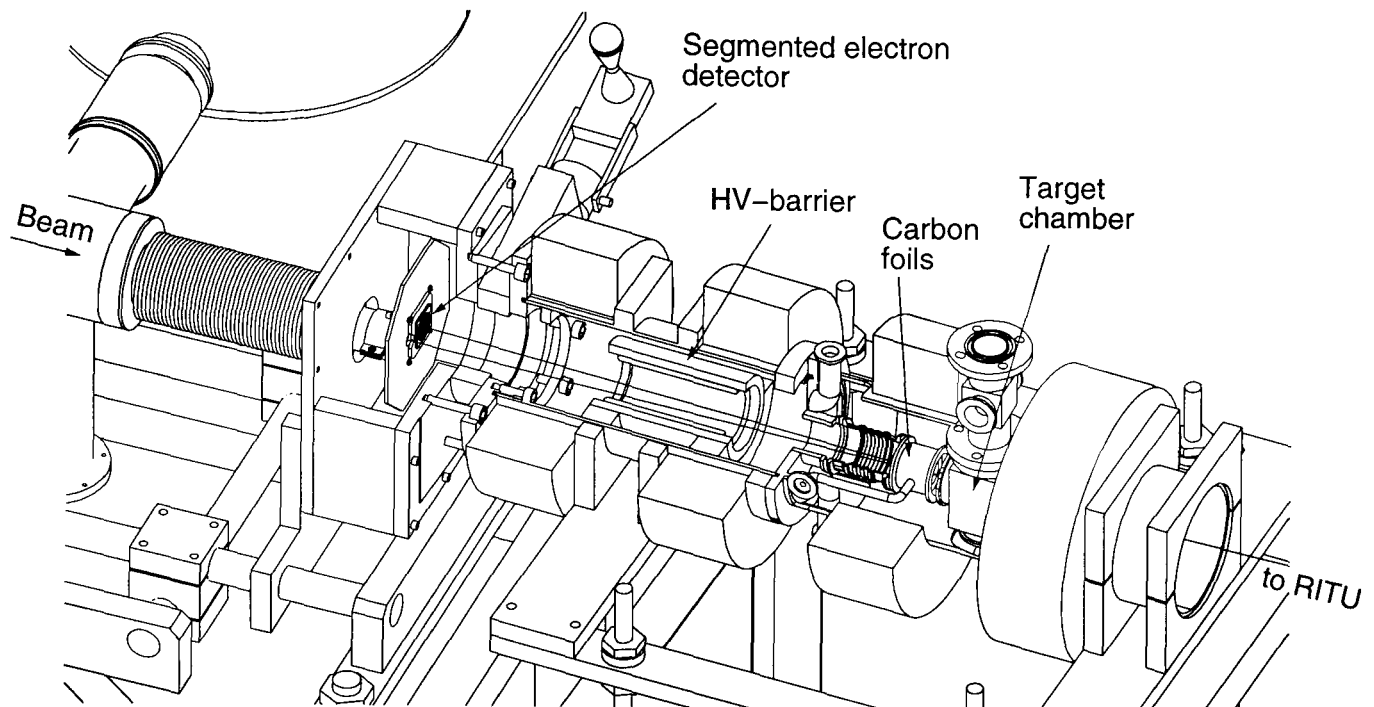
Figure 3.1: Illustration of the conversion electron spectrometer SACRED [Ka 01].

by radiation to a black copper plate in thermal contact with a liquid nitrogen bath.

3.2.1 Conventional Solenoid

The magnetic transport system of SACRED is made up of four normal conducting solenoidal coils. The coils are constructed from loops of 8.7 mm × 8.7 mm hollow copper tube through which the coolant water passes. Each coil is 87 mm in length and has an inner diameter of 134 mm and are spaced at regular intervals of 84 mm using plastic stays. The coils are connected in series and at maximum load of 560 A, produce a magnetic flux density through the spectrometer of $\approx$ 0.3 T. Although the magnetic flux density is nearly an order of magnitude less than the superconducting magnet of the previous SACRED incarnation, it is still sufficient to transport electrons with energies < 150 keV to the detector through the barrier 41 mm in diameter. The calculated magnetic field profile of the coils under normal operation is shown in figure 3.3.
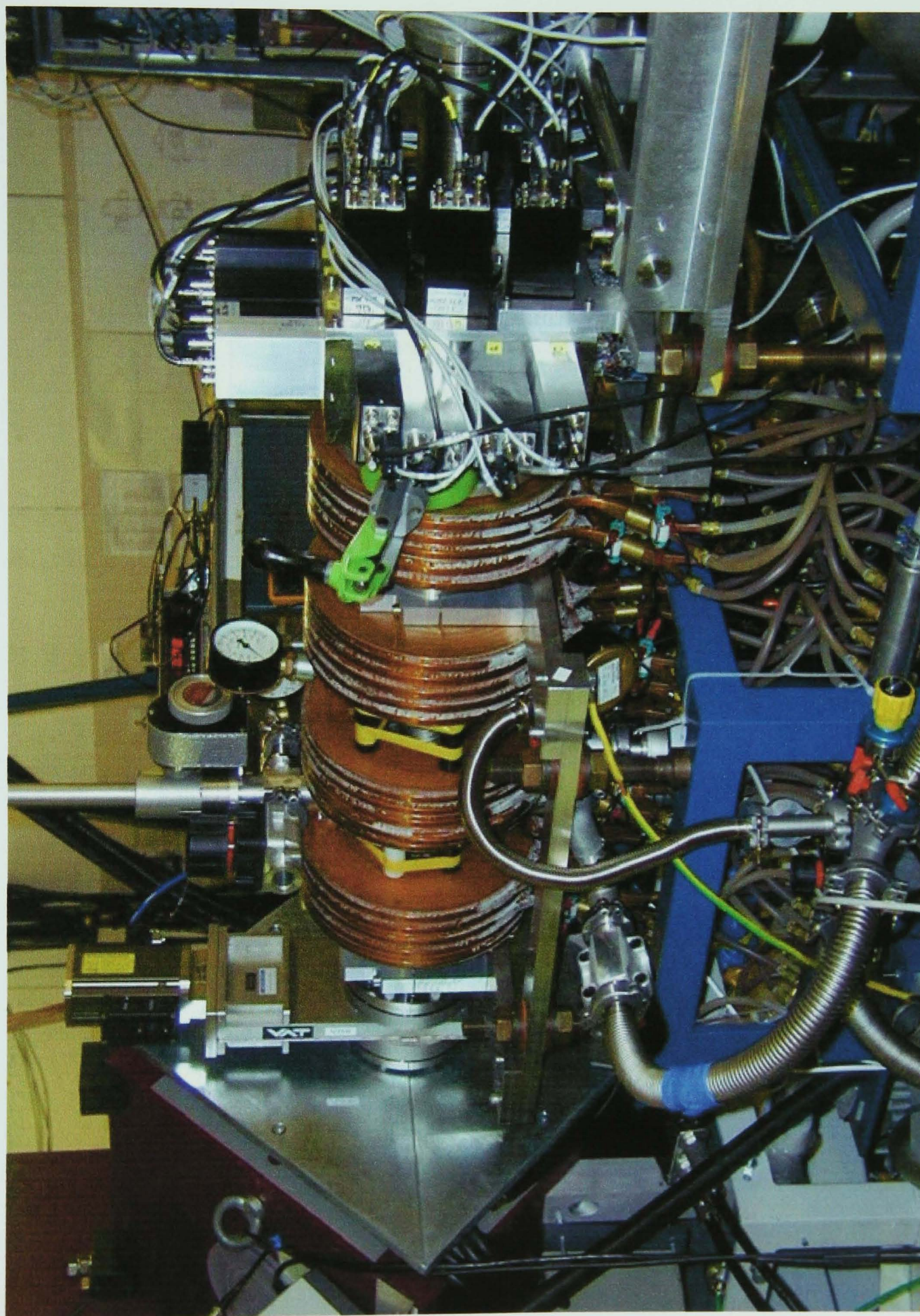
Figure 3.2: Photograph of the SACRED spectrometer connected to the recoil separator RITU.
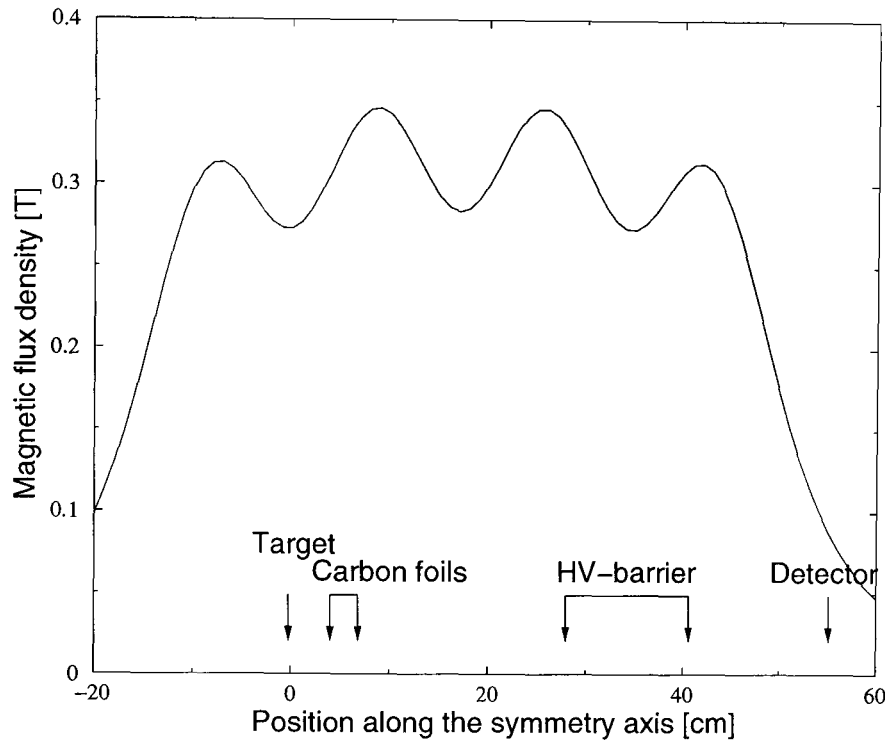
Figure 3.3: Calculated magnetic field profile at the solenoid axis for current I = 560 A [Ka 01].

3.3 High-Voltage Barrier

The background flux of δ electrons due to atomic collisions between the target nuclei and projectile nuclei has to be suppressed if conversion electrons are to be identified. The maximum energy of these δ-electrons can be estimated using equation [KR 69]:

$$E_\delta = 4 \left(\frac{m_e}{m_b} E_k E_b \right)^{\frac{1}{2}} + 4 \frac{m_e}{m_b} E_b,$$

where:

- m_e is the mass of an electron;

- m_b is the mass of the bombarding particle;

- E_k is the binding energy for the electrons in the K-shell;

- E_b is the energy of the bombarding particle.

Therefore the maximum energy for delta electrons, produced in the reaction ^{208}Pb(^{48}Ca,2n)^{254}No at a beam energy of 219 MeV and ^{208}Pb(^{22}Ne,4n)^{226}U at a beam energy of 112 MeV, are 69 keV and 74 keV respectively. With δ-electron production cross-sections many times higher than the typical compound nuclear cross-sections a form of δ-electron background suppression is required.

There are many techniques available to reduce the flux of δ-electrons. The simplest method to reduce the background flux is to place a thin baffle on the solenoid axis between the target and detector [LL 75], while this can prove effective in reducing the transmission of low energy delta electrons, the overall energy resolution would deteriorate due to energy straggling of the electrons travelling through the baffle. A more effective solution is a high voltage barrier placed between the target and detector. In the case of SACRED the negative potential barrier has the advantage that ionisation of residual gas by accelerated electrons, enhanced by the containment effect of the magnetic field, takes place in regions of low electric field density. As a result of this a voltage of up to -50 kV could be applied in a magnetic flux of 0.3 T, whereas only a tenth of this could be applied if the polarity were reversed. Another solution is to apply a retarding potential to the target, but, achieving a high enough potential would prove difficult, as just discussed. The added advantages of having the high voltage barrier placed in the region between the target and detector is that it has no effect on the detected energy of the electrons. Electrons having energies close to the barrier potential will only be transmitted through the barrier for incident trajectories lying close to the solenoid axis, ensuring they lose minimal energy in the target and have minimal backscattering from the detector. A schematic of the high voltage barrier used in SACRED is shown in figure 3.4. The barrier consists of a long stainless steel cylinder surrounded by a sheath of Noryl, which in turn is surrounded by a stainless steel cylinder. The outer bore of the barrier is grounded through being secured to the inner bore of the solenoid magnet and the high voltage feed-through cable is secured to the inner bore of the high voltage barrier by an aluminium ring; the ring and cable are designed to minimise their *shadow* to electrons passing through
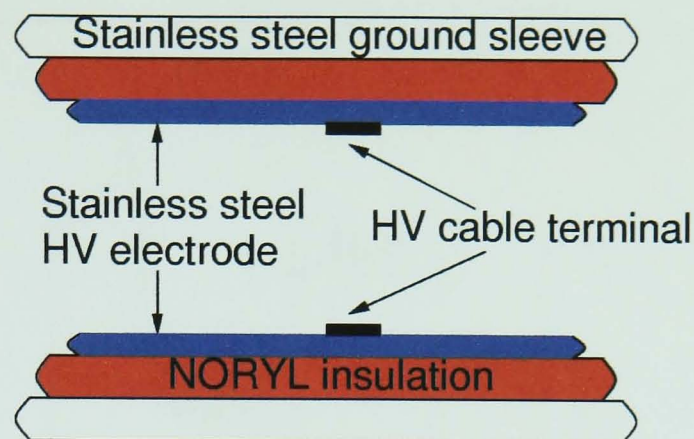
Figure 3.4: Illustration showing a cross-section of the SACRED high voltage barrier.

the barrier. All the components of the barrier were manufactured in such a way as to reduce the density of terminating field lines, thus reducing the likelihood of an electrical breakdown. Due to the near collinear geometry of SACRED the H.V. barrier is displaced from the solenoid axis so that it is not struck by the beam.

In order to minimise the ionisation of residual gas in the region of the high voltage barrier, a good vacuum must be maintained ($< 10^{-6}$ mbar). The gas-filled recoil separator RITU, used in conjunction with SACRED, is maintained at a He pressure of ≈ 1 mbar. With one 60 μg/cm^2 carbon foil window separating the RITU gas volume from SACRED, the lowest pressure achievable is $\approx 10^{-5}$ mbar, which is unacceptable as it causes a high electron background as shown in figure 3.5. An acceptable vacuum, of the order of 10^{-7} mbar, was achieved by using two carbon foils and pumping on the intermediate volume (see figure 3.6). Figure 3.7 shows the SACRED vacuum control system which is required to pump the intermediate volume down to $\approx 10^{-4}$ mbar, at a rate of 0.1 mbar/s. The precise control of the evacuation was required so that no damage was caused to the fragile foils.
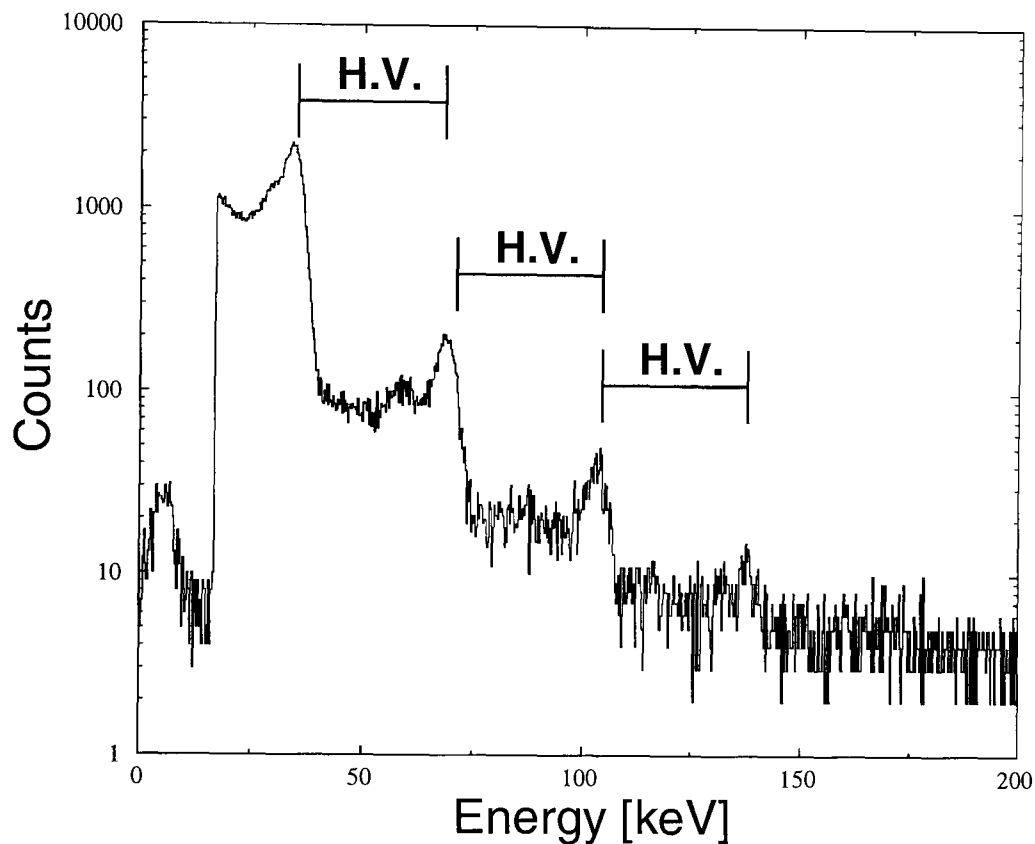
Figure 3.5: Background spectrum induced by the beam when the H.V. barrier is poorly evacuated. The labelled peaks are at intervals equivalent to the H.V. barrier potential (35 keV).

3.4   Si Electron Detector Array

3.4.1   Junction Detector

The resistivity of an intrinsic semiconductor, such as silicon, can be as low as 2×10^5 Ωcm. For the purpose of detection this is too low, as the current would be too great with the application of an electric field. The resistivity can be increased by doping the silicon, but the low ionisation energy of the donors ensures they are ionised by low electric fields. To overcome this problem the silicon can be doped in such a way as to create a p-n junction detector (see figure 3.8). A small depletion region is created at the junction without the application of an external electric field. This depletion region, an area of zero net charge, is the result of minority carriers diffusing across the junction. By the application of a reverse bias, the region can be extended
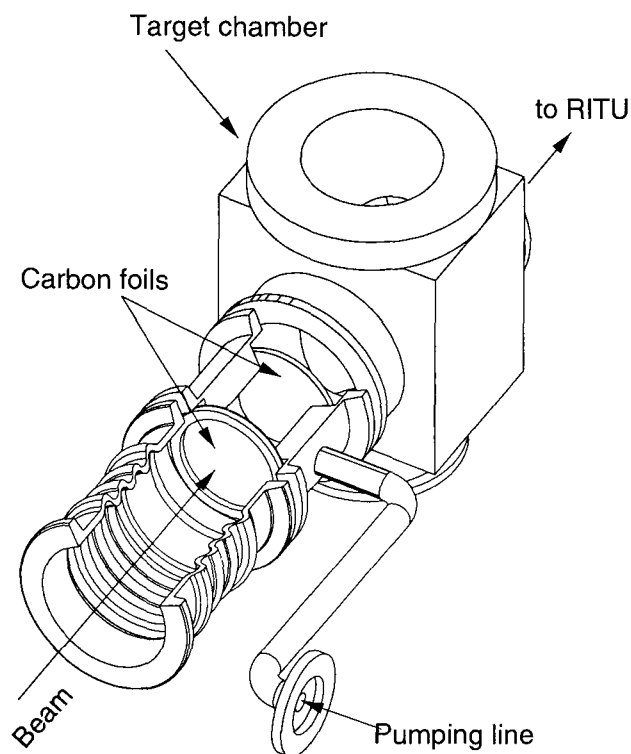
Figure 3.6: Diagram of the apparatus used to hold the carbon foils and allow differential pumping between the RITU gas volume and the SACRED vacuum [Ka 01].

into the p and n type regions, the extent of which is governed by the magnitude of the bias applied. An increased depletion region is desirable for a number of reasons. The depleted region is responsible for the collection of charge carriers following the interaction with an electron, therefore it is desirable to increase the detection volume of the detector by increasing its depletion region. The increased depletion region also decreases detector capacitance, which reduces electronic noise associated with the detector.

3.4.2 PIN Junction detector

PIN junction detectors derive their name from the fact that they consist of an intrinsic region, sandwiched between two heavily and oppositely doped semiconductors. Originally, large intrinsic regions were produced via the lithium drift process [Pe 60, Gi67, La 69]; but, with the advent of modern silicon technology, driven by the computer industry, it is possible to manufacture silicon of a high enough purity
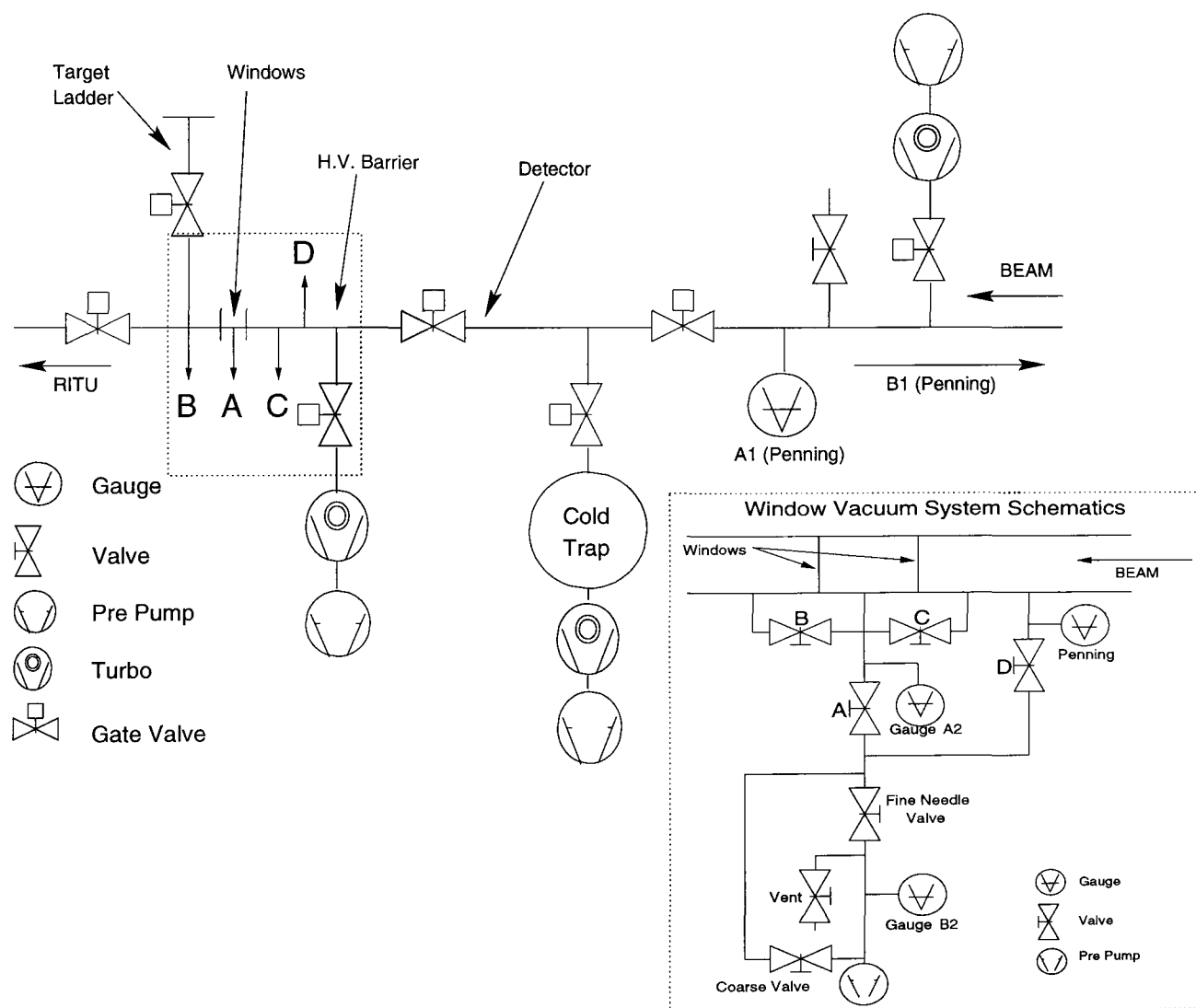
Figure 3.7: Schematic of the SACRED vacuum control system. Valves A, B, C and the needle valve are used to ensure the correct differential vacuum is maintained between the carbon foils.

to remove the need for the lithium drift process.

Modern PIN diodes such as SACRED are manufactured from a base wafer of very low impurity, high resistivity silicon, to form a base of intrinsic silicon. Heavily doped acceptor and donor regions are then formed on the silicon, commonly referred to as the p and n type layers. The p^+ layer acts as a rectifying contact from which the depletion region extends and the n^+ layer acts as a blocking contact to which the depletion region extends to. To operate the detector a reverse bias is applied across the contacts. Due to the greater resistivity of the intrinsic region, virtually all the applied voltage appears across the intrinsic region. Even the most advanced techniques for producing high purity silicon leave impurities, as a result of this the intrinsic region will either be n-type (p-ν-n) or p-type (p-π-n), the former being more commonly available. The depletion layer thickness d is given by:

$$d = \left(\frac{2\epsilon V}{eN}\right)^{\frac{1}{2}},$$

where ϵ is the dielectric constant, V is the bias voltage, e the elementary charge and N is the dopant concentration of the intrinsic material.

The capacitance of a PIN diode is a good approximation to a parallel plate capacitor, due to the fixed charge on either side of the depletion layer. The capacitance
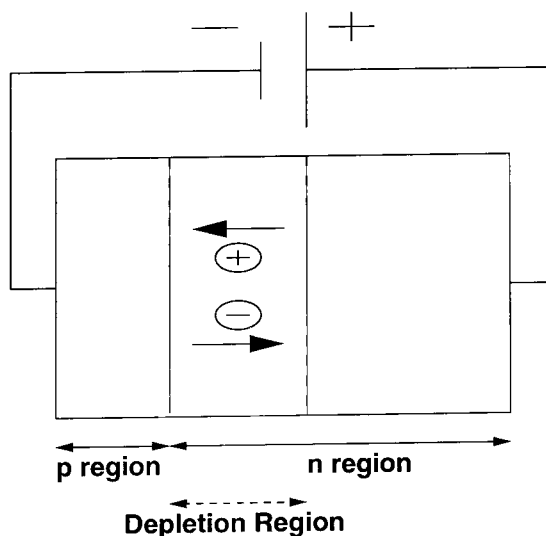
Figure 3.8: Schematic of a p-n junction detector.

is given by the equation:

$$C = \frac{\epsilon}{d} \cong \left(\frac{e\epsilon N}{2V}\right)^{\frac{1}{2}}.$$

From the equation it can be seen that the capacitance C of a PIN diode is controlled by the bias voltage V applied. In order to achieve the best possible resolution it is important that the PIN diode capacitance is minimised, thus it is desirable to operate the PIN diode at a voltage sufficient to cause full depletion.

3.4.3 Leakage Current

When reverse bias voltage is applied to a junction detector, a small current of the order of a μA is normally observed. Junction detector leakage current is related to the bulk volume and surface of the detector. Bulk leakage currents arising internally within the volume of the detector can be caused by either of two mechanisms. The conduction of minority carriers (majority carriers are repelled away from junctions) and by the thermal generation of electron-hole pairs within the depletion region. The first effect is small and is not an important leakage source for the PIN configuration, the second increases with depletion region volume but can be reduced through cooling.

Surface leakage current effects take place at the edges of the junction where relatively large voltage gradients are supported over small distances. The degree of surface leakage can vary greatly, depending on fabrication techniques, and any contamination of the detector surface e.g. dust, fingerprints and vacuum pump oil. These current contributions are shown below [WK 87]:

$$I_{depl} = e\frac{n_i}{\tau_g}A_g W_{depl},$$

$$I_{diff} = e\frac{n_i^2 D_p}{N_d L_p}A_g,$$

$$I_{surf} = e n_i S_0 P_g W_s,$$

where e is the elementary charge, n_i the intrinsic carrier density, τ_g the charge carrier lifetime in the depletion layer, A_g the gate area (p implantation area), W_{depl} the depletion layer thickness, D_p the diffusion coefficient of holes, L_p the diffusion

length of holes, N_d the doping density, S_0 the surface generation velocity, P_g the gate perimeter (perimeter of the p implantation area) and W_s the depletion layer width at the surface.

Leakage current is the largest noise contribution associated with the detector. Random fluctuations in the leakage current that inevitably occur will tend to obscure the small signal current that momentarily flows following an ionising event in the detector. Also the presence of leakage current makes tuning the first stage of the preamplifier a difficult task and in extreme cases leads to preamplifier saturation.

3.4.4 Detector Noise and Resolution

The two main sources of noise from the detector are:

1. Fluctuations in the bulk generated leakage current - *Shot Noise* [Hu 25];

2. Noise generated by series bias resistor - *Johnson Noise* [Jo 28, Ny 28].

The contribution of Shot Noise can only be reduced by cooling the detector. Johnson noise is associated with series resistance and is only present due to the series bias resistor, as a full depletion region eliminates series resistance within the detector. Again cooling reduces the effect of Johnson noise. Noise is also generated by surface leakage currents, which depend on the fabrication and condition of the detector.

These noise sources add in quadrature:

$$(\Delta E_{noise})^2 = (\Delta E_{shot})^2 + (\Delta E_{surface})^2 + (\Delta E_{Johnson})^2.$$

The entire detector setup circuit can be thought of as two distinct noise sources, parallel noise and series noise. The parallel noise consists of the detector leakage current fluctuations, thermal noise from the bias supply and thermal noise from the feedback resistor. The series noise is due to fluctuations in the channel current of the input stage Field Effect Transistor (FET).
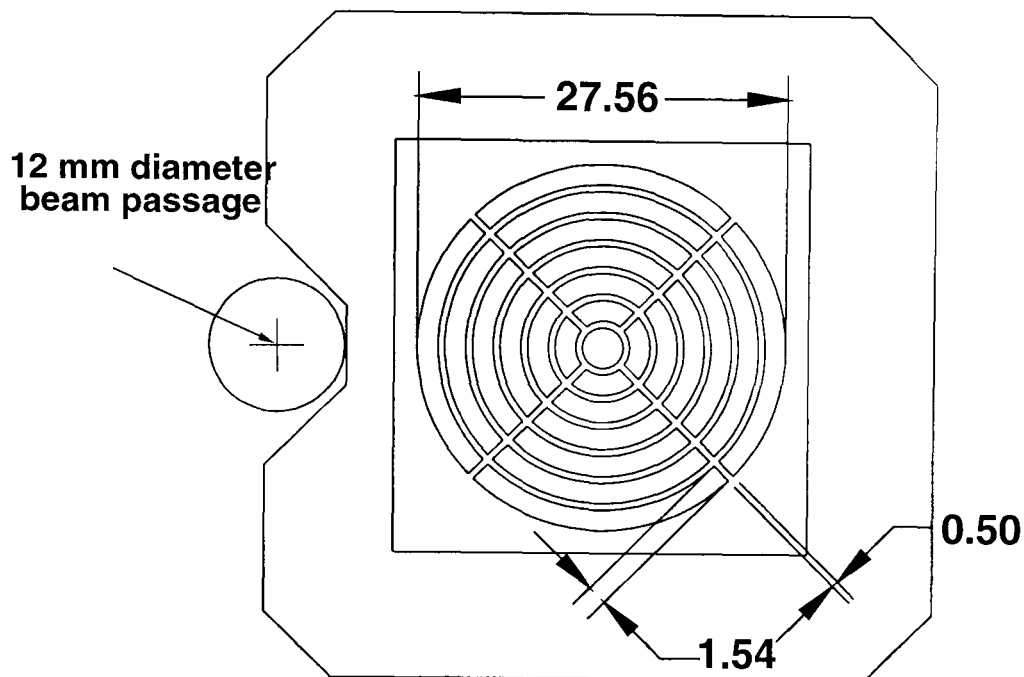
Figure 3.9: Illustration showing the layout of the SACRED segmented Si detector [Ka 01].

3.5 SACRED Silicon Detector Array

The SACRED spectrometer is a 25 element PIN silicon array, 500 microns thick, capable of simultaneously detecting multiple electrons. The detector was constructed by Hamamatsu Photonics of Japan. The array, total diameter 27.56 mm, is made up of 25 individual elements, each 1.54 mm wide, arranged in a circular geometry comprising six quadranted annuli surrounding a central element, for an illustration see figure 3.9. The increasing area of the elements from the inner ring to the outer ring helps equalise the counting rate across the electronics. The channels between the individual elements used to connect detector elements to the outer circuit board pads are 0.2 mm wide. The connections from the individual wafer elements to the gold plated nickel tracks on the circuit board are made using ultrasonically bonded wires which are protected by a resin coating. The connections and detector layout are constructed in such a way as to minimise cross-talk between individual elements during operation. A depletion depth of 500 μm can be obtained when operating at a reverse bias of 100 V, which is applied via a 500 MΩ resistor, to the rear common
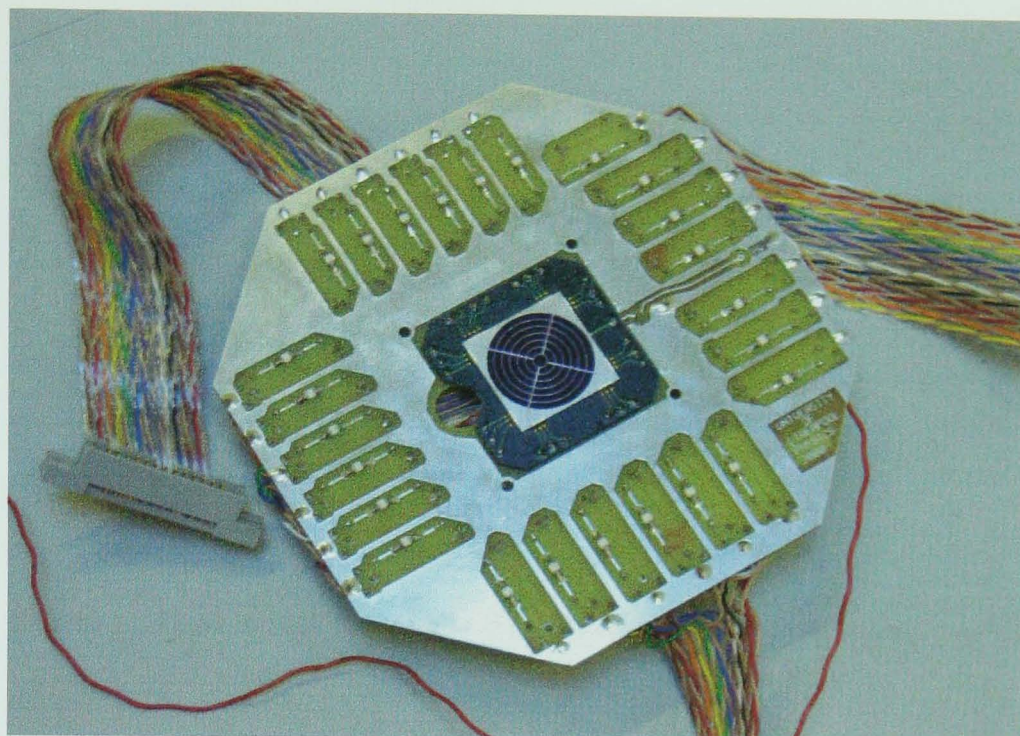
Figure 3.10: Photograph of the SACRED detector mounted on the first stage preamplification board.

cathode of the silicon wafer in contact with the central metallic surface of the support board.

The signals from the individual elements are amplified by Eurisys 761R preamplifiers. The first stage preamplification components are mounted on a printed circuit board with the detector daughter board. The first stage comprises a FET and a 500 MΩ resistor in parallel with a 0.2 pF capacitor. The output of this first stage is connected to the second stage external preamplifier units via ribbon cables and vacuum feed-throughs. The maximum count rate (12 kHz) of the individual Si elements (2μs amplifier shaping time) is restricted by the maximum acceptable dead time in the individual ADCs. It is this maximum count rate which is the deciding factor when determining the minimum barrier voltage (lowering the voltage increases flux of δ-electrons). A photograph of the detector mounted on the first stage preamplification board is shown in figure 3.10.
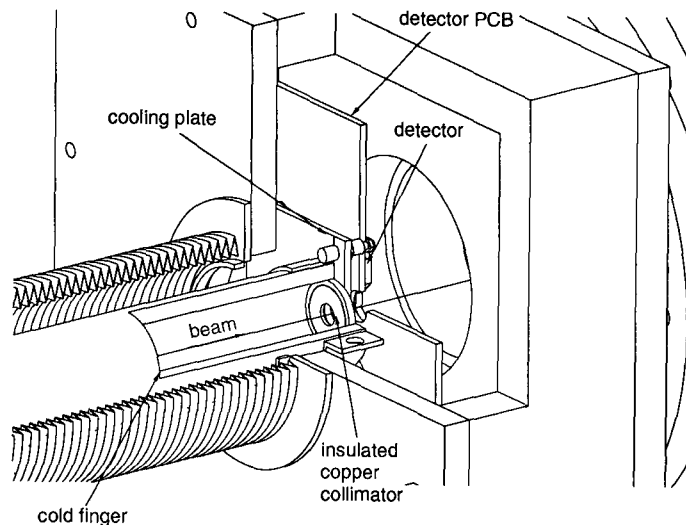
Figure 3.11: Diagram of the SACRED cooling apparatus [Ka 01].

3.5.1 Cooling

In order to reduce leakage current and shot noise and thus improve the performance of the SACRED detector array, it was cooled to a temperature of -20°C (the manufacturers minimum specified operating temperature). The cooling brought about a 10 fold reduction in leakage current; the leakage current dropped from $\approx$30 nA at room temperature to $\approx$3 nA, under an operating voltage of 80 V. The cooling was achieved by thermal radiation from the rear of the detector board which was coated with carbon and held in close proximity to a cooled, carbon coated, copper plate. The copper plate was coupled to a liquid nitrogen dewar via a copper cold finger, see figure 3.11. Carbon coating of the surfaces increases the emissivity of the two surfaces by approximately three fold. The temperature of the detector was monitored by a platinum resistance thermometer[1] placed in close proximity to the detector. An added benefit of the detector cooling system is that it augments the cold trap used as part of the pumping system.

---

[1]Part no. Oxford PRZ 0015

3.5.2 Efficiency

Using a calibrated ^{133}Ba source in the target position, the relative efficiency of SAC-RED can be obtained from peak intensity measurements in the singles data and normalised using previously published data [Tr 90].

A measure of the absolute efficiency requires coincident decays to be measured. The 356 keV transition is in clear coincidence with the 81 keV transition to the ground state, and provides the cleanest gated coincidence spectrum for measurement. The absolute efficiency values were calculated using the equation:

$$\frac{I^C_{e_1-e_2}}{I^S_{e_1}} = \frac{\epsilon_1 \epsilon_2}{\epsilon_1} \cdot \frac{\alpha_K}{(1 + \Sigma\alpha)} \cdot B_I, \qquad (3.1)$$

where:

- $I^C_{e_1-e_2}$ is the intensity of electron line e_2 in coincidence with line e_1;

- $I^S_{e_1}$ is the intensity of electron line e_1 in singles;

- ϵ_1 is the detection efficiency of electrons in line e_1;

- ϵ_2 is the detection efficiency of electrons in line e_2;

- $\frac{\alpha_K}{(1+\Sigma\alpha)}$ Is the fraction of the K conversion coefficient compared to the total conversion coefficient for the e_2 transitions;

- B_I is the branching intensity of the total intensity, taking into account the transitions into and out of the e_1 associated nuclear state.

The internal conversion coefficients needed for the calculations were taken from [Rö 78]. Corrections were made, using [Tr 90], to take into account the measured intensity of the 81 K line, which is contaminated by the 53 L and 79 K transitions.

The data were sorted into symmetric electron-electron matrices, see section 4.6.5, so that a coincidence electron spectrum could be produced for a particular energy gate. Coincidence energy gates were set for both the 81 keV and 365 keV transitions so that the absolute efficiency could be calculated using equation 3.1, and the absolute

efficiency was extended to other ^{133}Ba electron energies by normalising the relative efficiency values.

For in-beam measurements the barrier is usually maintained between -35 and -40 kV. One drawback of the high voltage barrier is the reduction in efficiency experienced as the electron detection energy approaches the barrier voltage. Consequently to make reliable in-beam intensity measurements the efficiency of the detector must be known when the barrier is being operated. Calibration measurements were made with the high voltage barrier in operation, and analysed as discussed above to produce the efficiency curves shown in figure 3.12. Looking at the efficiency curve it is apparent that although the simulation [Bu 92] is generally in good agreement with the data, at the highest energy ($\approx$ 430 keV) the simulation disagrees with the data and no obvious solution was forthcoming when this discrepancy was investigated. Although a solution to this problem might be needed for future work, it is of less importance in this work as the spectra observed are at energies where there is good agreement between the simulation and the data.

3.5.3 Resolution

Improving the resolution of radiation detectors is always desirable and electron spectroscopy is no exception to this general rule. Improved resolution helps resolve the fine detail of the subshell structure of conversion electrons and allows more accurate sorting conditions to be used, thus helping in general spectra analysis. Table 3.1 gives the resolution for the SACRED spectrometer using ^{133}Ba source measurements.

The reduced energy resolution at lower energies is a consequence of energy straggling, which takes place in the source and the detector dead layer. This demonstrates the importance of thin detector entrance windows for charged particle spectroscopy and also highlights the need for thin targets to be used in in-beam electron spectroscopy. The resolution degraded with use as deposits built up on the surface of the detector. This energy degradation is due to two different processes. Firstly the deposits on the detector surface increase energy straggling of the electrons and secondly
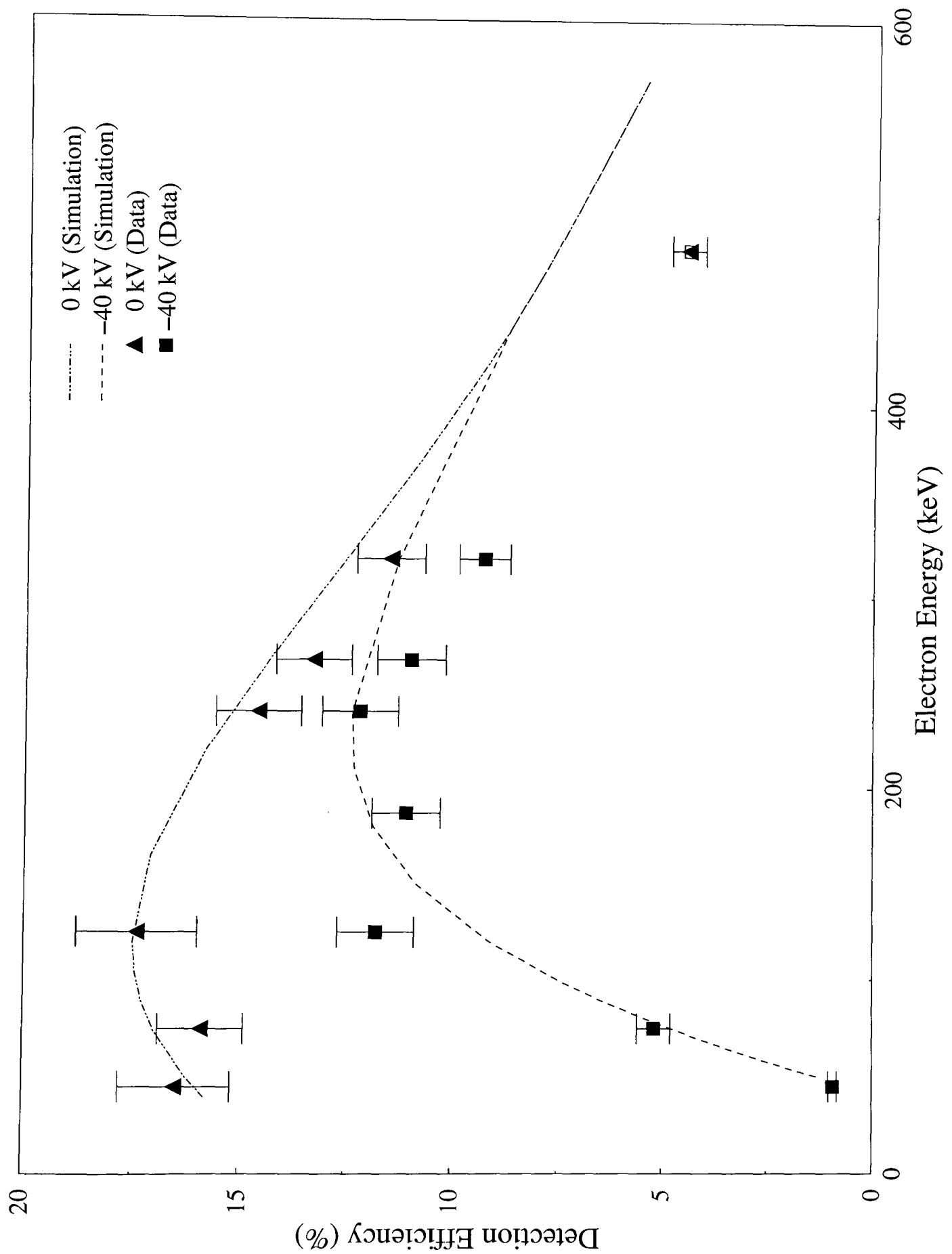
Figure 3.12: Absolute efficiency curve for the SACRED spectrometer taken using a ^{133}Ba electron source [Gr 03b]. The simulated data are from the SOLENOID Monte Carlo code [Bu 92].

Table 3.1: Energy resolution for SACRED spectrometer measured using ^{133}Ba source.

Energy (keV)	Resolution (keV)
45	4.6
75	4.0
124	3.3
240	3.4
267	3.6
320	3.4

the deposits increase the detector surface leakage current; both of which manifest themselves in degraded energy resolution.

3.6 Recoil Separators

Due to the low production cross-sections of the heaviest elements, where fission dominates the total cross-section, special methods are required to isolate transitions originating from the fusion channels.

A recoil separator is needed to collect the nuclei of interest whilst separating them from the primary beam and fission products. Two approaches can be taken in the construction of a recoil separator. The separator can be operated under a vacuum which generally gives a good mass resolution but poor transmission efficiency, due to the fact that the reaction products will have wide ranging charge states. Taking a different approach, using an idea proposed by Cohen and Fulmer [CF 58], the separator can be gas-filled, whereby the heavy ions travelling through the separator will undergo atomic collisions, the net result being that the ions will emerge at the focal plane with a mean charge state, see figure 3.13. This second approach enables a much higher transmission of fusion-evaporation products, which is essentially due the acceptance of all charge states, while still maintaining good beam suppression. It
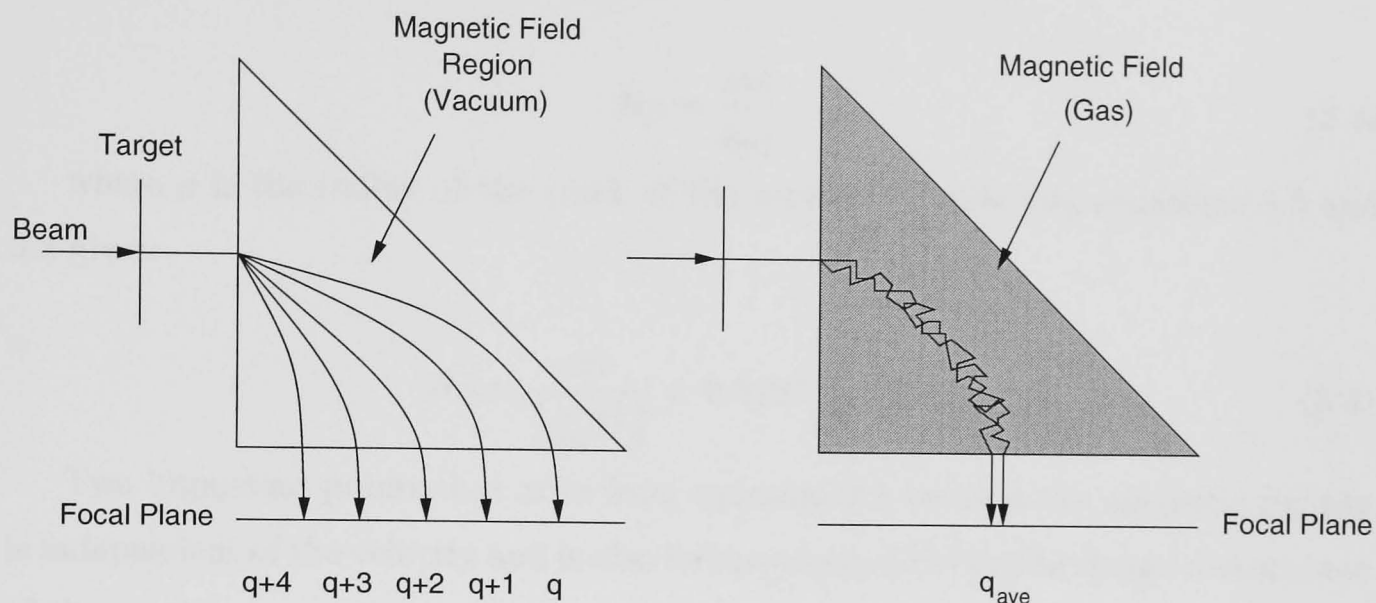
Figure 3.13: Schematic highlighting the differences between evacuated and gas-filled recoil separators.

should be noted that this increased transmission efficiency is gained at the expense of mass resolution (typically 1 part in 300 for a non gas-filled device such as the FMA at the Argonne National Laboratory). The design of gas-filled recoil separators includes a dipole bending magnet behind the target position usually followed by two quadrupole magnets to focus the ion beam onto the focal plane. The dipole magnet is used for in-flight separation of the primary beam and the fusion products. This design is employed by SASSY [Gh 88], JINR [Og 91] and RITU [Le 95]. The average charge state q_{ave} of an ion moving in a dilute gas can be defined using the Thomas-Fermi model. If the velocity v is in the range:

$$1 < \frac{v}{v_0} < Z^{\frac{2}{3}},$$

then:

$$q_{ave} \approx \frac{v}{v_0} Z^{\frac{1}{3}}, \tag{3.2}$$

where v_0 is the Bohr velocity ($v_0 = \frac{c}{\alpha}$) and v is the velocity of the ion.

The magnetic rigidity Bρ of an ion moving in a gas is described [Gh 88] as:

$$B\rho = \frac{mv}{q_{ave}}, \tag{3.3}$$

where ρ is the radius of the track of the particle. Combining equations 3.2 and 3.3 gives:

$$B\rho \approx \frac{mv}{\left(\frac{v}{v_0}Z^{\frac{1}{3}}\right)} = 0.0227\frac{A}{Z^{\frac{1}{3}}} \; [\mathbf{Tm}]. \tag{3.4}$$

Two important points that arise from equation 3.4 are that the magnetic rigidity is independent of the velocity and is also independent of the initial charge distribution of the particles.

3.6.1 RITU Gas-Filled Recoil Separator

The gas-filled recoil separator RITU (Recoil Ion Transport Unit) [Le 95] was constructed by the Physics Department of the University of Jyväskylä. RITU varies from many gas-filled recoil separators in that it has three quadrupole magnets instead of the usual two. The third strongly vertical focusing quadrupole magnet is positioned in front of the dipole magnet. This leads to an increase in the transmission efficiency because the quadrupole magnet leads to better matching of the recoil ion beam to the angular acceptance of the dipole magnet. The dipole magnet separates the evaporation residues from the beam which is dumped into an electrode inside the dipole magnet. The two quadrupole magnets, behind the dipole magnet, focus the fusion evaporation residues both horizontally and vertically . A schematic of RITU along with SACRED positioned in the target position is shown in figure 3.14. Normally the magnetic field region is filled by a constant flow of helium gas, regulated by a mass flow controller, the flow is such that the entire volume is replenished twice each hour, thus keeping impurities to a minimum. The gas pressure is varied between 0.3 and 3 mbar depending on the reaction used, the objective being to minimise the image size at the focal plane. Thin foils (0.04-0.1 mg/cm^2) of carbon or nickel are used to separate the focal plane detector from the gas-filled region. The helium gas
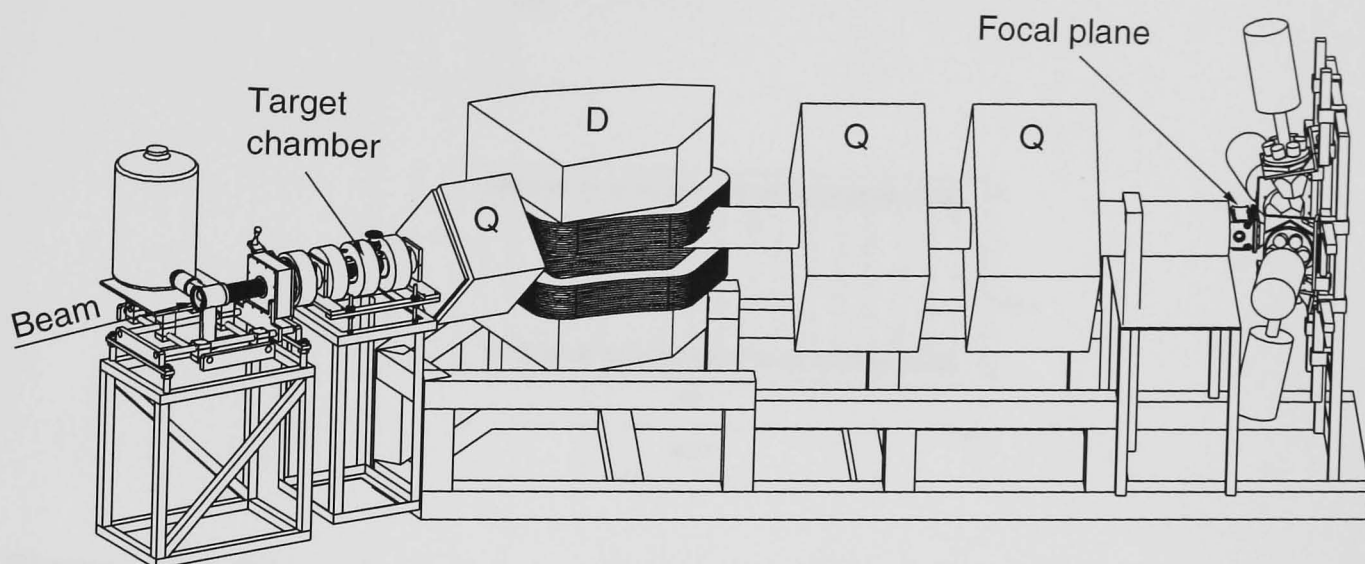
Figure 3.14: Schematic of the gas-filled recoil separator RITU coupled to the electron spectrometer SACRED [Ka 01].

also serves to cool the target, enabling high intensity beams to be used without the need for a target wheel.

3.6.2 Recoil Identification

One of the disadvantages highlighted for gas-filled recoil separators such as RITU is their poor mass resolution, and as such the recoiling nuclei must be identified through other techniques. The two nuclei studied in this work were identified using two different methods. ^{226}U recoils were identified using the position sensitive silicon strip detector and the method of delayed coincidences [Sh 79], while ^{254}No recoils were identified using time of flight (TOF) information gained from two Multi-Wire Proportional Avalanche Counters (MWPAC), see sections 4.4.4 and 4.5 for examples.

The position sensitive silicon strip detector [Uu 96] placed at the focal plane of RITU has dimensions 80mm × 35mm and is 300 μm thick. The detector is divided into sixteen 5 mm wide strips which are position sensitive in the vertical plane. This position sensitivity is a result of charge division within the strip which is made possible by the resistive layer fabricated into the detector. A signal is taken from both ends of
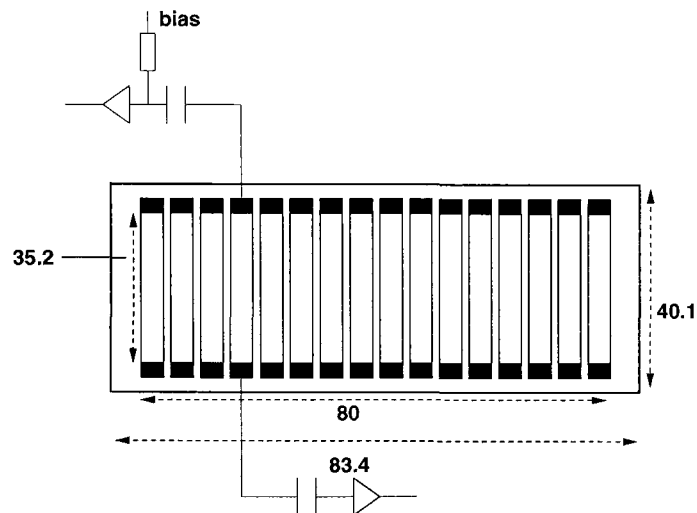
Figure 3.15: Schematic showing the PSSD at the focal plane of RITU, with an example of the electronics for one of the elements.

a strip and summed to give the total energy of the event in the strip (see figure 3.15). In order to obtain the position of an event in the strip, the signal from one end of the strip is divided by the total summed signal. The MWPAC is situated in front of the focal plane detector and consists of two planes of dimensions 145 mm × 108 mm and separated by 200 mm, see figure 3.16. The volume inside the MWPAC detectors is filled with 3 mbar of isobutane, which is chosen for its high electron drift velocity. Recoils are selected from scattered beam and other unwanted reaction products by their different flight times through the gas counter.
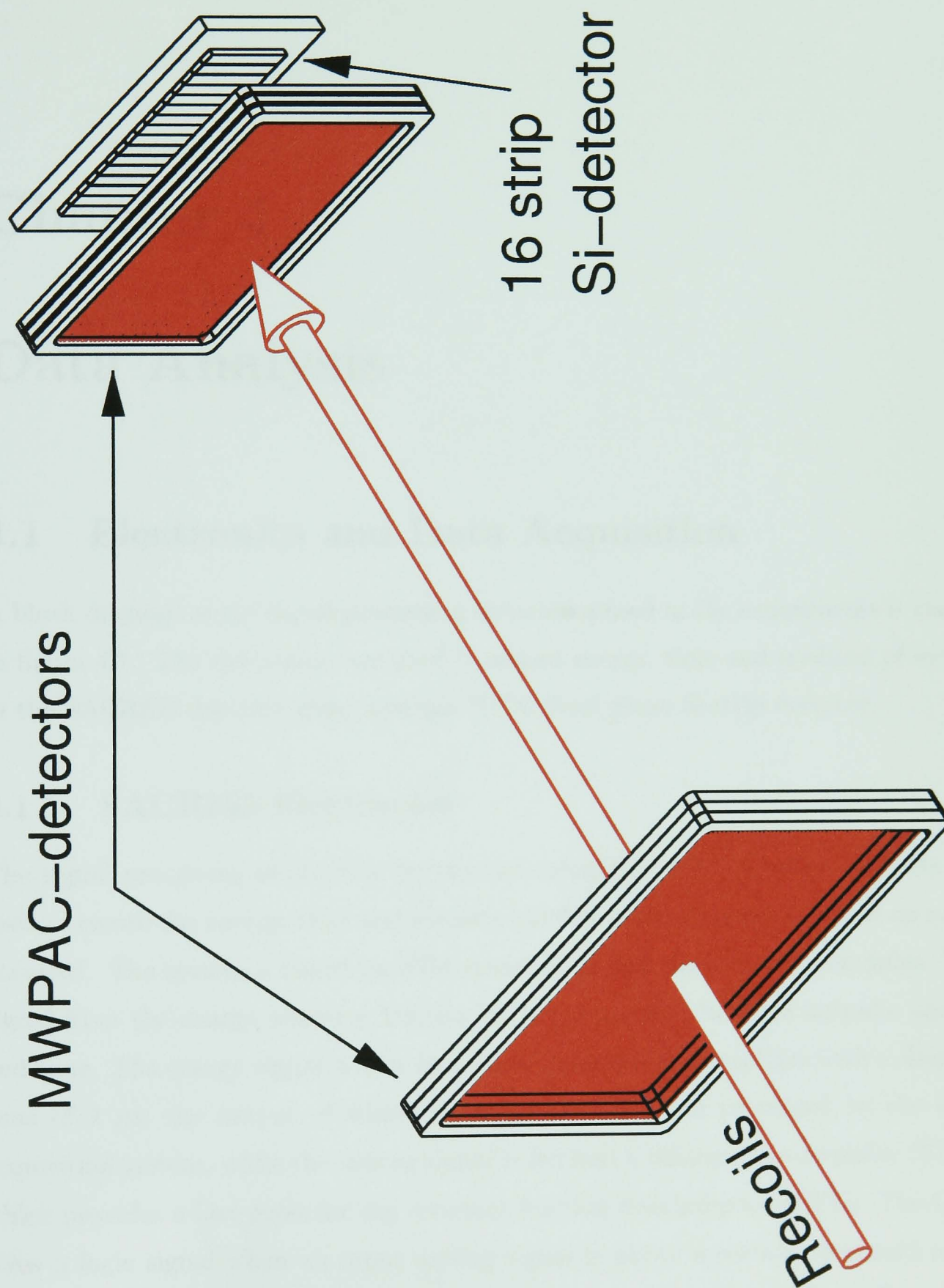
Figure 3.16: Diagram of the Multi Wire Proportional Avalanche Counter used at the focal plane of RITU.

Chapter 4

Data Analysis

4.1 Electronics and Data Acquisition

A block diagram of the signal processing electronics used in the experiments is shown in figure 4.1. The electronics are used to record energy, time and position of events in the SACRED detector array and the RITU focal plane Si-strip detector.

4.1.1 SACRED Electronics

The signal processing electronics for the individual SACRED detector elements are used to record the energy, time and identity number of the detector in which an event occurred. The system is based on NIM standard nuclear spectroscopy modules. The signal from the charge sensitive Eurisys 761R preamplifier has two outputs, energy and time. The energy signal is sent to a linear spectroscopy amplifier with a shaping time of 2 μs, the output of which is fed to an ADC and processed by the data acquisition system, while the timing signal is fed into a timing filter amplifier (TFA), which provides a fast pulse for the constant fraction discriminator (CFD). The CFD gives a logic signal when an input analog signal is above a certain threshold level, which is set by the user, above the constant noise background level. The CFD signal for each element is overlapped, in a coincidence unit, with a 500 ns wide trigger pulse
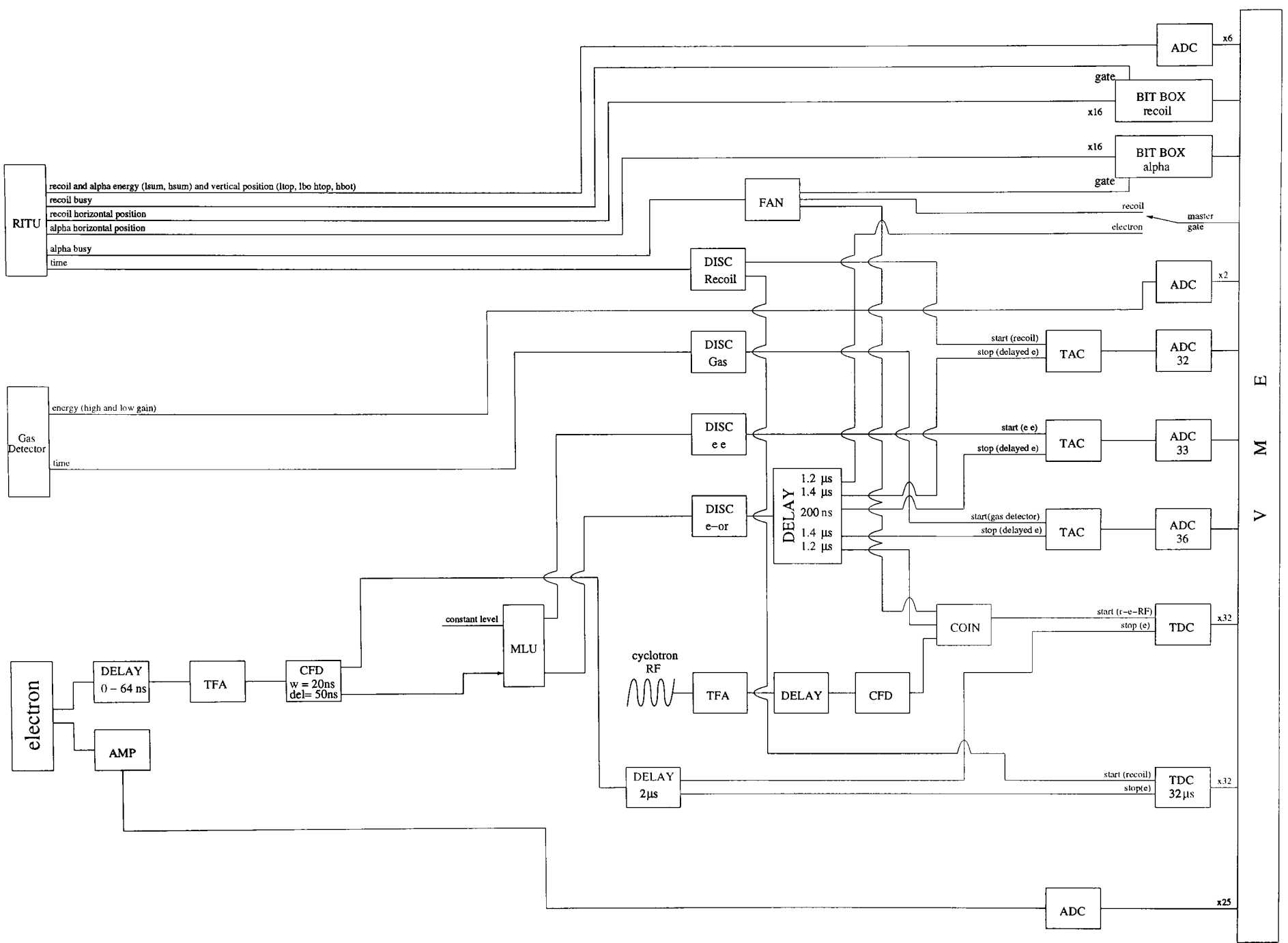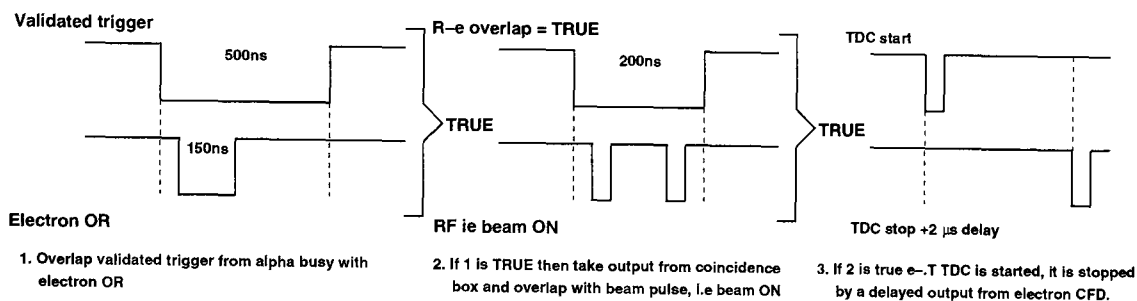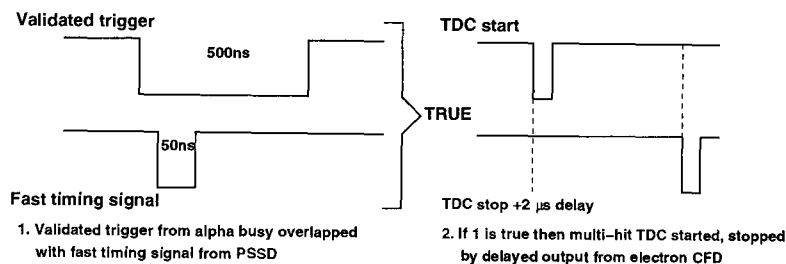
Figure 4.1: Block diagram of the SACRED and RITU electronics.

e−.T TDC

Validated trigger
500ns
150ns
Electron OR

R−e overlap = TRUE
200ns
TRUE
RF ie beam ON

TDC start
TRUE
TDC stop +2 μs delay

1. Overlap validated trigger from alpha busy with electron OR

2. If 1 is TRUE then take output from coincidence box and overlap with beam pulse, I.e beam ON

3. If 2 is true e−.T TDC is started, it is stopped by a delayed output from electron CFD.

Recoil−electron TDC

Validated trigger
500ns
50ns
Fast timing signal

TDC start
TRUE
TDC stop +2 μs delay

1. Validated trigger from alpha busy overlapped with fast timing signal from PSSD

2. If 1 is true then multi−hit TDC started, stopped by delayed output from electron CFD

Figure 4.2: Schematic showing the timing characteristics for the e⁻.T and recoil electron TDC. [Pa 03]

from the alpha busy signal and a 200 ns wide signal from the cyclotron RF. If the three signals overlap and give a true event in the coincidence unit, then the appropriate time-to-digital converter (TDC) is started, which is then stopped by a 2 μs delayed signal from the CFD, see figure 4.2 for details on e⁻ TDC and recoil electron TDC timing. The time between the start and stop signal is then processed from the TDC to the VME. The CFD is also used as a stop signal for various TACs, so that timing information can be acquired on a number of aspects. The VME also has a master gate which dictates the operation of the VME electronics. The master gate is set so that the VME crate is only active when a signal event is present from the focal plane alpha busy signal; therefore, a preliminary selection of events is carried out as events are only collected in the VME when in coincidence with an event in the focal plane.

4.1.2 Data Acquisition

The acquisition system utilised at Jyväskylä is based on a scaled down version of the EUROGAM system [McPh 92]. The processing of events generated by each ADC is carried out by VME interface cards. The VME cards are capable of continuous histograming of singles data, where data are simply read out at the ADC when it receives a signal at the input over a certain threshold. This is only useful for on-line monitoring of the experiment and as such the data is not written to magnetic tape. For the experiments carried out using SACRED, data were only written to tape if events were present in the RITU detector, this is known as the master trigger. The master trigger signal enables the read-out of any coincident ADCs into the VME. If a coincident requirement occurs the VME readout controller stops all singles acquisition, allowing a common dead time for all ADC measurements, the length of which is governed by the last ADC conversion in coincidence with the master gate. This negates the effect of dead time for coincidence data comparison and also reduces the counting rate of the electron ADCs and the quantity of data to be written to tape. Data are then passed on to the event builder, via high speed memory. The event builder is used to convert the data into EUROGAM format [Cr 91], which are then sent over a private Ethernet link to the tape server, where they are recorded on magnetic tape.

4.2 ^{226}U Experimental Details

Two experiments were carried out at the accelerator laboratory of the University of Jyväskylä. In the first experiment a beam of 112 MeV ^{22}Ne, with an average intensity of 8.5 particle nA, irradiated a ^{208}Pb target, of 200 μg/cm^2 thickness, for approximately 29 hours, with a helium gas pressure of 0.3 mbar in the magnetic volume of RITU and the target section of SACRED. Under these conditions the counting rate in the central pixel of the detector, where the rate is highest, is ≈ 12 kHz. The rates in the pixels drop rapidly with distance from the centre despite the larger area of the outer pixels and deliberate defocusing of the beam at the target. The

electrostatic barrier potential was -35 kV for this experiment. The maximum cross-section for the reaction ^{208}Pb(^{22}Ne,4n)^{226}U is approximately 6 μb [Ye 94], compared to 300 μb for the dominant αxn channels to isotopes of Thorium. Although the efficiency of RITU for detection of the latter channel is much smaller than for the former, the use of some form of channel selection is necessary in order to retrieve events of interest. Channel selection in this case was achieved using the method of Recoil-Decay-Tagging (RDT) [Sh 79]. ^{226}U recoils were identified by requiring that their subsequent α-decay corresponded to the ^{226}U α-decay energy, at the same position in the Si-strip detector, within a maximum time interval of 800 ms (approx. three half-lives ($T_{\frac{1}{2}} = 260(10)$ ms [Gr 98] of ^{226}U). The search time of 800 ms was chosen in order to keep accidental correlations to a minimum. Only events in the energy range 7506-7608 keV were accepted as possible ^{226}U α-decays. This large energy acceptance was needed to account for the resolution of the PSSD of $\approx$ 30 keV. Using this method a total of 1230 recoils were tagged. A more detailed description of the techniques used is given in the following sections.

4.3 ^{254}No Experimental Details

In the second experiment a beam of 219 MeV ^{48}Ca was used with an average beam energy of 216 MeV, estimated at the centre of the target, corresponding to the maximum yield for ^{254}No. Two separate targets of 98% enriched ^{208}Pb were employed during the experiment. The first, a ^{208}Pb target of thickness 400μg/cm^2 was irradiated by a beam of 1.6 particle nA for approximately 106 hours. The second, a ^{208}Pb target of thickness 250 μg/cm^2 was irradiated by a beam of 3 particle nA for approximately 123 hours. The magnetic volume of RITU and the target section of SACRED were maintained at a helium gas pressure of 0.7 mbar for both experiments. In this experiment the electrostatic barrier was maintained at -40 kV for both runs. In the first run, 2440 recoils were detected and 4710 recoils were detected in the second. Unlike the ^{226}U experiment there were no competing compound channels. The target purity

of 98% ^{208}Pb ensures negligible competition from the reaction ^{207}Pb(^{48}Ca,2n)^{253}No [Og 01], and the combined population of ^{253,255}No from the 3n and 1n channels is $\approx$ 1% of that of ^{254}No [It 98, Za 01] making the use of the RDT technique unnecessary. For the reaction used in these experiments the nobelium recoils are sufficiently energetic to allow the use of a parallel plate proportional counter, placed in front of the silicon detector, for the identification of the nobelium recoils. However, to verify this procedure, RDT was used to select ^{254}No recoils by gating on their subsequent alpha decays in the energy range 7989-8169 keV and within a search time of 600s ($\approx$ 13 half lives ($T_{\frac{1}{2}} = 48(3)$s [Le 99]). Such a long search time would usually be problematic (increased probability of erroneous correlations), but in this experiment the effectiveness of the parallel plate proportional counter ensured that the probability of erroneous correlations was minimal. For details on the RDT method see section 4.5.

4.4   Si Strip Detector Analysis

The data obtained from the ^{226}U and ^{254}No experiments were analysed by essentially the same process. In this chapter the general steps carried out in analysing the data will be described, as well as individual sections describing steps in the analysis unique to each experiment. For each experiment the data analysis was carried out in two stages, the first stage concerning the data associated with RITU and the second stage concerning data associated with SACRED. Once these two preparatory analysis stages were completed, the data from RITU and SACRED were analysed in tandem using coincidence methods to produce the final electron spectra of interest.

4.4.1   Focal Plane Energy-Position Corrections

The energy observed in the Si-strip detector is dependent on the vertical position of the event in the detector (see section 3.6.2). This position dependence means that the sum energy for each strip[1] needs to be corrected for its position dependence in

---

[1]Obtained by adding the signal from the top and bottom strip

order to improve the resolution. Position and energy calibrations can be carried out using a calibration α source, or using known α lines produced in the reaction for each experiment. The latter method of calibration was used in the nobelium and uranium experiments. The sum energy for each Si strip in the detector is a combination of the top and bottom energy signals. Due to variations in resistance at each contact, different amplifier gains and possible non-uniformity in the resistance along each strip, the position dependence of each strip must be corrected. The energy position corrections were obtained by creating a 2-dimensional matrix of vertical event position on the x axis against α energy on the y axis for each strip, see figure 4.3 (a). The points from this plot were then extracted using a linear regression fit to obtain the gradient. The gradient was then used to correct the position dependence of each strip as follows:

$$E_{corr} = E_{sum} + \left(m \times 1024 \times \frac{E_{bot}}{E_{sum}} \right),$$

where E_{corr} is the position corrected sum energy, m is gradient obtained from the 2-dimensional gradient and 1024 is the constant which determines the maximum number of pixels in the y direction. Figure 4.3 (b), is the energy-position corrected matrix. The resultant corrections allow a position independent α spectrum to be obtained in the Si-strip detector, see figures 4.4. (a) and (b) for α spectra before and after correction respectively.

4.4.2 α-Energy Calibration

Once the position corrections have been made, each strip needs to be calibrated so that all α lines are aligned and at the correct energy. As stated in the previous section, the calibration was carried out using known α lines produced in the reaction. The following peaks were used in calibrating the ^{254}No experiment, ^{254}No 8093 $\pm$ 13 keV [Ak 01], ^{250}Fm 7436 $\pm$ 12 keV [Ar 98] and ^{246}Cf 6750.1 $\pm$ 15 keV [Sh 85]. The following peaks were used in the ^{226}U experiment, ^{222}Th 7982 $\pm$ 8 KeV [Ak 95], ^{219}Ra 7675 $\pm$ 5 keV [Br 01], ^{211}Po 74503 $\pm$ 5 keV [Br 92] and ^{224}Th 7170 $\pm$ 10 keV [Ar 97].
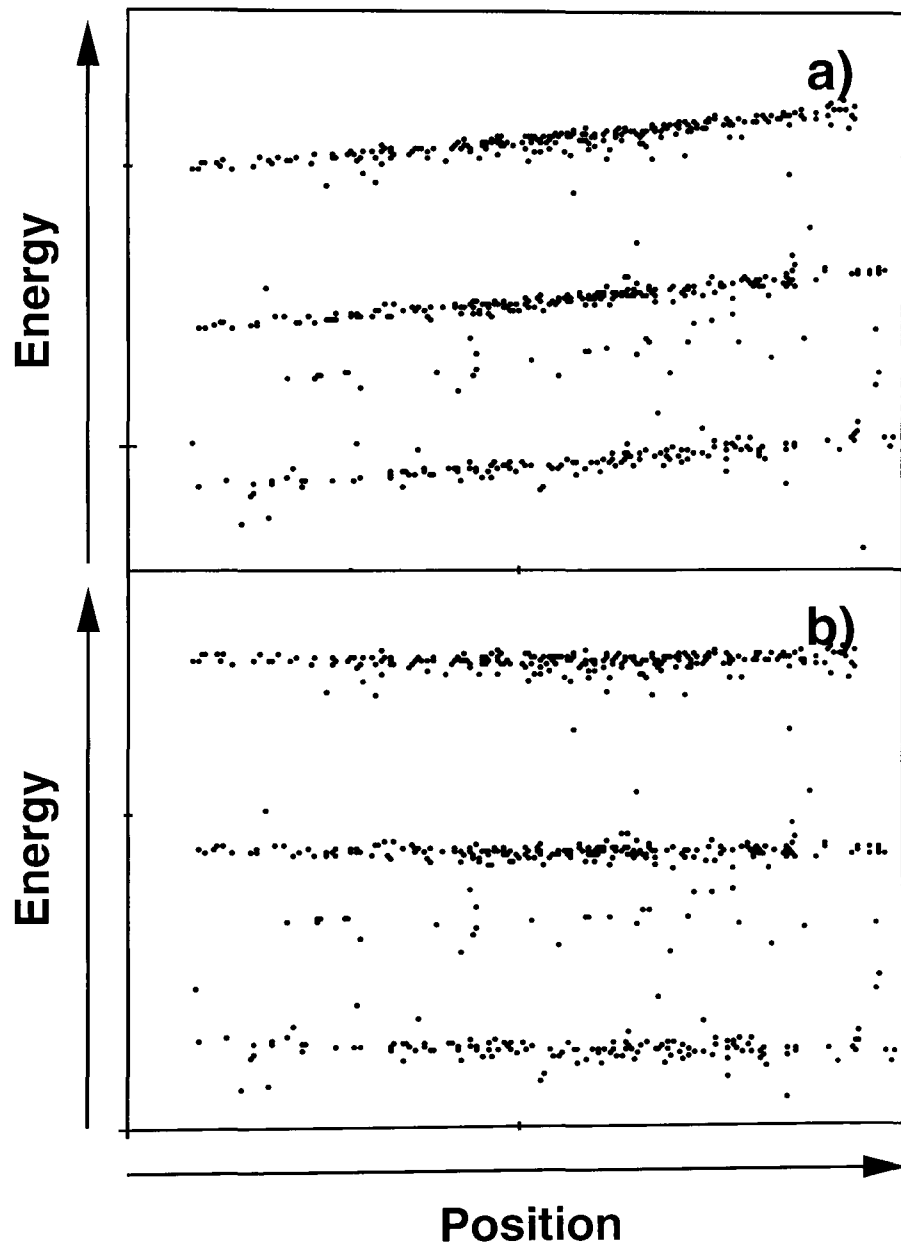
Figure 4.3: (a)Uncorrected energy plotted as a function of event position for a single strip in the PSSD. (b) Corrected energy plotted as a function of event position for a single strip in the PSSD.
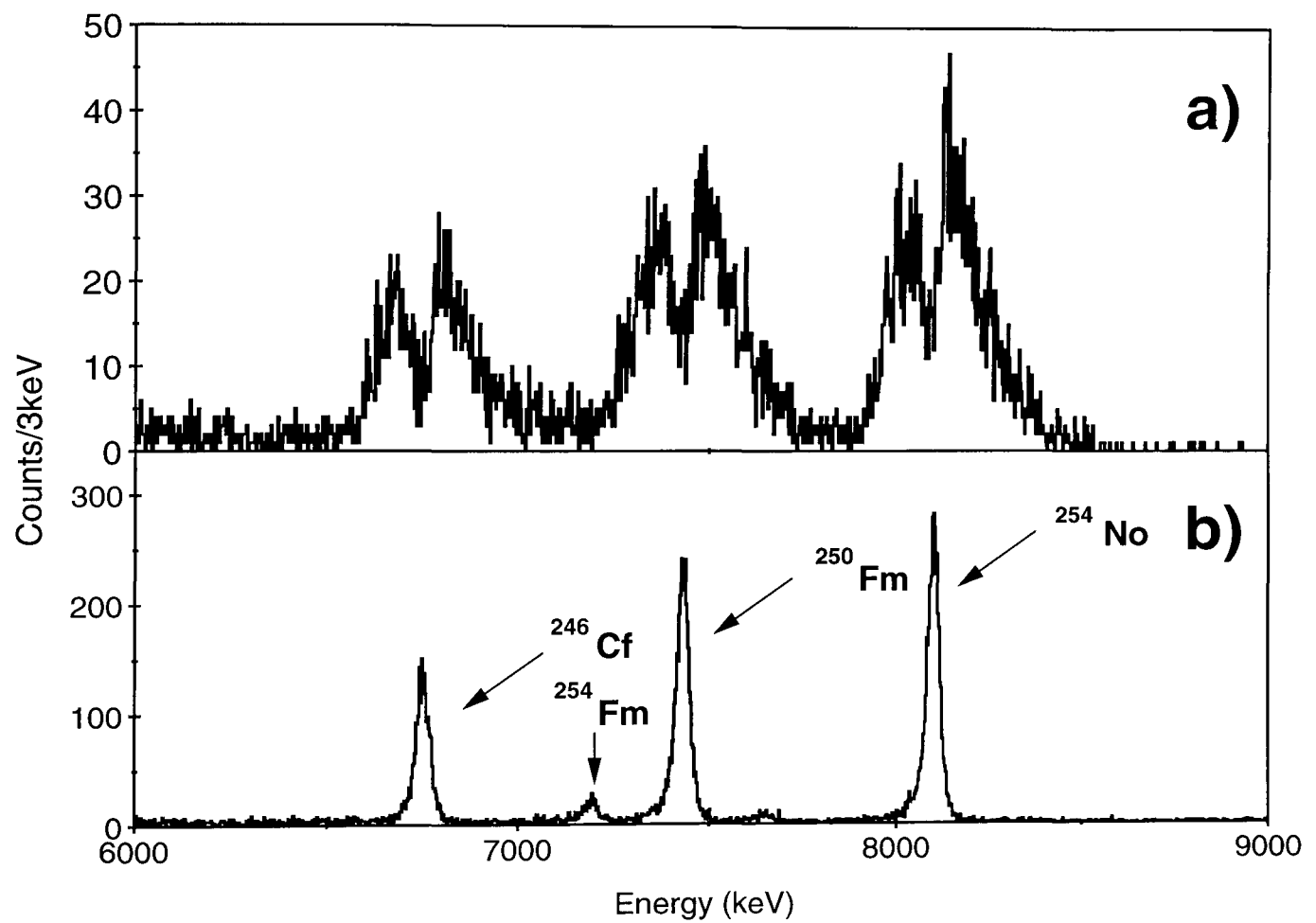
Figure 4.4: Figure a) shows the ^{254}No alpha decay sequence before energy position dependence corrections, b) shows the ^{254}No alpha decay sequence after energy position dependence corrections.
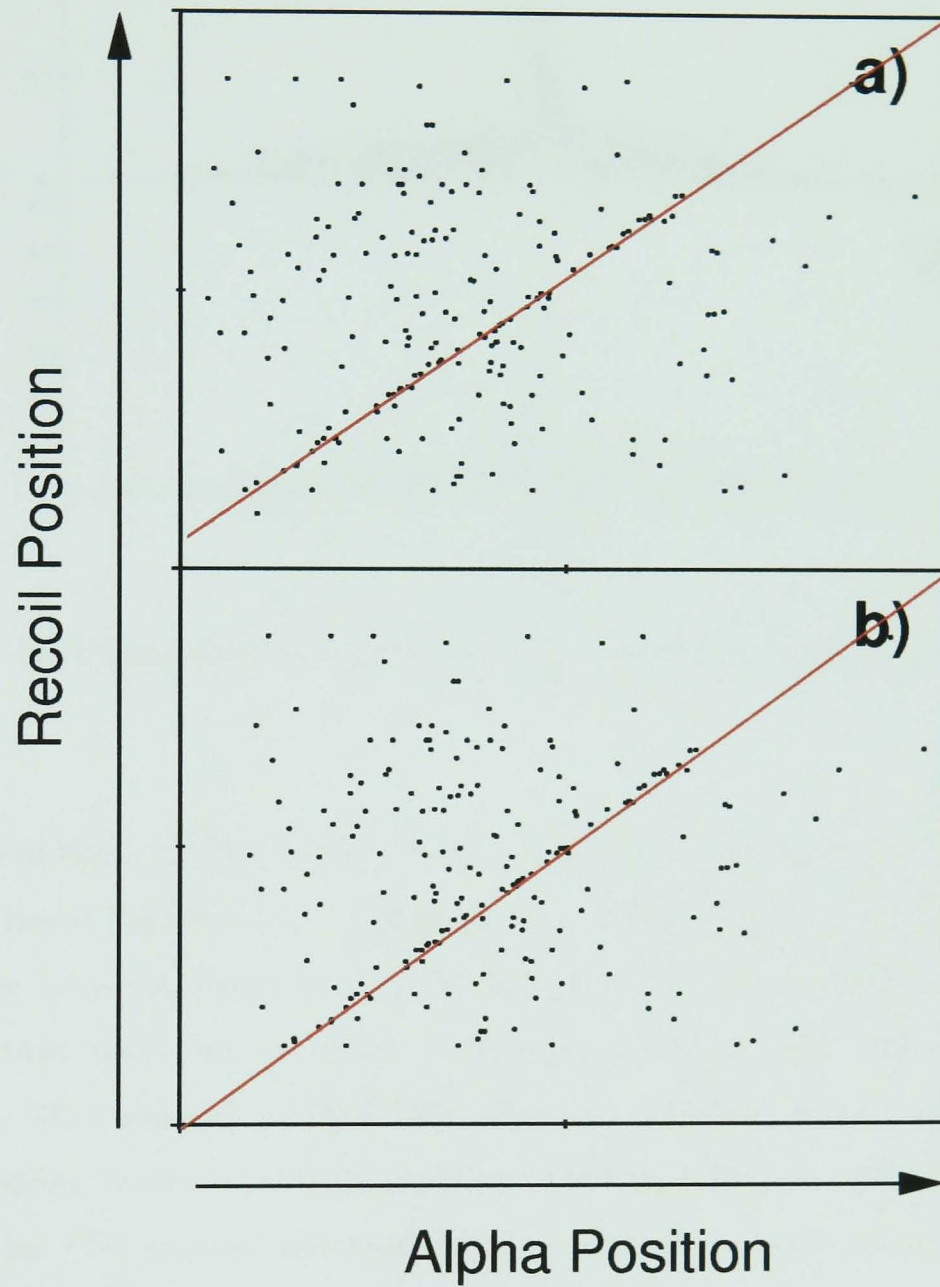
4.4.3 Alpha vs. Recoil Position Correction

The delayed coincidence method requires that the alpha particle from a decaying implantation is found and associated with its parent. This is achieved in the Si-strip detector by searching for the nearest event with the correct energy and within the shortest time. As stated previously, the Si-strip detector is connected to two amplifiers, a high gain amplifier to observe the alpha events and a low gain amplifier to observe the relatively higher energy recoils. The use of two amplifiers poses a problem in that there will be differences in the position read out for recoils and their subsequent alpha decay, thus increasing the probability of an incorrect correlation. In order to minimise this effect a 2-dimensional plot of correlated recoil position (yr) versus alpha position (yd) is produced for each strip, see figure 4.5a. A quadratic fit is taken of the line of points which is then used to correct the position differences between the alphas and recoils. A position corrected matrix should have a gradient of one and pass through the origin (yd=yr), as shown in figure 4.5b. This procedure was only necessary for the ^{254}No experiment where RDT was used to check the recoil gated spectra produced using the MWPAC[2]. In the ^{226}U experiment the recoils could be seen in the high gain amplifier making the low gain amplifier redundant. An illustration of the improvement gained through position corrections is shown by the matrix projections in figure 4.6.

4.4.4 Multi Wire Proportional Avalanche Counter

Recoil identification in the ^{254}No experiment was carried out using the MWPAC time of flight system which is able to distinguish between beam and recoils. The gas TAC is started by a MWPAC event and stopped by a delayed (to take into account flight time of recoil nuclei) electron event. So in effect the TAC is an indication of the time of flight of focal plane events. Many of these focal plane events will be scattered beam and scattered target nuclei. To distinguish recoils from these background events a 2 dimensional matrix was produced of energy in the Si-strip detector in the X axis

---

[2]Multi Wire Proportional Avalanche Counter

Figure 4.5: Figure a) Uncorrected recoil position plotted as a function of alpha position, b) Corrected recoil position plotted as a function of alpha position. The red lines indicate the trends in the data. Note that the data in b) conform to a straight line of gradient 1 passing through the origin.
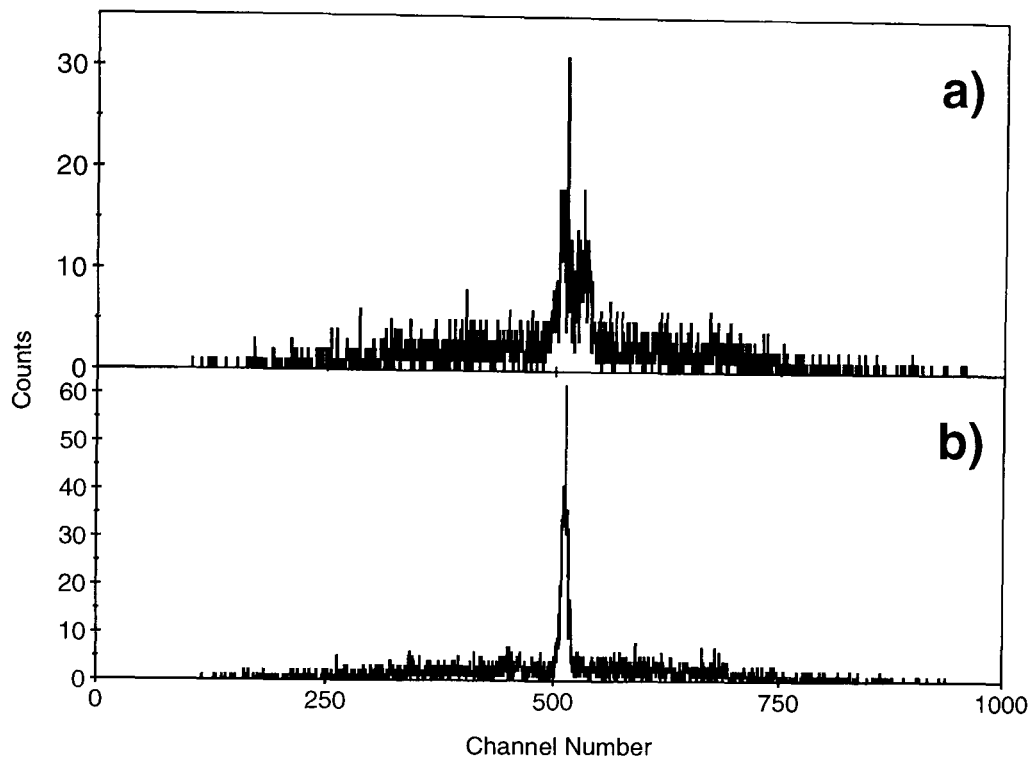
Figure 4.6: (a) Uncorrected y position difference spectrum (b) Corrected y position difference.

against time of flight (TOF) in the Y axis. A two dimensional gate was then placed around the recoil region shown in figure 4.7. This method of recoil identification proved to be very successful in the identification of ^{254}No recoils. This was due to the fact that there are no other competing channels other than fission. As a consequence, RDT analysis of the ^{254}No data was unnecessary and was used purely for cross checking the results obtained from TOF identification. The MWPAC could not be used for ^{226}U channel selection because of the low recoil energy.

The MWPAC was also used to clean up ^{254}No alpha spectra. This was achieved by simply vetoing all Si-strip events that occurred in coincidence with a MWPAC event, see figure 4.8 for an illustration of how the MWPAC was used to clean up a ^{254}No alpha spectrum.
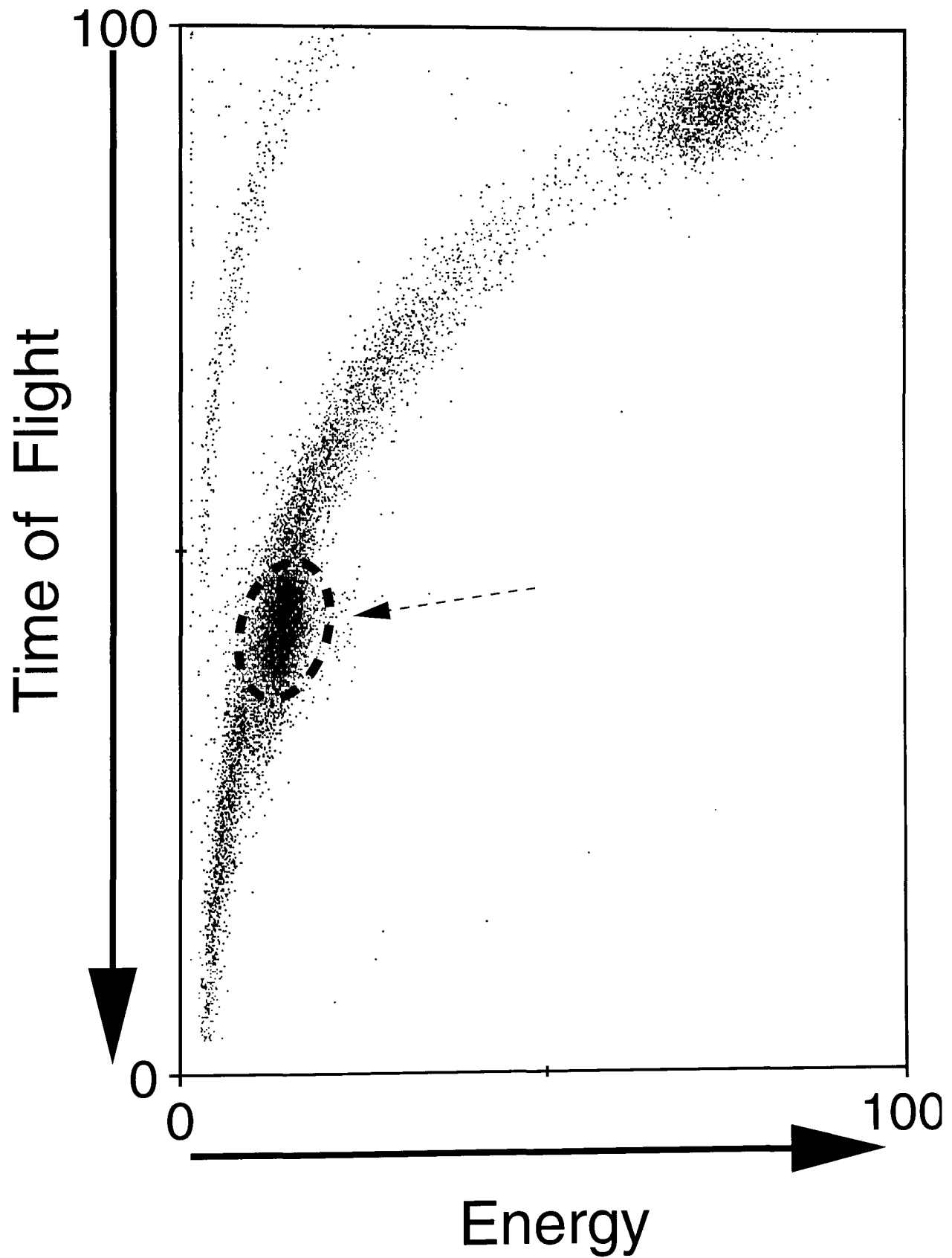
Figure 4.7: Focal plane energy vs. Time of Flight with arbitrary units on both axis. ^{254}No recoils are highlighted in the circled region.
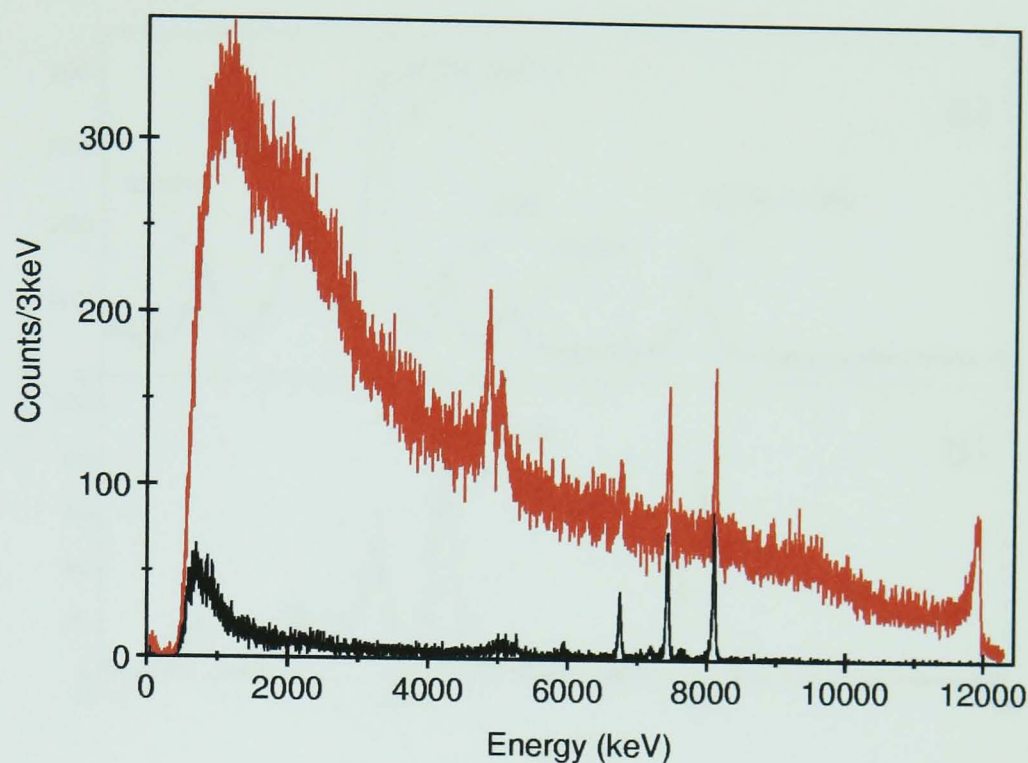
Figure 4.8: ^{254}No α spectra highlighting the effect of gas gating (MWPAC) on the RITU focal plane detector. The red spectrum shows the alpha spectrum obtained without using the gas counter veto. The black spectrum was incremented by demanding that the gas counter (MWPAC detector closest to the Si-detector) veto signal was not present. The black spectrum is thus cleaned by vetoing events which escape the Si-detector, causing incomplete energy deposition.

4.5 Recoil-Decay-Tagging Method

As mentioned in section 3.6.2 the gas-filled recoil separator RITU has a low mass resolving power. Therefore for reactions such as that used to produce ^{226}U where the MWPAC is unsuitable, recoil-decay-tagging (RDT) must be used to identify the fusion evaporation residues. The RDT technique requires a position sensitive Si-strip detector positioned at the focal plane of RITU and that the time of each event in the Si-strip is recorded. The method involves selecting two successive events which occur at the same position in the detector, within a specified search time. For the ^{226}U experiment the first event was only selected for correlation if the energy was approximately between 2 and 7 MeV, the energy corresponding to the observation
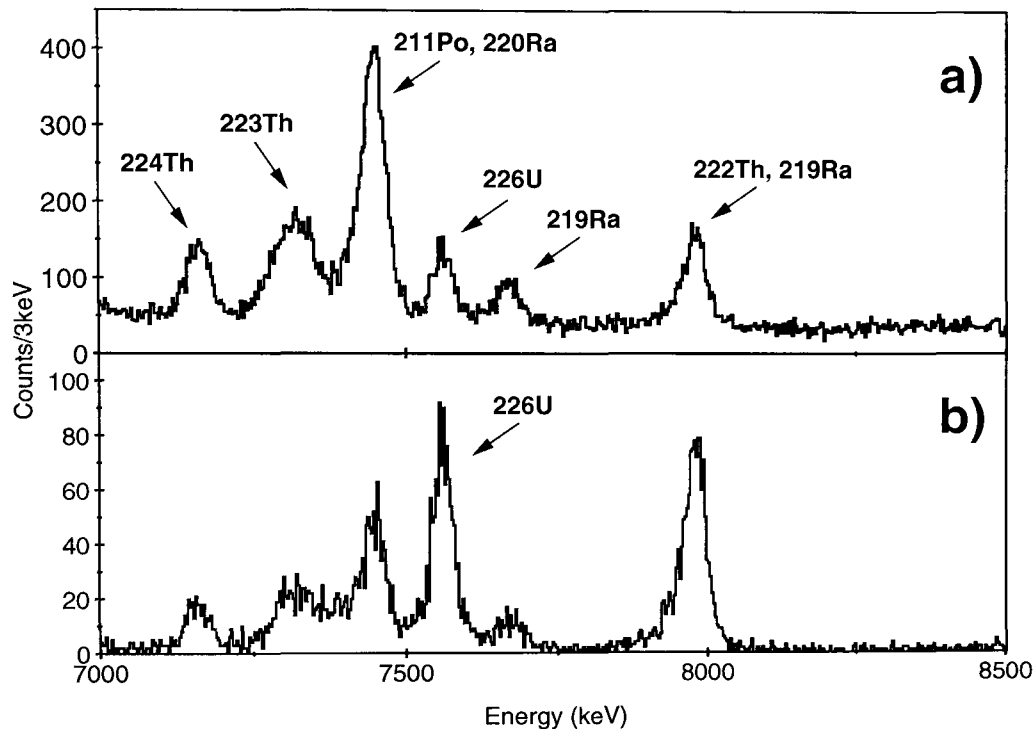
Figure 4.9: (a) Focal plane spectrum of alpha particles expanded on energy region of interest. (b) α events occurring up to 800 ms after the implantation of a recoil.

of a ^{226}U recoil. The second event was only selected if the energy was between 7506 and 7608 keV, the energy corresponding to the 7565±5 keV ^{226}U α decay. The search time used was approximately three ^{226}U half lives, or 800 ms. Using this technique 1230 correlated recoil-α pairs were identified. Figure 4.9 gives an illustration of the effectiveness of the RDT technique. The upper panel shows the α decay spectrum from the Si-strip detector, where there is a large amount of background and the ^{226}U α decays are obscured by adjacent peaks. The lower panel shows the α decay events which are correlated to an event in the fusion evaporation distribution within the 800 ms search time. Much of the background is reduced and as a result the ^{226}U α decay peak is more pronounced.

As discussed previously, RDT was also carried out in the ^{254}No experiment as a cross check. Recoil events were selected using the MWPAC as discussed in section 4.4.4 and subsequent events in the Si-strip detector were only selected if they were between 7989 keV and 8169 keV in energy. A search time of 600 s, $\approx$ 13 half lives was

used because the very clean recoil gating of the MWPAC meant that few accidental correlations were introduced by selecting such a long search time.

4.6 SACRED Data Analysis

The energy calibration of the individual SACRED detector elements was achieved using an open ^{133}Ba source in the target position; the response of the detector to the conversion electrons can be seen in figure 4.10. This source is generally chosen for electron calibration as it emits a broad energy range of conversion electrons from 40keV to 320keV. The calibrated electron energies are then corrected for Doppler shift and energy losses in the target for each individual experiment. The calibration is checked a number of times during and after the experiment to pick up any gain-shift that may have occurred during the experiment so that corrections can be made. Losses in the carbon foils are not taken into account because the foils are also present when calibrating the detector with a ^{133}Ba source.

4.6.1 Doppler Corrections

The collinear design of SACRED effectively eliminates the problem of Doppler broadening, but the Doppler shift of electrons emitted from a recoil must still be accounted for. The Doppler corrections used in this work were calculated using the SOLENOID Monte Carlo code [Bu 96]. The code models the emission and transportation of electrons, treated relativistically, from the recoiling nuclei to the detector. The average Doppler shift was calculated for many electron trajectories for a given input transition energy. The Doppler corrections were applied to the observed electron transitions and via an iterative process the input transition energies were adjusted until consistent transition energies and their Doppler shifts were reproduced. If the timing resolution of the detector could be improved in some way such that it was better than 1 ns then the exact electron emission angle θ' could be determined with sufficient accuracy so that the Doppler correction could be obtained more elegantly
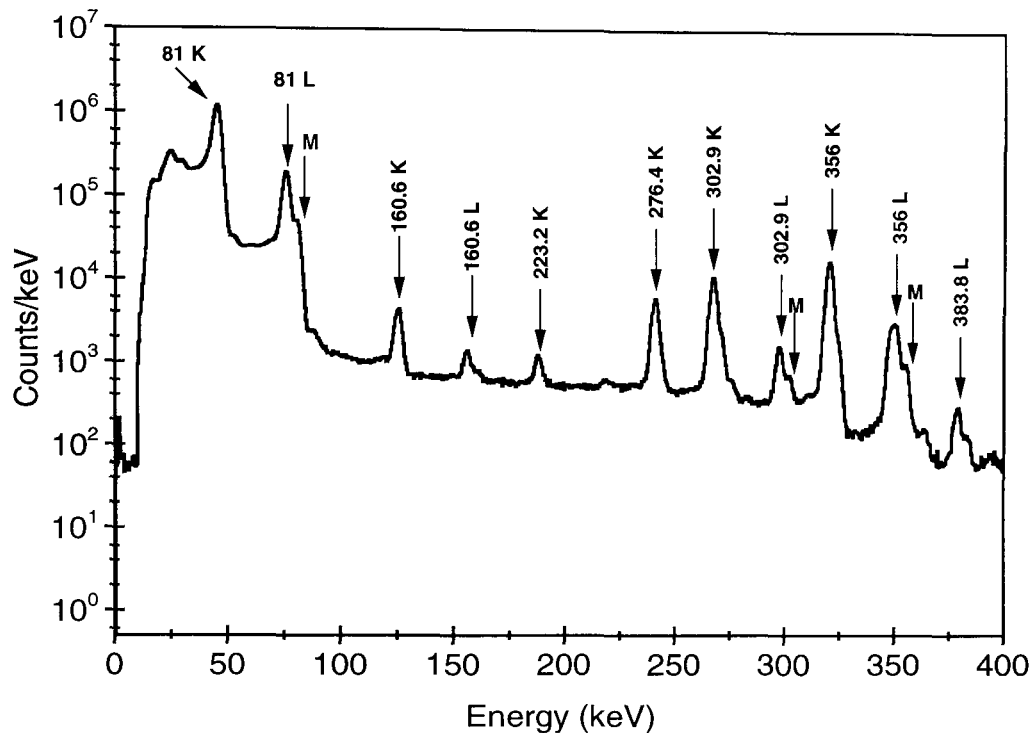
**Figure** 4.10: Spectrum of ^{133}Ba source, showing the detector response with no high voltage barrier.

using the following Doppler shift equation applicable to relativistic electrons:

$$E = \frac{E' + m - \beta cos\theta' \sqrt{E'^2 + 2mE'}}{\sqrt{1 - \beta^2}} - m,$$

where E' is the electron energy measured in the laboratory frame, E is the unshifted electron energy and θ' the emission angle measured in the laboratory frame. As an example of the magnitude of the Doppler shifts, the experimental 60.8 keV electron line in ^{226}U ($\beta \approx 0.0102c$) required the addition of a Doppler correction of ≈ 1 keV, while ≈ 4.8 keV was added to the 73.15 keV electron line in ^{254}No ($\beta \approx 0.0186c$). An illustration of the magnitude of Doppler shifts for various values of β is given in figure 4.11.

4.6.2 Recoil-Electron TDC

Each SACRED detector element has an associated TDC which is started by a logical pulse event in the Si-Strip detector and then stopped by a logical pulse from an event
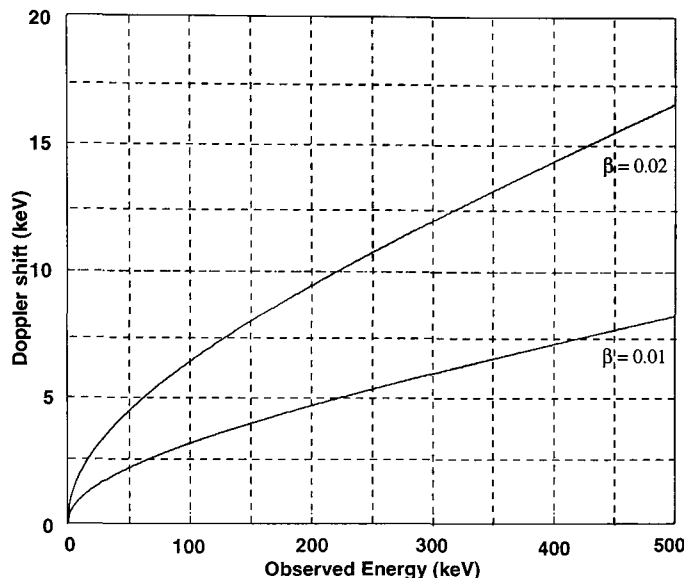
Figure 4.11: Doppler shift as a function of observed electron energy for given recoil velocities $\beta(=\frac{v}{c})$ values at $\theta = 160°$.

in the SACRED detector. The TDCs are needed to pick out genuine prompt electrons because the master gate, although triggered by events in the Si-strip detector as with the TDCs, has a much wider coincidence gate in the electronics allowing for non genuine prompt coincidences to be read out. Figures 4.12a and 4.13a show the total TDC spectra for the ^{226}U and ^{254}No respectively, the genuine prompt electrons giving rise to the peak. Truly prompt electrons can then be selected by only selecting events which form the peak in each TDC. The TDC spectra shown in figures 4.12a and 4.13a, contain a large amount of background, this is due to the fact that the TDCs are started by any event in the Si-strip detector such as α particles and scattered beam. This contribution can be greatly reduced, as shown in figures 4.12b and 4.13b, and in the process improve the number of genuine prompt coincidence electrons by the use of energy coincidence gates and RDT in the case of ^{226}U and recoil gating using the MWPAC in the case of ^{254}No.
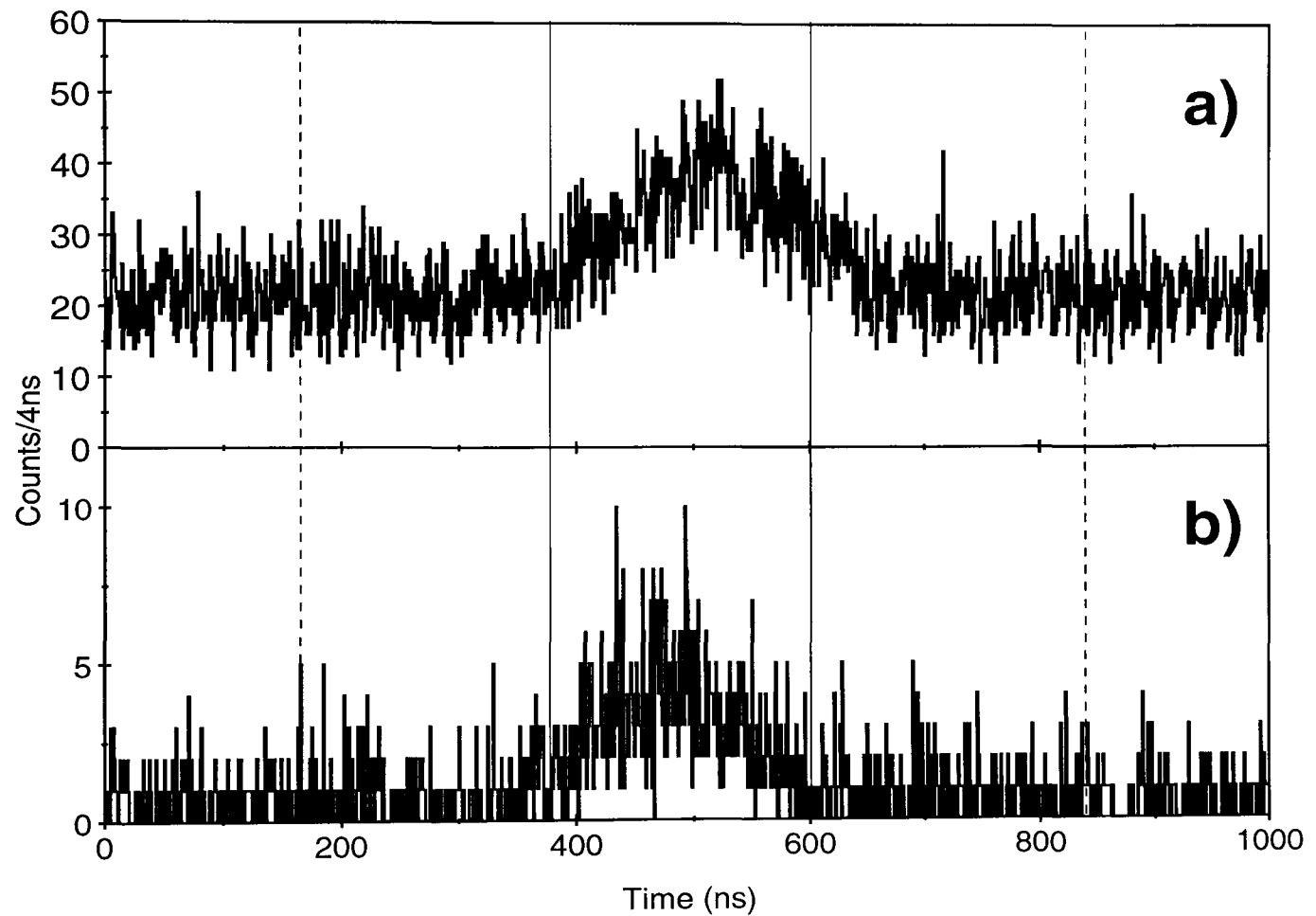
Figure 4.12: (a) TDC started by a recoil event in the focal plane and stopped by the detection of an electron in the target position. (b) The same as (a) but in coincidence with recoils correlated to the decay of ^{226}U. The region between the solid lines represents the prompt TDC gate used in the experiment. The region between solid and dashed lines either side represents the gates used to create the background contribution.
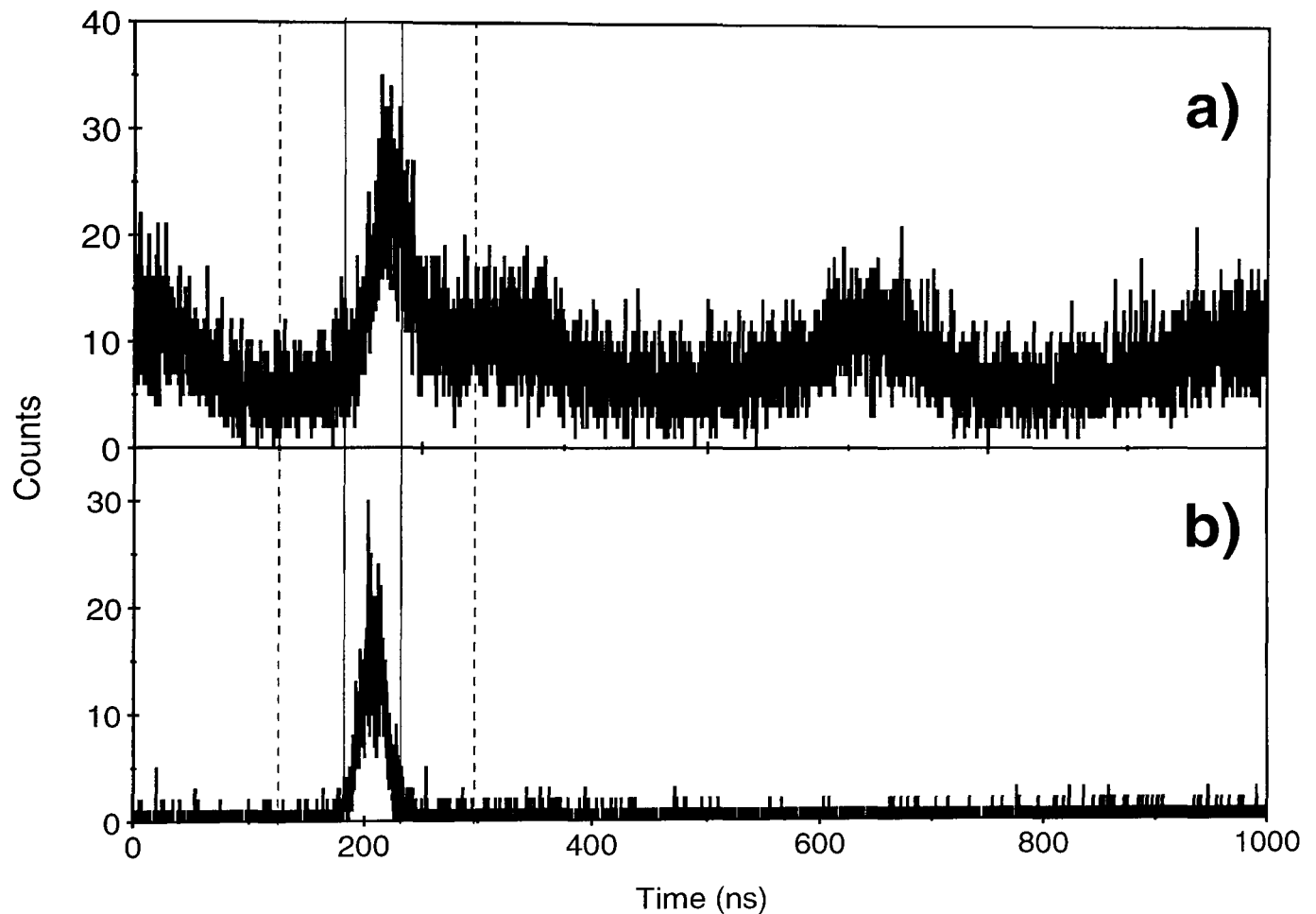
Figure 4.13: (a) TDC started by a recoil event in the focal plane and stopped by the detection of an electron in the target position. (b) The same as (a) but in coincidence with recoils correlated to ^{254}No using the MWPAC. The region between the solid lines represents the prompt TDC gate used in the experiment. The region between solid and dashed lines either side represents the gates used to create the background contribution.
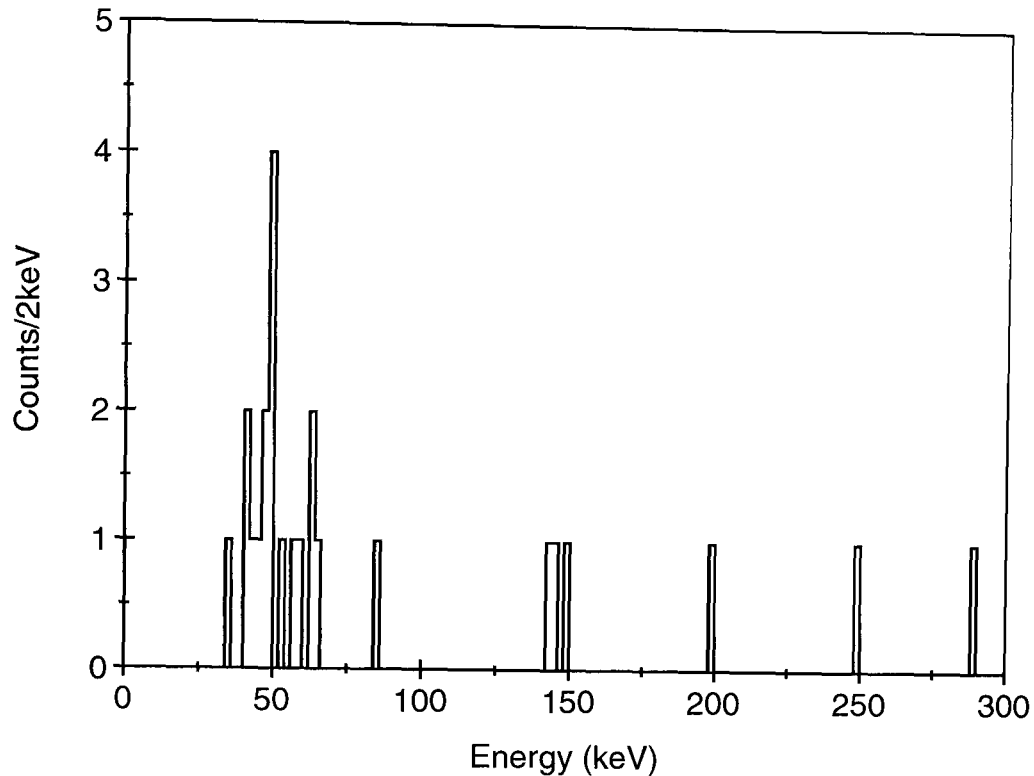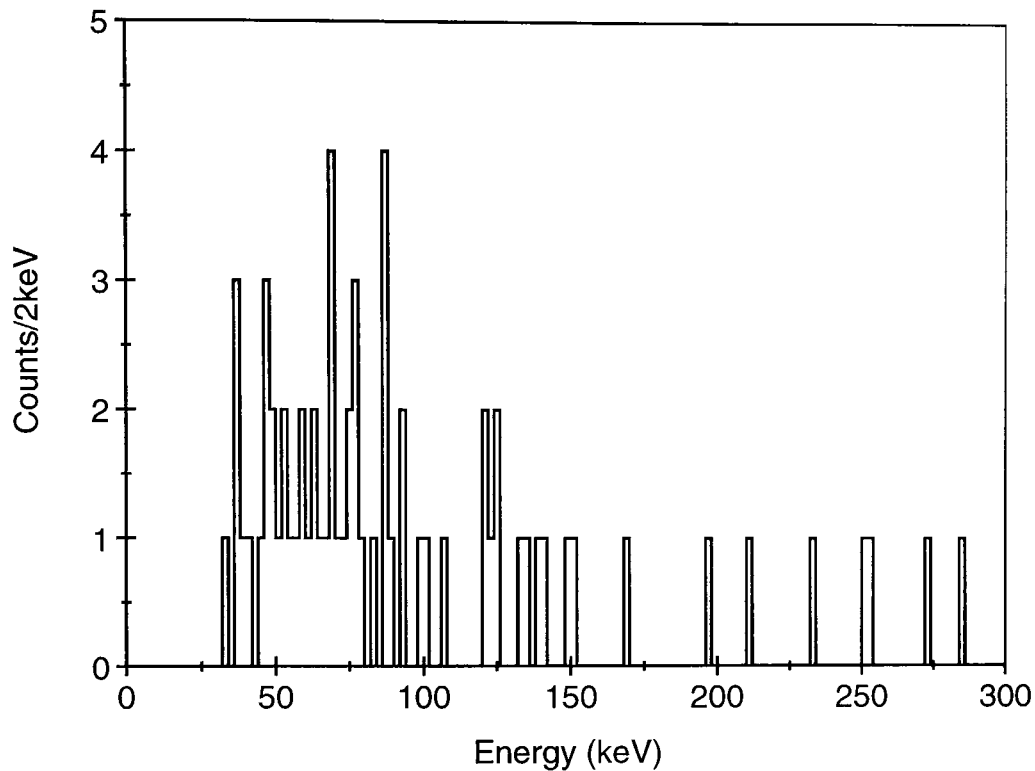
Figure 4.14: Normalised random background contribution taken from regions either side of prompt TDC peak for ^{226}U .

4.6.3 Background Analysis

Some of the background present in the electron spectra for both ^{226}U and ^{254}No can be removed by considering the contribution of background events under the recoil-electron TDC. An estimation of the contribution from such events can be obtained by producing an electron spectrum coincident with events on either side of the prompt TDC peak, shown in figure 4.12b. The contribution in ^{226}U is shown in figure 4.14, where the random background contributions from either side of the prompt TDC peak are added together and then normalised to the width of the prompt TDC peak. The same procedure was also carried out for the ^{254}No experiment but the contribution from background events from under the recoil-electron TDC was found to be insignificant compared to the total number of counts, see figure 4.15.

Figure 4.15: Normalised random background contribution taken from regions either side of prompt TDC peak for ^{254}No .

4.6.4 Background Calculations in ^{254}No

In order to gain insight into the origin of the pronounced background in ^{254}No the area of the background was measured using a distribution of the form:

$$f(E) = a \cdot \left(1 - \sqrt{\frac{b}{E}}\right) \exp(c \cdot E),$$

to match the shape and area of the background, where a is proportional to the maximum value the function rises to, b represents the low cutoff point and c determines the exponential tail. For an illustration of the fitting process see figure 4.16. Two background fits were made in order to make an approximate quantitative measure of the background error. The two fits were taken as the largest and smallest acceptable approximations of the background. Background fits were taken for both *singles* and multi-fold electron spectra, so that the background electron multiplicity could also be measured. The background fits were further used to provide background subtracted spectra for the purposes of transition energy and intensity measurements.
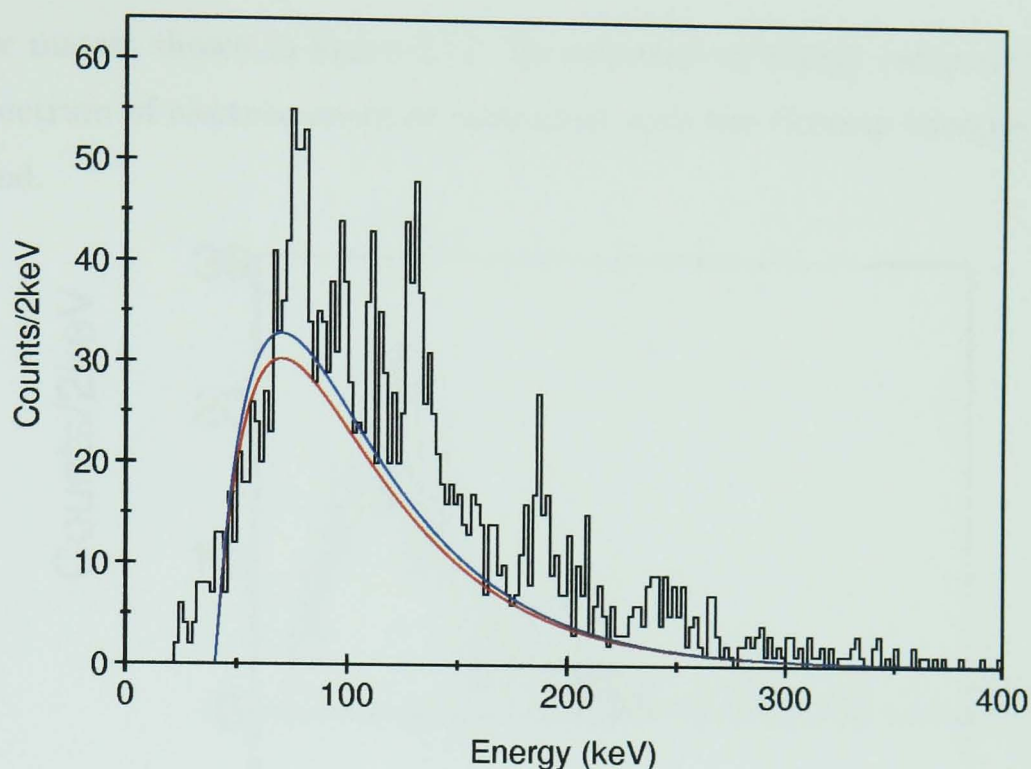
Figure 4.16: ^{254}No spectrum showing the fits used for background measurement and subtraction. The blue (a = 650, b = 20, c = -0.045) and red (a = 600, b = 20, c = -0.045) lines are the upper and lower fits respectively.

4.6.5 Recoil Tagged Electron-Electron Coincidence Data

SACRED is a multi-element array, and as such can detect more than one electron at a time in coincidence with a recoil. Electron-electron coincidence data are a very useful tool in level scheme analysis, and this section describes how the electron-electron matrices were analysed. The ^{254}No data were analysed by creating an electron-electron fold two matrix coincident with ^{254}No recoils. Higher fold events can be *unpacked* into fold two events, for example a fold four event can be broken down into six fold two events. The number of combinations can be calculated using:

$$_mC_n = \frac{m!}{n!(m-n)!},$$

where m is the original fold number and n is the fold number after unfolding. The fold two electron-electron matrix contains fold two events of energies E_{e1} and E_{e2} which are represented by points at (E_{e1}, E_{e2}) and (E_{e2}, E_{e1}) in the matrix, producing a

symmetric matrix shown in figure 4.17. By selecting an energy range or *gate* on one axis, a spectrum of electron energies coincident with the electron energies of the gate is produced.
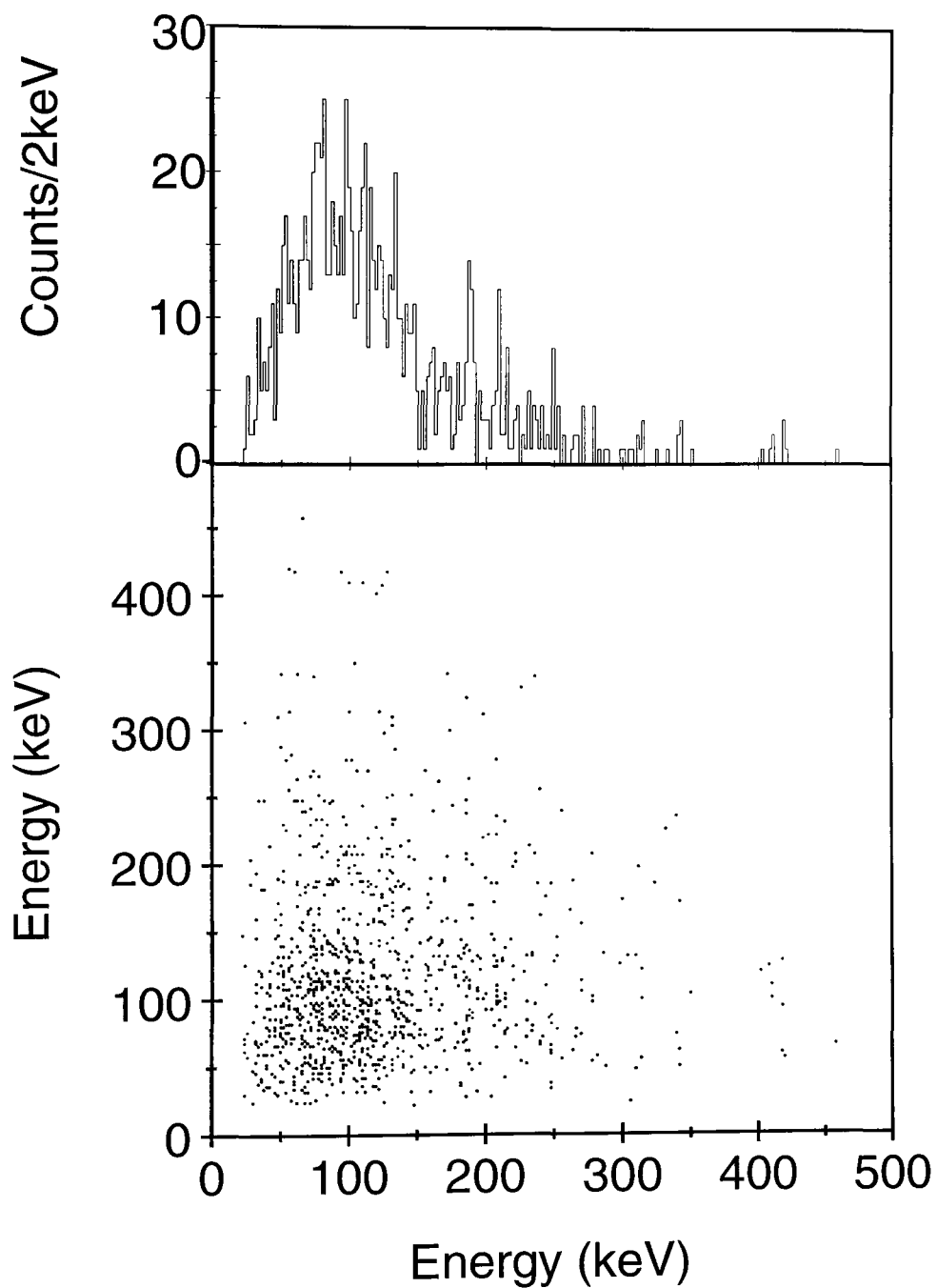
Figure 4.17: Recoil gated E_e - E_e matrix showing coincidences between the ground state band in ^{254}No nuclei. The top panel shows the total projection of the matrix.
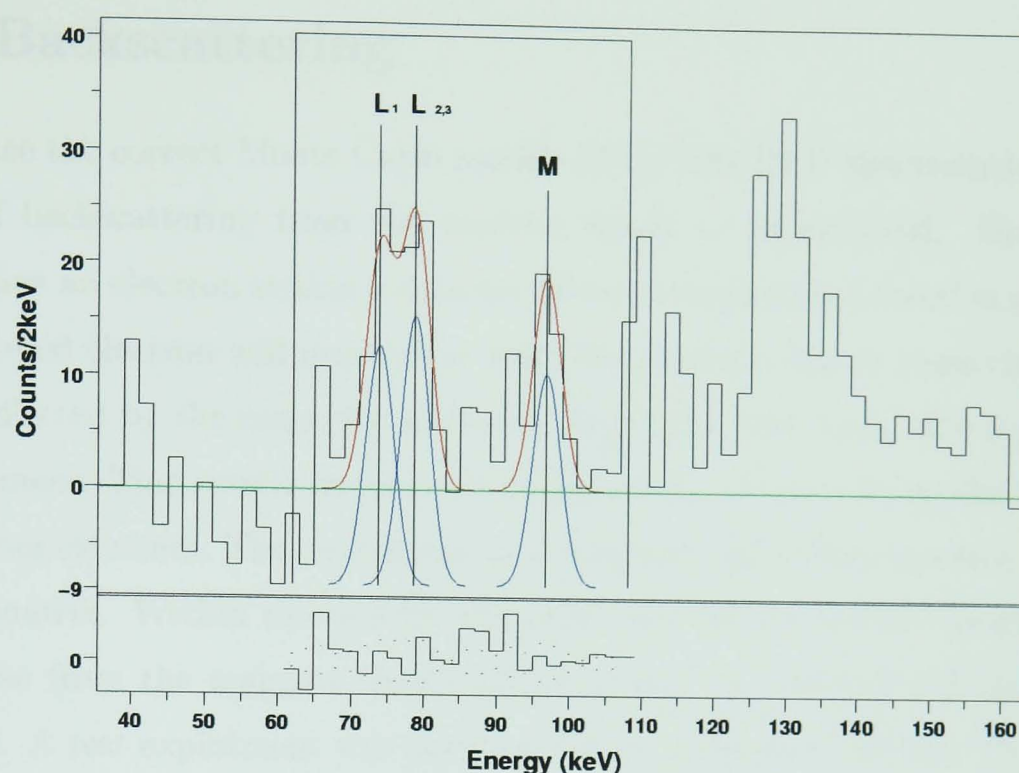
Figure 4.18: Example of an electron energy and intensity measurement using ^{254}No recoil gated electrons. The red curves show the fit, the blue curves show the decomposition and the bottom panel shows the residuum fit. The green line is the background subtraction (set to 0 for this example).

4.6.6 Electron Energy and Intensity Measurement

Once all the previous procedures have been carried out the end result is a recoil or recoil decay tagged electron spectrum from which energy and intensity measurements can be taken. Energy and intensity measurements were made using the spectra and matrix analysis program Tv[3]. Figure 4.18 shows an example fit on the $4^+ \rightarrow 2^+$ transition in ^{254}No, for simplicity the background subtraction has been set to zero. Although a large majority of the background is removed prior to analysis in Tv, background regions are selected in Tv when required to obtain accurate energy and intensity measurements.

---

[3]http://hydra.ikp.uni-koeln.de~fitz/

4.7   Backscattering

To produce the correct Monte Carlo models of the SACRED spectrometer, the magnitude of backscattering from the detector needs to be explored. Backscattering occurs when an electron strikes a detector element, imparting a fraction of its energy. The scattered electron will move away from the detector, but in some circumstances will be reflected by the magnetic solenoidal transport field, back onto a different detector element. This results in the total energy of the electron being divided between two detector elements. The easiest way to measure the effect is to produce an electron-electron matrix. Within the matrix, diagonal lines with a negative gradient of one, which arise from the magnetic backscattering, can be observed and their intensity measured. A test experiment was performed with a beam of 219 MeV ^{48}Ca on a 400 μg/cm^2 thick ^{124}Sn target. The reaction produces an abundance of conversion electrons making it an ideal reaction to measure the backscattering effect. Figure 4.19 shows the recoil electron-electron matrix used to measure the backscattering effect. While using the ^{133}Ba source would seem the obvious choice to measure the backscattering effect, the recoil trigger needed to clean the spectra is not available when taking source measurements.
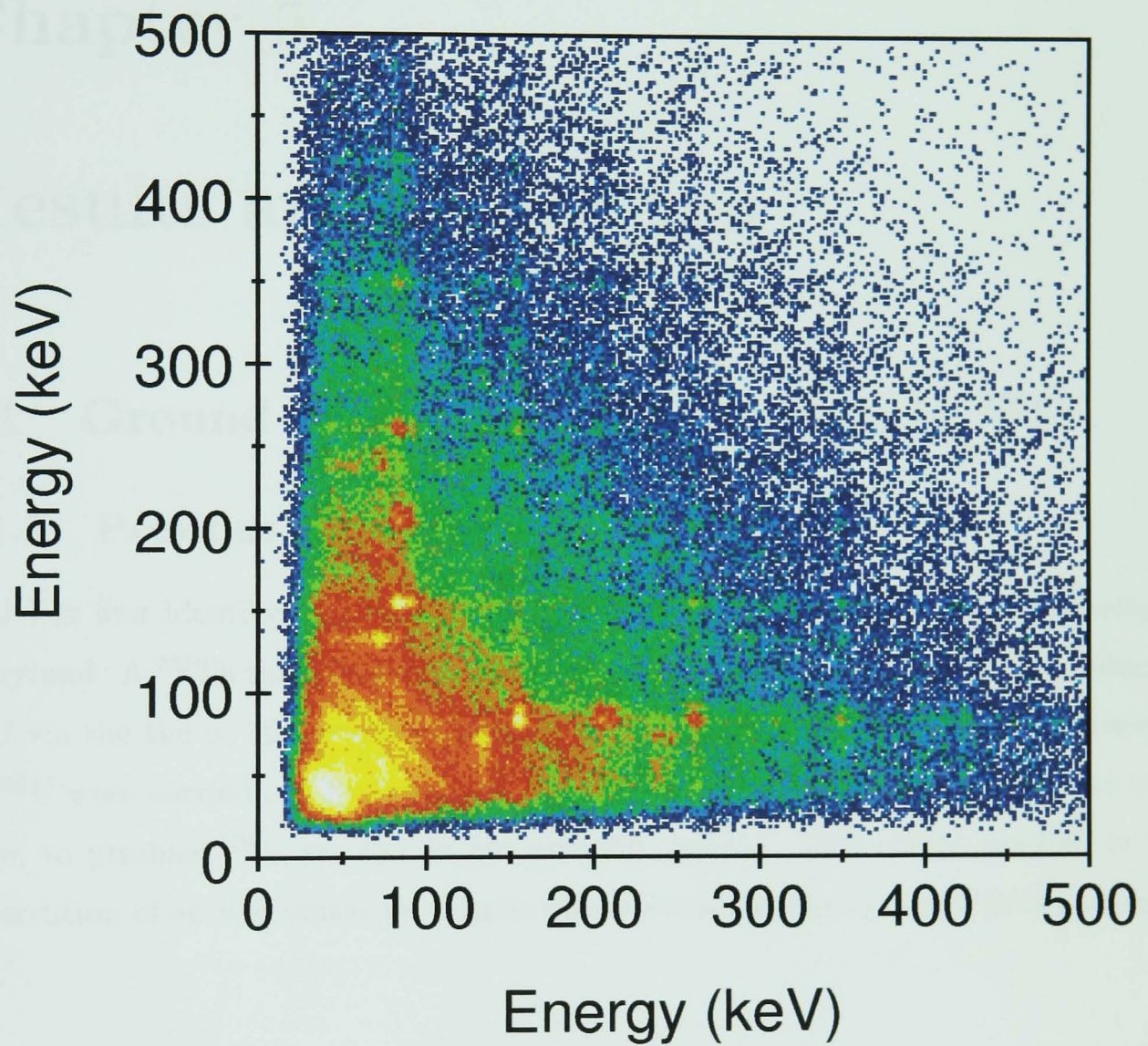
Figure 4.19: Recoil gated E_e - E_e matrix showing coincidences between the ground state bands in ^{165,166}Yb nuclei and diagonal lines due to backscattered electrons.

Chapter 5

Results and Discussion

5.1 Ground State Band Observations in ^{226}U

5.1.1 Previous Work

^{226}U was first identified by Viola *et al.* [Ve 73] in an experiment at the University of Maryland. A ^{232}Th target was irradiated with a beam of 140 Mev ^{4}He ions, producing ^{226}U via the the α, 10n evaporation channel. The first in-beam γ-ray measurements of ^{226}U were carried out by Greenlees *et al.* [Gr 98]; irradiating a ^{208}Pb target with ^{22}Ne, to produce ^{226}U via the 4n evaporation channel. Their work resulted in the observation of excited states up to spin 14$\hbar$ and evidence for octupole deformation in ^{226}U .

5.1.2 Results

Figure 5.1 shows the background corrected conversion electron spectrum of ^{226}U, in which the conversion electrons from the $2^+ \rightarrow 0^+$ and $4^+ \rightarrow 2^+$ transitions can be observed. The in-beam energy resolution of SACRED is typically 5-6 keV, insufficient to fully resolve the L_2 and L_3 subshell components (3.78 keV separation) and the various M subshells (< 1 keV separation). The efficiency of SACRED for the 81.3 keV L and M lines is reduced largely because of the effect of the electrostatic barrier

but also because of the high timing discriminator settings in this experiment. The collinear design of SACRED effectively eliminates the problem of Doppler broadening, but the Doppler shift of electrons emitted from a recoil must still be accounted for (see section 4.6.1). Energy losses in the target are taken into account although losses in the carbon foils are ignored because the foils are also present when calibrating the detector with a ^{133}Ba source. In order to calculate the transition energy from the composite L and M peaks an average binding energy is needed. Using conversion coefficients from Rösel *et al.* [Rö 78] the relative intensities of the various subshells were calculated, and using this information a weighted binding energy for the L and M atomic shells was produced for each observable energy transition. The weighted binding energy was then used in conjunction with the corrected electron energies to determine the energy of the given line. Table 5.1 shows the electron energy of the observed L and M lines, along with the derived transition energy, E_γ. The relevant intensities are given in table 5.2.

The observed transition energies have been added to the partial level scheme from previous work by Greenlees *et al.* [Gr 98], and can be seen in figure 5.2. From table 5.1 it can be seen that the energies measured here are in good agreement with the measured and predicted energies made by Greenlees *et al.* [Gr 98]; therefore, the intrinsic dipole moment measurement estimate [Gr 98] of $|D_0| = 0.58(7)\text{fm}^2$, made using the estimated $2^+ \rightarrow 0^+$ transition energy in table 5.1(b), is confirmed. Likewise the intrinsic quadrupole moment estimate of 740(80) fm^2 is also confirmed.

Table 5.1: Measured energies for ^{226}U. Column (a) lists the transition energies deduced here. Column (b) lists the transition energies estimated by Greenlees *et al.* [Gr 98].

$I_i^{\pi i}$	$I_f^{\pi f}$	E_L	E_M	E_γ (a)	E_γ (b)
2^+	0^+	60.8(5)	78.2(7)	81.3(6)	80.5(5)
4^+	2^+	148.2(4)	162.51(6)	167.8(4)	168.7(6)
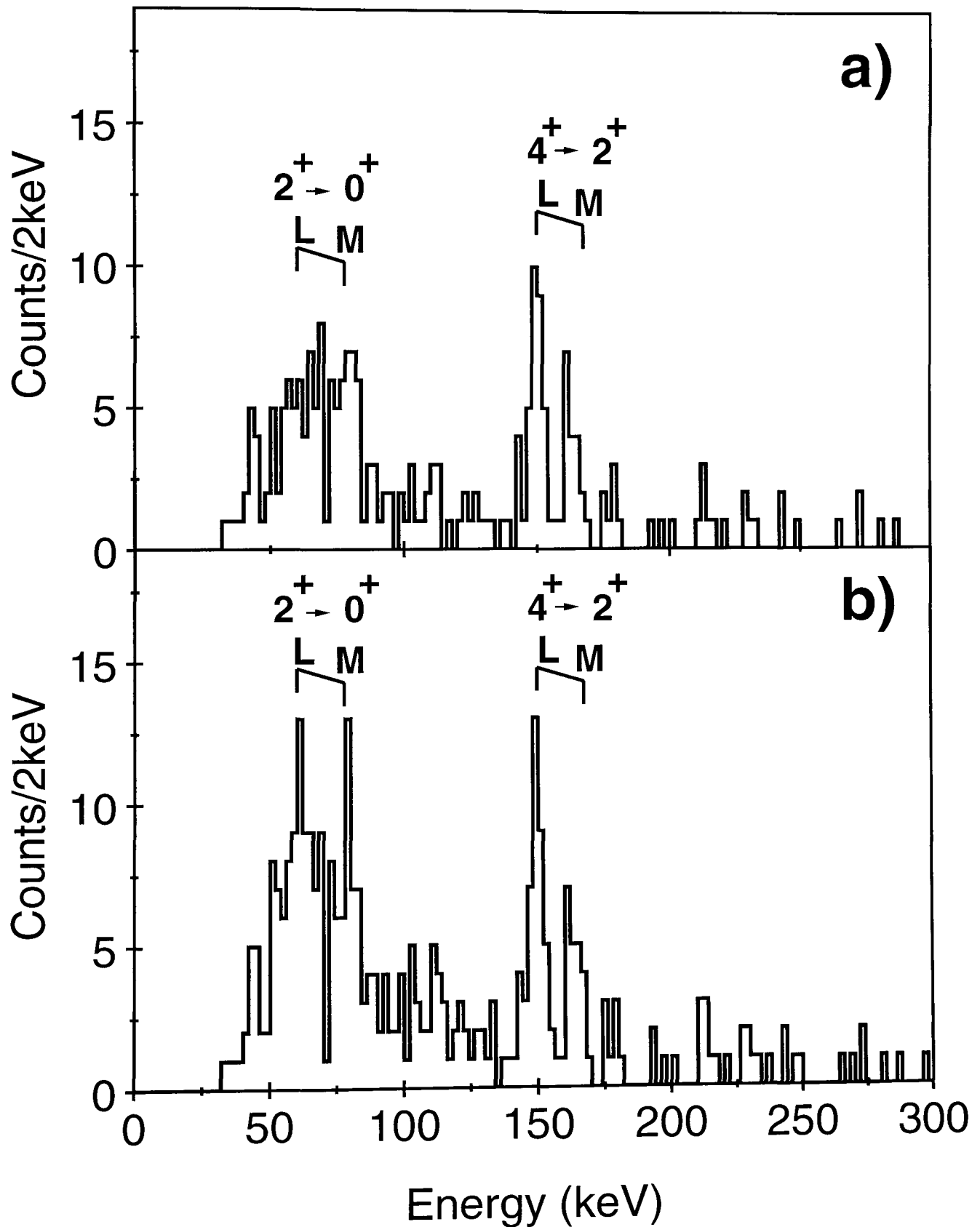
Figure 5.1: (a) Single fold electron energy spectrum in coincidence with recoils correlated to the decay of ^{226}U. (b) Electron energy spectrum in coincidence with recoils correlated to the decay of ^{226}U. The poor statistics of the 81.3 keV L and M lines in (a) is because of the

Table 5.2: Measured intensities for ^{226}U. The counts column lists the sum of the L and M electron counts experimentally observed. Intensity column (a) lists the electron intensities corrected using the energy dependent absolute efficiency curve. Column (b) lists the electron intensities per 1000 recoils. Column (c) lists the total transition intensities corrected using tabulated values of internal conversion coefficients [Rö 78]. Column (d) lists the total transition intensities per 1000 recoils. Column (e) lists the transition intensities, from Greenlees *et al.* [Gr 98], normalised to 100 for the $6^+ \rightarrow 4^+$ transition.

$I_i^{\pi i}$	$I_f^{\pi f}$	Counts	Intensity (a)	Intensity (b)	Intensity (c)	Intensity (d)	Intensity (e)
2^+	0^+	45(9)	850(210)	690(170)	870(220)	710(180)	250(90)
4^+	2^+	42(9)	490(100)	400(80)	690(140)	560(110)	190(30)
6^+	4^+						100(8)
8^+	6^+						35(7)
10^+	8^+						14(3)
12^+	10^+						7(2)

5.2 Ground State Band Observations in ^{254}No

5.2.1 Previous Work

^{254}No was first identified by Ghiorso *et al.* [Gh 58] in an experiment at Berkeley, California. A ^{246}Cm target was irradiated with a beam of ^{12}C, producing ^{254}No via the 4n evaporation channel. Ghiorso *et al.* [Gh 73] later went on to discover a 0.28 ± 0.04 s isomeric state in ^{254}No , and suggested the existence of the isomeric state was due to a $K^\pi = 8^-$ two-quasiparticle state. The first in-beam γ-ray measurements of ^{254}No were carried out by Reiter *et al.* [Re 99] and Leino *et al.* [Le 99]; irradiating ^{208}Pb targets with beams of ^{48}Ca, to produce ^{254}No via the 4n evaporation channel. Their
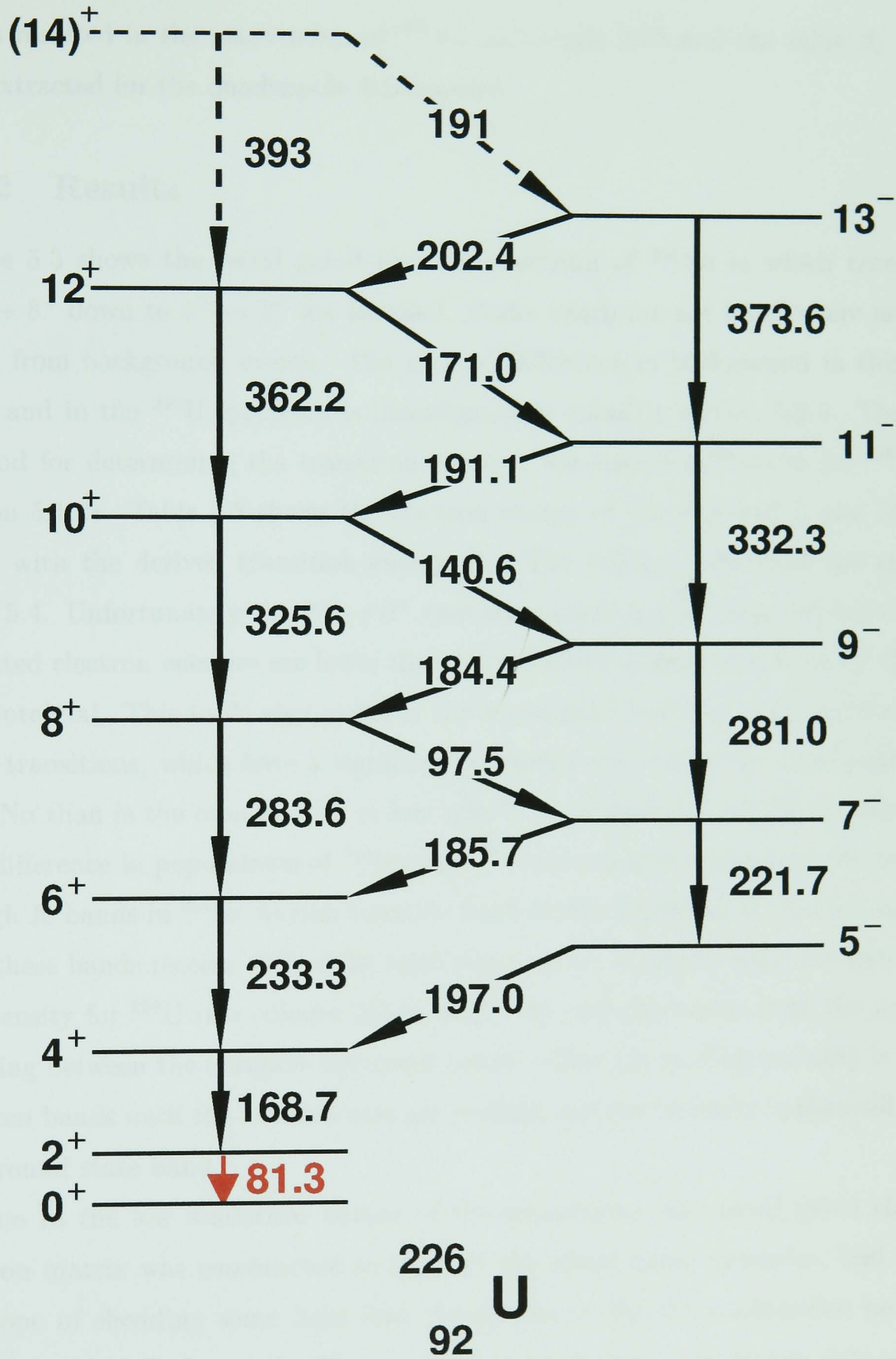
Figure 5.2: Partial level scheme for ^{226}U. The transition identified for the first time, in this work is labelled in red.

works resulted in the observation of ^{254}No up to spin 20 $\hbar$ and the value $\beta_2 = 0.27$ was extracted for the quadrupole deformation.

5.2.2   Results

Figure 5.3 shows the recoil gated electron spectrum of ^{254}No in which transitions $10^+ \rightarrow 8^+$ down to $4^+ \rightarrow 2^+$ are labelled. Peaks which are not labelled are assumed to be from background events. The marked difference in background in this spectrum and in the ^{226}U spectrum is investigated in detail in section 5.2.3. The same method for determining the transition energies was used for ^{254}No as for ^{226}U (see section 5.1.2). Table 5.3 shows the electron energy of the observed L and M lines, along with the derived transition energy E_γ. The relevant intensities are given in table 5.4. Unfortunately the $2^+ \rightarrow 0^+$ transition could not be observed because the expected electron energies are lower than the 40 keV threshold produced by the barrier potential. This table also contains the measured intensities of the ground state band transitions, which have a significantly smaller fraction of the total population of ^{254}No than is the case in ^{226}U at low spin (see columns (c) and (d) in table 5.2). The difference in populations of ^{254}No and ^{226}U presumably arises from the presence of high K bands in ^{254}No having isomeric band heads. Butler *et al.* [Bu 02] estimate that these bands receive 40% of the total population. At higher spins the sharp drop in intensity for ^{226}U (see column (d) in table 5.2) probably arises from the intensity splitting between the octupole deformed bands, where the feeding intensity is shared between bands until the lowest states are reached and the intensity is channelled into the ground state band.

Due to the low statistical nature of the experiment, the recoil gated electron-electron matrix was constructed to support the recoil gated spectrum, and also in the hope of shedding some light into the origins of the the unidentified peak and the pronounced background. The recoil-electron-electron coincidence data support the level scheme, although no additional information can be obtained due to the low statistics, see figures 5.6(a)-(e). The gates used to generate spectra in panels (b)-(e)
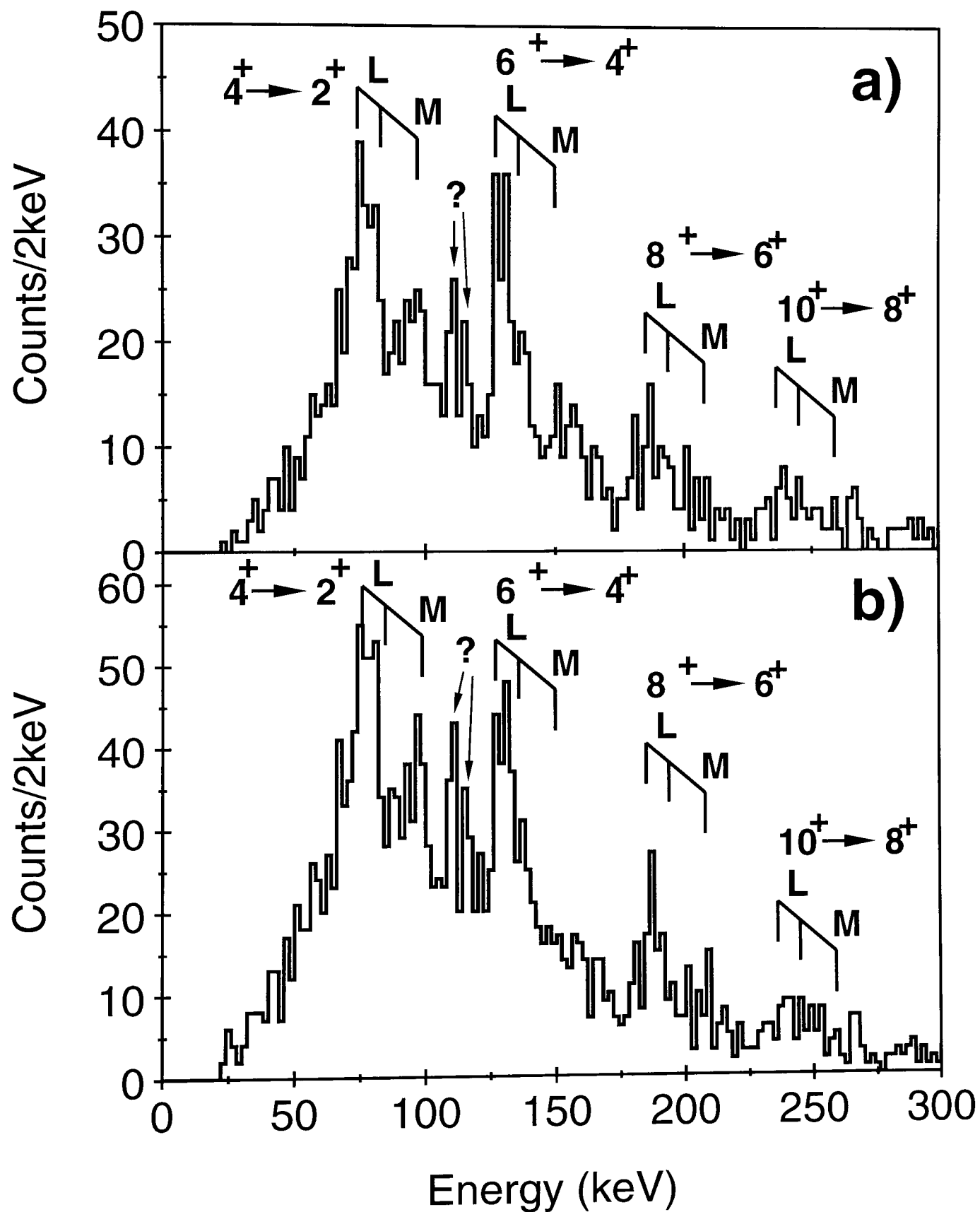
Figure 5.3: (a) Single fold electron energy spectrum in coincidence with ^{254}No recoils selected using the parallel plate gas detector. (b) Electron energy spectrum in coincidence with ^{254}No recoils selected using parallel plate gas detector. The unidentified peaks are
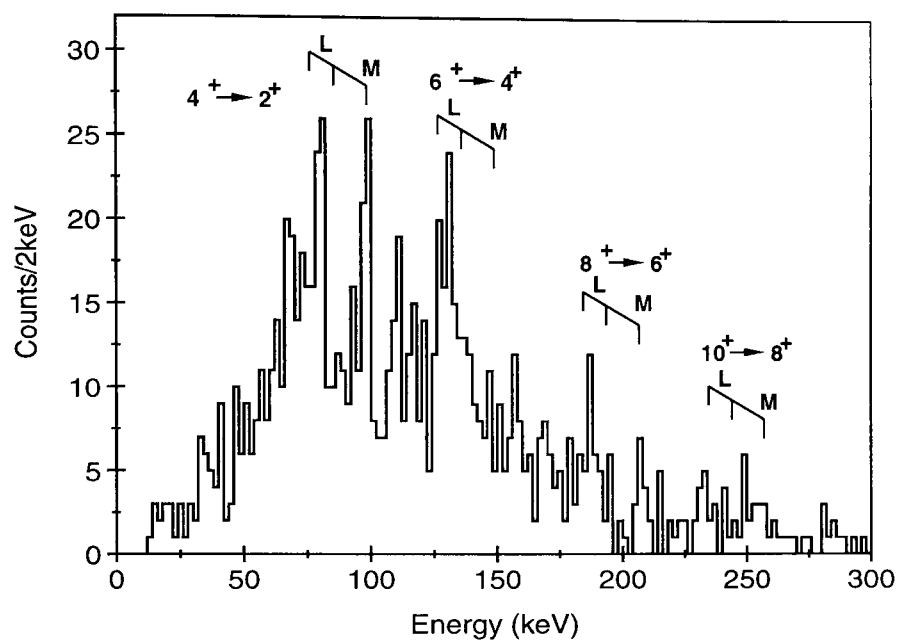
Figure 5.4: Electron energy spectrum tagged by the characteristic α-decay of ^{254}No .
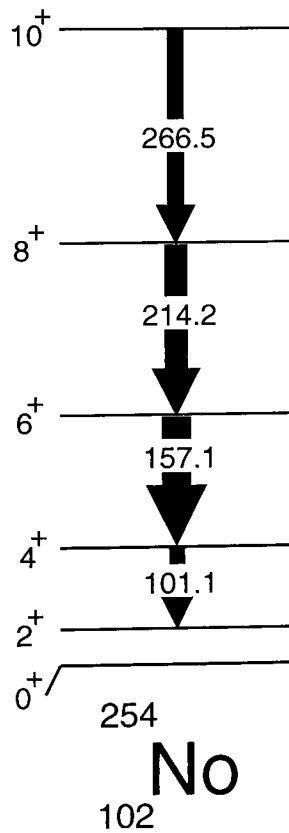
Figure 5.5: Ground state band level scheme obtained for ^{254}No.

include all L subshells.

An unidentified peak having an energy of ≈ 112 keV was observed in figure 5.3. The peak is within ≈ 6 keV of where the $10^+ \rightarrow 8^+$ K transition is expected. If the peak originated from the $10^+ \rightarrow 8^+$ K transition, an intensity of ≈ 16 counts would be expected, but the measured intensity (see table 5.4) is ≈ 70 and hence the origin of the major component lies elsewhere. It is possible that a component of this transition arose from a specific $M1$ transition in an isomeric high-$K(8^-)$ (see section 5.2.3) rotational band with the bandhead positioned at an excitation energy between the 8^+ and 10^+ levels of the yrast band. However, figure 5.6 suggests that the transition is in coincidence with the $4^+ \rightarrow 2^+$ transition in the ground state band with an intensity greater than that expected from the $10^+ \rightarrow 8^+$ K transition alone. Since coincidences between transitions above the isomeric bandhead and below it for the lifetimes involved are unlikely it seems more probable that the unknown transition feeds into the yrast band by a prompt transition.

In order to check the validity of the recoil gating used to obtain the data (see section 4.5), the RDT method was used to produce ^{254}No electron spectra. From the RDT electron spectrum in figure 5.4 it can be seen that the characteristic background is present along with the unidentified peak; validating the recoil gated electron spectra.

5.2.3   Background Features in ^{254}No

From inspection of the ^{254}No electron spectra in figure 5.3, it becomes apparent that there is a pronounced background centred at ≈ 100 keV. A comparison with the ^{226}U spectra in figure 5.1 shows the large difference in background counts, which if atomic could only arise from the differences in target and beam used. If the background is predominantly atomic in origin then one would expect a very different shape to the background than that observed. Figure 5.7 shows the electron spectra taken in random coincidence from the ^{254}No data. The maximum intensity of the random coincidence spectra is near to the high voltage barrier, which is the shape expected from
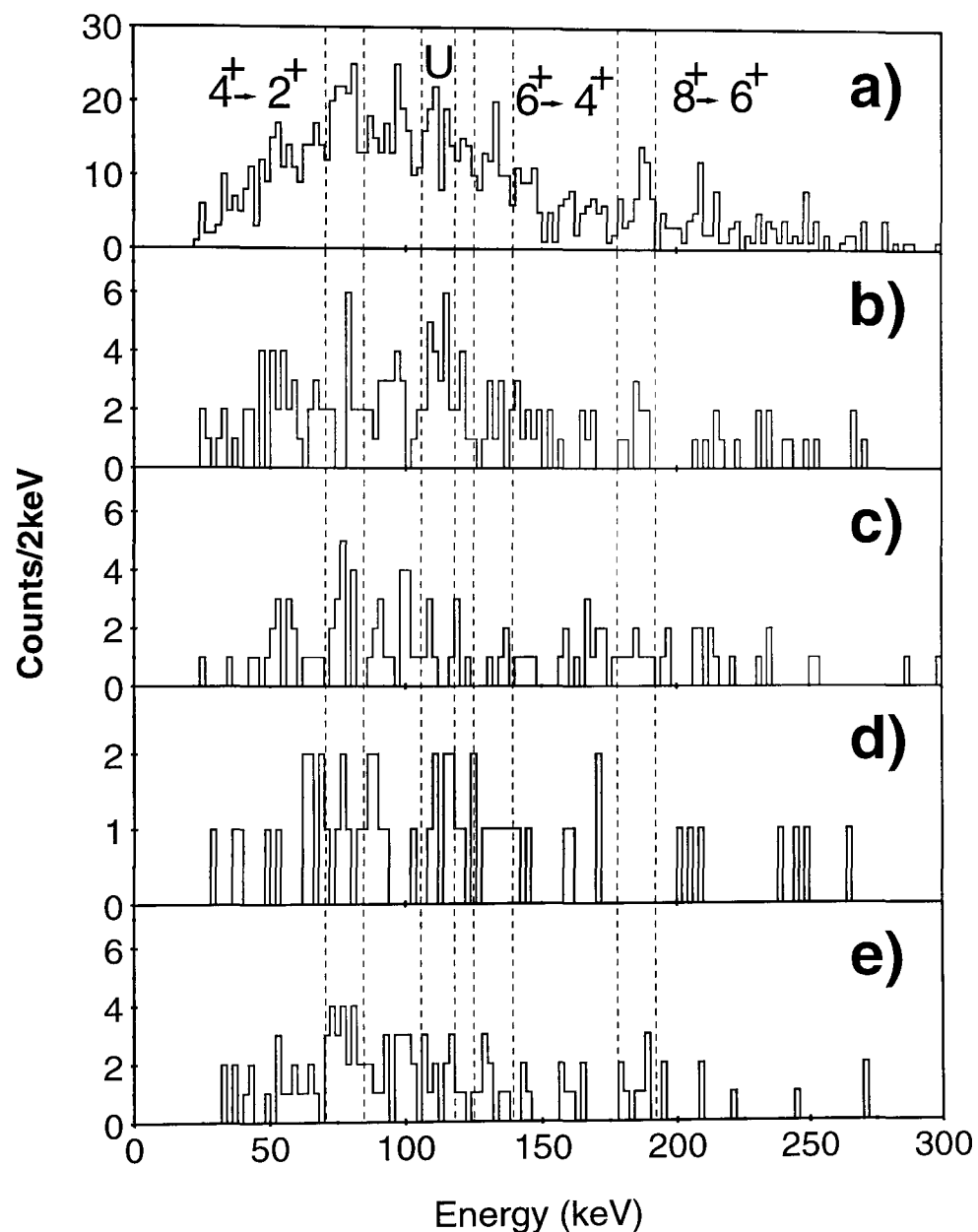
Figure 5.6: Panels (a) to (e) are ^{254}No recoil tagged e-e coincidence spectra. (a) The total projection of the coincident electron matrix. The dashed lines represent the gates set on the L electrons used to produce panels (b) to (e). (b) Electrons coincident with the $4^+ \rightarrow 2^+$ transition (first dashed gate in (a)). (c) Electrons coincident with the $6^+ \rightarrow 4^+$ transition (third dashed gate in (a)). (d) Electrons coincident with the $8^+ \rightarrow 6^+$ transition (fourth dashed gate in (a)). (e) Electrons coincident with the unidentified peak (second dashed line in (a)).

Table 5.3: Measured energies for ^{254}No. Column (a) lists the transition energies deduced here. Column (b) lists the transition energies observed by Leino *et al.* [Le 99]. Column (c) lists the transition energies observed by Reiter *et al.* [Re 99]. The energies marked with an asterisk * represent Harris parameter predictions.

$I_i^{\pi i}$	$I_f^{\pi f}$	$E_{L_{1,2}}$	E_{L_3}	E_M	E_γ (a)	E_γ (b)	E_γ (c)
4^+	2^+	73.15(3)	78.6(4)	94.6(8)	101.1(4)	102*	102*
6^+	4^+	128.6(3)	136.4(4)	152.0(4)	157.7(4)	158.9(3)	159.1(3)
8^+	6^+	185.9(4)	192.6(4)	206.1(8)	214.2(4)	214.1 (3)	214.1(2)
10^+	8^+	237.8(4)	245.6(5)	257.8(8)	266.5(6)	267.2(3)	267.3(3)
		112(1)					

delta electron background. A comparison of the random coincidence spectrum to the ^{254}No recoil gated electron spectrum background, shows that it is highly unlikely that the background is atomic in origin. Additional evidence can be obtained from comparisons between spectra taken for different thickness targets. The ^{254}No experiment was carried out with two different thickness targets 250 μg/cm^2 (4710 recoils) and 400 μg/cm^2 (2440 recoils). The background yield per ^{254}No recoil from the two targets was found to be very similar, 0.177 ± 0.008 and 0.170 ± 0.010 respectively. Delta electron background arising from atomic collisions between ^{254}No and Pb would be expected to increase with target thickness. The fact that the background yield was observed to remain almost constant with varying target thickness again points to the background being non atomic in origin.

If the background is not atomic in origin then another explanation of its origin is required. An interesting feature of the background is its multiplicity, which is much higher than the discrete transitions. A comparison of figures 5.3(a) and (b) demonstrates this. The peak to background is significantly improved in figure 5.3(a)

Table 5.4: Measured intensities for ^{254}No. The counts column are the sum of the actual L and M electron counts observed. Intensity column (a) lists the electron intensities corrected using the energy dependent absolute efficiency curve. Column (b) lists the electron intensities per 1000 recoils. Column (c) lists the total transition intensities corrected using tabulated values of internal conversion coefficients [Rö 78]. Column (d) lists the total transition intensities per 1000 recoils. Column (e) lists the transition intensities normalised to 100 for the 6$^+$ → 4$^+$ transition. Column (f) lists the transition intensities, from Leino *et al.* [Le 99], normalised to 100 for the 6$^+$ → 4$^+$ transition. The numbers marked with an Asterisk * represent measurements made for the ≈112 keV peak.

$I_i^{\pi_i}$	$I_f^{\pi_f}$	Counts	Intensity (a)	Intensity (b)	Intensity (c)	Intensity (d)	Intensity (e)	Intensity (f)
4$^+$	2$^+$	183(14)	2270(240)	320(30)	2340(250)	330(35)	122(13)	
6$^+$	4$^+$	175(15)	1610(160)	225(20)	1910(190)	270(30)	100(11)	100(32)
8$^+$	6$^+$	106(10)	1080(130)	150(20)	1560(180)	220(25)	81(9)	84(16)
10$^+$	8$^+$	54(7)	600(90)	80(10)	990(150)	140(20)	52(7)	72(13)
		70(8)*	660(70)*					
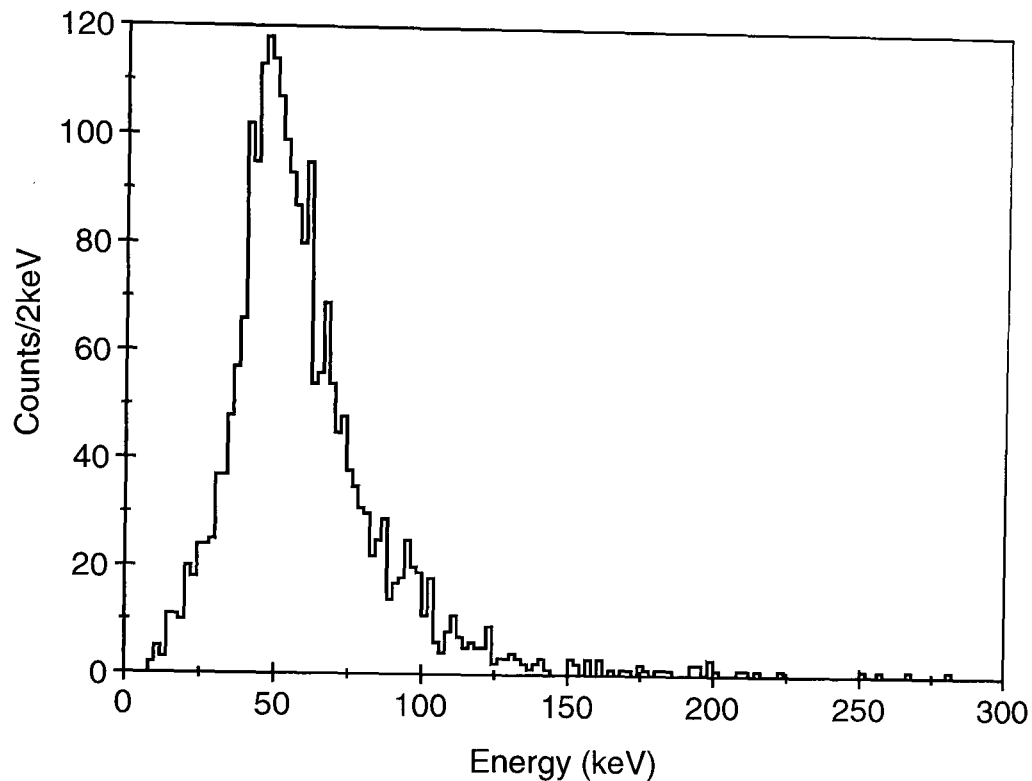
Figure 5.7: Electron spectrum to show shape of background which is atomic in origin. The spectrum is taken in random coincidence for ^{254}No .

where the spectrum is only incremented if no other electrons are detected in any of the SACRED pixels within 100 ns of the detection of the first electron. In order to estimate the mean electron multiplicity the SOLENOID Monte Carlo simulation code produced by Butler [Bu 92] was used as it is able to provide an accurate response model for the SACRED spectrometer. The model assumes only the ground state band is populated, there are no other sources of conversion electrons and the relative transition intensities used in the simulation of ^{254}No are taken from [Le 99], [Re 99]. The simulation was able to reproduce the characteristics of the SACRED detector with a good deal of success. In the simulation (see figure 5.8), carried out for 28,600 recoils[1], the values for the yield of the $6^+ \rightarrow 4^+$ transitions for any electron being detected and a single electron being detected give a ratio of $\mathcal{R}_{(6+\rightarrow4+)} = 0.84$, compared to a ratio of $\mathcal{R}_{(6+\rightarrow4+)} = 0.78 \pm 0.16$ measured from figures 5.3(a) and (b). If the only decay path is via the ground state band, then the known transitions including

---

[1]Four times the number of recoils recorded in the measurement

the undetected $2^+ \rightarrow 0^+$ transition give an average electron multiplicity of 3.7. The measurement of the observed yield is consistent with the simulation only if approximately 60% of the nuclei de-excite via that path, the remaining 40% de-exciting via isomeric states built on high K bandheads.

Having validated that the simulation can model observed ^{254}No spectra, it was then used to model the background. It was assumed the background arises from decays within a single rotational band built on a $K = 8$ isomeric bandhead, populated with the same entry spin distribution as that measured for all states by Reiter *et al.* [Re 00]. The value of g_K is taken to be 0 and $g_R = 0.3$. For this band it was assumed a constant moment of inertia of 100 $\hbar^2$ MeV^{-1}; this value was chosen to allow a better fit to the low energy part of the spectra even though it is slightly larger than the highest transitions in the ground state band. To account for the presence of many such bands having differing moments of inertia the electron energies were randomised by applying a Gaussian distribution of $\sigma = 10$ keV. The simulation was again run for 28,600 recoils and then renormalised by a factor of 0.10, see figure 5.9 (a) and (b).

The measured intensity of the background matches the calculated intensity, implying that approximately 40% of all detected recoils proceed through these paths. From section 2.5 it can be seen that the expected values of g_K for the lowest two quasiparticle $K^\pi = 8^-$ bands in ^{254}No are $\approx -0.3(\frac{9}{2}^-[734]_\nu \otimes \frac{7}{2}^+[613]_\nu$, ref.[SSS 91]), $0(\frac{9}{2}^-[734]_\nu \otimes \frac{7}{2}^+[624]_\nu)$ and $1(\frac{9}{2}^+[624]_\pi \otimes \frac{7}{2}^-[514]_\pi$, ref.[SSS 91]). Using these values of g_K in the SOLENOID simulation and the expression:

$$\mathcal{R} = \frac{\int N_{single}(E)dE}{\int N_{tot}(E)dE},$$

yields a ratio of $\mathcal{R}_{bkg} = 0.57 - 0.59$, which agrees with the measured value of 0.58 ± 0.03, while the mean electron multiplicity corresponding to these paths is in the range 7-8. The simulation was also run with $(g_K - g_R) = 0$ to investigate the effect of purely electric transitions on the background. A value of $\mathcal{R}_{bkg} = 0.64$ was obtained, corresponding to an electron multiplicity of 4 distributed evenly between $I \rightarrow I - 1$ and $I \rightarrow I - 2$ transitions. From figures 5.9 (a) and (b) it can be seen that in this case the calculated spectrum overestimates the high energy part of the spectrum. Finally,
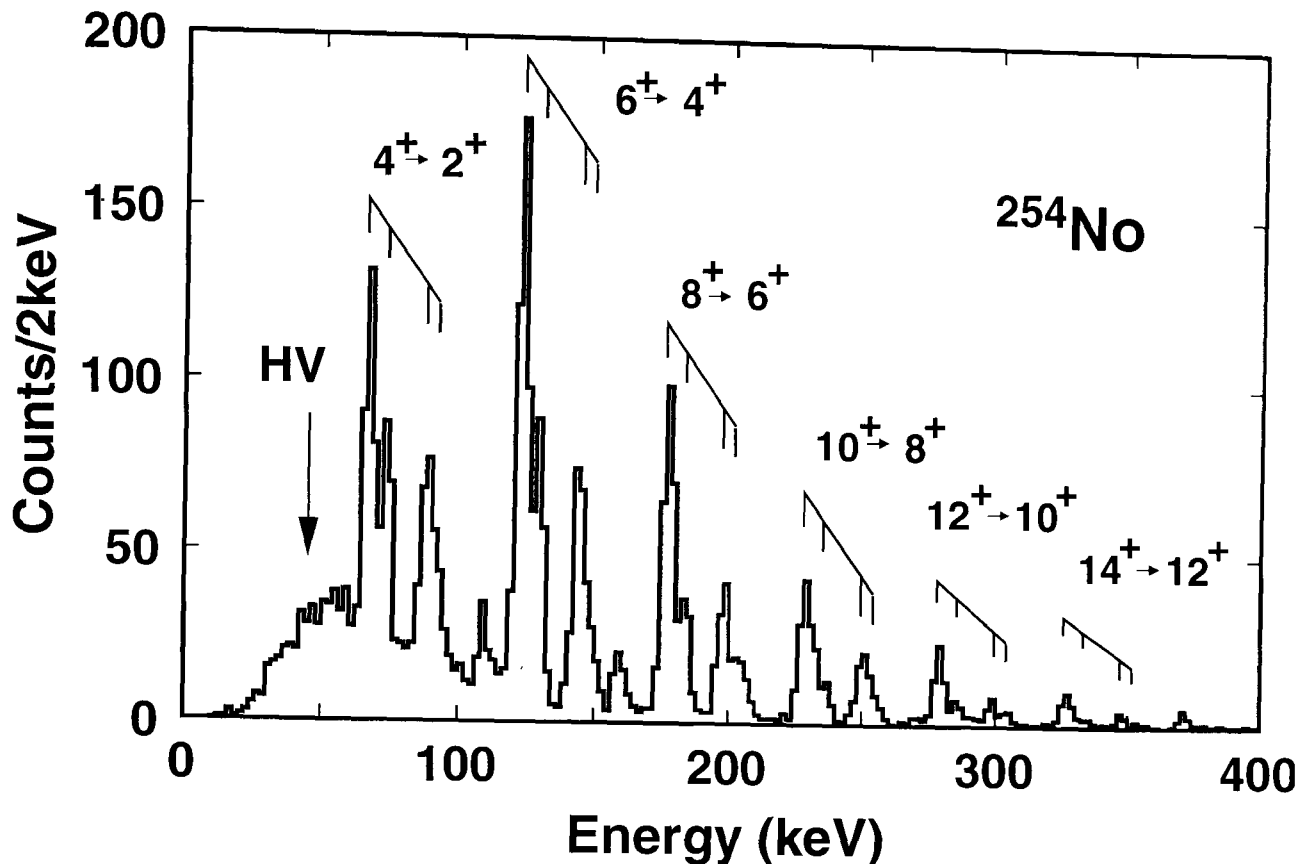
Figure 5.8: Simulation of the expected ground state band in ^{254}No illustrating the response of the detector [He 03].

if the simulation is set so that the $K = 8$ state decays immediately to the 8^+ member of the ground state band, then $\mathcal{R}_{bkg} = 0.47$ for a $g_K = 0$ and the corresponding electron multiplicity is 10. Further evidence to suggest that this feeding pattern is insignificant can be found in figure 5.9(b) (green line) which shows the spectrum of electrons in coincidence with a selected region of the background.

From these observations it is apparent that a large fraction ($\approx 40\%$) of the entry states in ^{254}No , populated in this reaction, decay via $M1$ cascades, and future entry distribution measurements should be modified to take this into account. No previous evidence of these cascades has been found in γ-ray arrays; although this is to be expected due to the strongly converting nature of $M1$ decays. The $M1$ cascades are expected to arise from the population of two-, four-, and many-quasiparticle excitations with isomeric high K-value bandheads. The lowest $K^{\pi} = 8^-$ bands, which
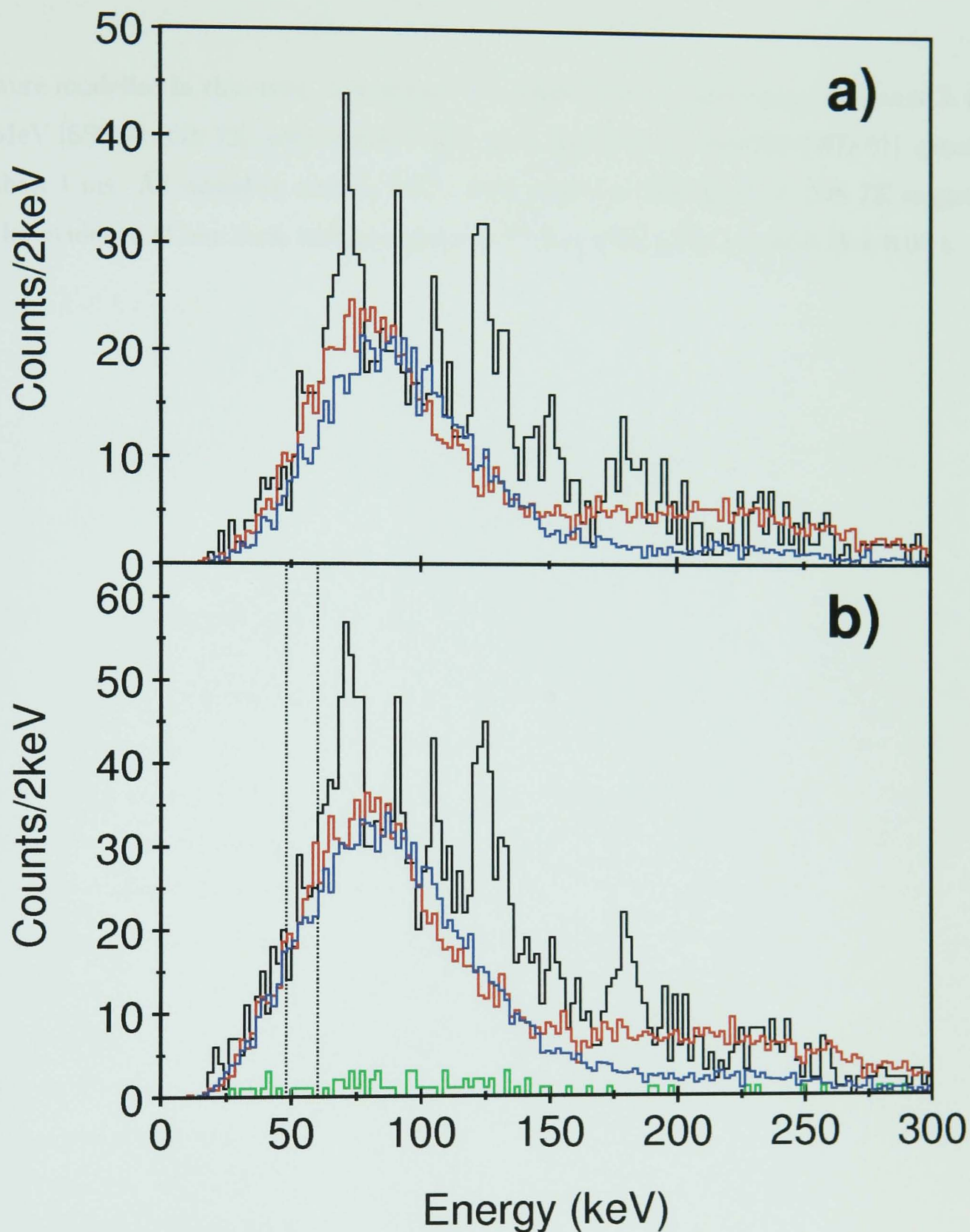
Figure 5.9: (a) The experimental conversion electron electron spectrum tagged by [254]No recoils corresponding to the detection of a single electron(black line). In this spectrum the energies are not corrected for Doppler shift. Also shown are the simulated spectra as described in the text for $g_K = 0$ (blue line) and for $g_K - g_R = 0$ (red line). (b): as (a) except that the experiment and simulation correspond to the detection of any number of electrons. The green line is a spectrum of a second electron in coincidence with a selected region between the dashed lines.

were modelled in this work, are expected to have an excitation energy of around 1-1.5 MeV [SSS 91, Gh 73], with isomeric lifetimes, based on systematics [WD 01], greater than 1 ms. As stated in section 5.2.1, work done by Ghiorso *et al.* [Gh 73] suggests the evidence of one such isomeric state in ^{254}No , with a lifetime of 0.28 ± 0.04 s.

Chapter 6

Summary and Future Prospects

6.1 Summary

The collinear geometry allowed conversion electrons to be detected with negligible Doppler broadening, and a smaller contribution from delta electrons than encountered with the previous SACRED geometry. These improvements enabled the conversion electrons to be measured with an in-beam resolution of ≈ 4 keV and at a peak absolute efficiency of ≈ 0.12 at an energy of ≈ 220 keV.

In-beam conversion electron measurements of super-heavy nuclei, with a cross section of ≈ 2 μb [It 98], have been undertaken, for the first time, using the new collinear geometry conversion electron spectrometer SACRED. Through its design to allow operation with the RITU gas-filled separator, recoil-tagging and recoil-decay-tagging techniques were utilised in identifying the hitherto measured $2^+ \rightarrow 0^+$ transition in ^{226}U and the $4^+ \rightarrow 2^+$ transition in ^{254}No, and used to confirm predictions for their respective partial level schemes; therefore, it seems likely that previously deduced deformation parameters remain unaffected. The ^{254}No experiment has shown evidence of a hitherto unseen transition, whose electron energies ≈ 112 keV, have been measured.

The ^{254}No experiment has also shown that a large fraction of the entry states, populated in this reaction, decay via $M1$ cascades that will not be detected in γ-ray

99

arrays, and measurements of entry distributions should be modified to take this into account. The $M1$ cascades will naturally arise from the population of two-, four-. and many-quasiparticle excitations that will often have bandheads with high K values. The lowest $K^\pi = 8^-$ bands are expected to be isomeric with life times greater than 1 ms and have an excitation energy of $\approx$ 1-1.5 MeV.

6.2   Future Prospects

A novel method of selecting summed internal conversion electron transitions following the decay of an isomer, correlated in position with an implanted recoil and its subsequent α-decay [Jo 02] can be used as an isomer tag, for coincidences with transitions above the isomeric bandhead. With isomer tagging of electrons it should be possible to examine $M1$ electron cascades in the high K rotational band in more detail. It should also be possible to isolate the transitions from the ground state band alone and remove the background from the transitions above the high K isomer. These spectra should give more insight into the structure of ^{254}No and more specifically; the origin of the previously unseen transition.

In the region of Cf, Fm and No there are single-particle high-K states near the Fermi energy level. As a result, K-isomeric states are expected in these nuclei; work done by Ghiorso *et al.* suggests evidence of a 1.8 ± 0.1 s isomer in ^{250}Fm. ^{250}Fm has recently been studied by Bastin *et al.* [Ba] using SACRED, and early results [Ba 03] suggest evidence of the background which characterised the $M1$ cascades observed in ^{254}No , in this work.

One of the main drawbacks of in-beam work regarding superheavy elements is their very low production cross-sections, which can be countered, in part, by improvements in spectroscopic technique. Some of ways in which SACRED could be improved are:

- Improve the resolution of the detector so that less prominent lines can be resolved and identified at lower statistics. These improvements could be made by redesigning the detector into more, smaller. pixels so that the capacitance

is reduced and also different manufacturing techniques which would allow the detector to be cooled below -20°C;

- Improve the efficiency of SACRED, especially at higher energies. This could again be achieved by redesigning the detector mask so that counting is distributed more evenly over the detector. The increased efficiency at higher energies could be brought about by increasing the current through the solenoid coils.

References

[Ak 01] Y.A. Akovali, Nucl. Data Sheets **94**, 131 (2001)

[Ak 95] Y.A. Akovali, Nucl. Data Sheets **76**, 457 (1995)

[Ar 85] P. Armbruster *et al.*, Phys. Rev. Lett. **54**, 406-9 (1985)

[Ar 98] A. Artna-Cohen, Nucl. Data Sheets **84**, 901 (1998)

[Ar 97] A. Artna-Cohen, Nucl. Data Sheets **80**, 157 (1997)

[Br 71] T.H. Braid, R.R. Chasman, J.R. Erskine, and A.M. Friedman, Phys. Rev. C **4**, 247 (1971)

[Ba 57] J. Bardeen, L.N. Cooper and J.R. Schrieffer, Phys. Rev. **108**, 1175 (1957)

[Ba] J.E. Bastin *et al.*, to be published

[Ba 03] J.E. Bastin, priv. comm.

[Be 03] M. Bender, P.-H. Heenen and P.-G. Reinhard, Rev. Mod. Phys. **75**, 121 (2003)

[Br 01] E. Browne, Nucl. Data Sheets **93**, 763 (2001)

[Br 92] E. Browne, Nucl. Data Sheets **65**, 669 (1992)

[Bo 58] A. Bohr, B.R. Mottelson and D. Pines, Phys. Rev. **110**, 936 (1958)

[Bo 82] R. Bock *et al.*, Nucl. Phys. A **388**, 344 (1982)

[Bu 92]   P.A. Butler, Monte Carlo code "SOLENOID" (1992)

[Bu 96]   P.A. Butler *et al.*, Nucl. Instr. Meth. A **381**, 433 (1996)

[BN 96]   P.A. Butler and W. Nazarewicz, Rev. Mod. Phys. **68**, 349 (1996)

[Bu 02]   P.A. Butler et al., Phys. Rev. Lett. **89**, 202501 (2002)

[CF 58]   B.L. Cohen and C.B. Fulmer, Nucl. Phys. **6**, 547 (1958)

[Ca 90]   R.F. Casten, Nuclear Structure from a Simple Perspective, Oxford Studies in Nuclear Physics (1990) p.91,130.

[Ca 98]   K.J. Cann, PhD thesis, University of Liverpool (1998)

[Cr 91]   J. Cresswell, "Event Format", EUROGAM Documentation (1991).

[Cw 87]   S. Cwiok, J. Dudek, W. Nazarewicz, W. Skalski and T. Werner, Comp. Phys. Comm. **46**, 379 (1987)

[Cw 96]   S. Cwiok *et al.*, Nucl. Phys. A **611**, 211 (1996)

[FN 72]   E.O. Fiset and J.R. Nix, Nucl. Phys. A **193**, 647 (1972)

[Gh 58]   A. Ghiorso *et al.*,Phys. Rev. Lett. **1**, 18 (1958)

[Gh 73]   A. Ghiorso *et al.*, Phys. Rev . C **7**, 2032 (1973)

[Gh 88]   A. Ghiorso *et al.*, Nucl. Instr. Meth. A **269**, 192 (1988)

[Gi67]   P.E. Gibbons *et al.*, Nucl. Instr. Meth. **53**, 1 (1967)

[Gr 98]   P.T. Greenlees *et al.*, J.Phys. G **24**, L63 (1998)

[Gr 03a]   P.T. Greenlees *et al.*, to be published

[Gr 03b]   P.T. Greenlees, priv. comm.

[HS 68]   R.S. Hager and E.C. Seltzer, Nucl. Data A **4**, 1 (1968)

[HJS 49]   O.Haxel, D. Jensen and H.E. Suess, Phys. Rev. **75**, 1766 (1949)

[He 02a]   R.-D. Herzberg *et al.*, Phys. Rev. C **65**, 014303 (2002)

[He 02b]   R.-D. Herzberg *et al.*, Proceedings of the International Conference Frontiers of Nuclear Structure, Berkeley, July 29 - Aug 2 (2002)

[He 03]   R.-D. Herzberg, Proceedings of the International Workshop XXXI on Gross Properties of Nuclei and Nuclear Excitations, Hirschegg, January 12 -18 (2003)

[Ho 78]   P.E. Hodgson, Nuclear Heavy-ion Reactions, Oxford University Press (1978)

[Ho 00]   S. Hofmann and G. Münzenberg Rev. Mod. Phys. **72**, 733 (2000)

[Hu 25]   A.W. Hull and N.H. Williams Phys. Rev. **25**, 147 (1925)

[It 98]   M. Itkis *et al.*, Nouv. Cim. **111**A, 783 (1998)

[Jo 28]   J.B. Johnson, Phys. Rev. **32**, 97 (1928)

[Jo 93]   P.M. Jones, SUN Library Code (1993)

[Jo 95]   P.M. Jones, PhD thesis, University of Liverpool (1995)

[Jo 02]   G.D. Jones Nucl. Instr. Meth. A **488**, 471 (2002)

[Ka 01]   H. Kankaanpää, PhD thesis, University of Jyväskylä (2001)

[Ka 95]   J. Kantele, *Handbook of Nuclear Spectroscopy*, Academic Press, New York (1995)

[KR 69]   B. Klank and R.A. Ristinen, Intern. Conf. on Radioactivity in nuclear spectroscopy (Nashville, 1969; J.H. Hamilton and J.C. Manthuruthill, eds.) pg.207.

[Kra 88]   K.S. Krane, Introductory Nuclear Physics. Wiley (1998) pg.345.

[Kru 00]   A.T. Kruppa *et al.*, Phys. Rev. C **61**, 034313 (2000)

[Ku 75]   V.A. Kuzminikh and S.A. Vorobiev, Nucl. Isnt. Meth. **129**, 561 (1975)

[La 69]   A. Lauber *et al.*, Nucl. Instr. Meth. **75**, 297 (1969)

[Le 95]   M. Leino *et al.*, Nucl. Instr. Meth. B **99**, 653 (1995)

[Le 99]   M. Leino *et al.*, eur. Phys. J. A **6**, 63 (1999)

[LL 75]   T. Lindbald and C.G. Lindén, Nucl. Instr. Meth. **126**, 397 (1975)

[Lö 68]   K.E.G. Löbner., Phys. Lett. B **26**, 369 (1968)

[Ma 49]   M.G. Mayer, Phys. Rev. **75**, 1969 (1949)

[McPh 92] G.M. McPherson *et al.*, IEEE Trans. Nucl. Sci. **39**, 886 (1992)

[Mö 94]   P.Möller and J.R. Nix, J. Phys. G **20**, 1681 (1994)

[MS 66]   W.D. Myers and W.J. Świątecki, Nucl. Phys. **81**, 1 (1966)

[Na 85]   W. Nazarewicz, J. Dudek, R. Bengtsson and I. Ragnarsson, Nucl. Phys. A **435**, 397 (1985)

[Ni 55]   S.G. Nilsson, Kgl.Danske Videnskab.Selskab, Mat. -fys. Medd. **29**, No.16 (1955)

[Ni 68]   S.G. Nilsson *et al.*, Nucl. Phys. A **115**, 545 (1968)

[Ni 69]   S.G. Nilsson *et al.*, Nucl. Phys. A **131**, 1 (1969)

[Ny 28]   H. Nyquist, Phys. Rev. **32**, 110 (1928)

[Og 78]   Yu. Ts. Oganessian *et al.*, Nucl. Phys. A **294**. 213 (1978)

[Og 91]   Yu. Ts. Oganessian *et al.*, JINR LNR Scientific Report. 158 (1991)

[Og 01]   Yu. Ts. Oganessian *et al.*, Phys. Rev. C **64**. 054606 (2001)

[Pa 03]   T. Page, priv. comm.

[Pa 95]   E.S. Paul *et al.*, Phys. Rev. C **51**, 78 (1995)

[Pe 60]   E.M. Pehl, J. Appl. Phys. **31**, 291 (1960)

[Ra 76]   J. Randrup *et al.*, Phys. Rev. C **13**, 229 (1976)

[Re 99]   P. Reiter *et al.*, Phys. Rev. Lett. **82**, 509 (1999)

[Re 00]   P. Reiter *et al.*, Phys. Rev. Lett. **84**, 3542 (2000)

[Ro 58]   M.E. Rose, "Internal Conversion Coefficients", North-Holland (1958)

[Ro 66]   M.E. Rose, "Alpha-, Beta- and Gamma-Ray Spectroscopy", **Ch. XVI**, Norht-Holland (1966)

[Rö 78]   F. Rösel *et al.*, At. Data Nucl. Data Tables **21**, 91 (1978)

[Ru 97]   K. Rutz *et al.*, Phys. Rev. C **56**, 238 (1997)

[Sh 79]   K.H. Schmidt *et al.*, Nucl. Phys. A **318**, 253 (1979)

[Sh 85]   E.N. Shurshikov *et al.*, Nucl. Data Sheets **45**, 509 (1985)

[Sh 87]   W.Q. Shen *et al.*, Phys. Rev. C **36**, 115 (1987)

[Si 86]   R.S. Simon *et al.*, Z. Phys. A **325**, 197 (1986)

[Sm 95]   R. Smolanczuk *et al.*, Phys. Rev. C **52**, 1871 (1995)

[So 94]   A. Sobiczewski, Phys. Part. Nuclei **25**, 119 (1994)

[SSS 91] V.G. Solov'ev, A.V. Sushkov and N.Yu. Shirikova, Sov. J. Nucl. Phys. **54**, 748 (1991)

[St 67]   V.M. Strutinsky, Nucl. Phys. A **95**, 420 (1967)

[Tr 90]   W.H. Trzaska, Nucl. Instr. Meth. A **297**, 223 (1990)

[Uu 96]   J. Uusitalo, Ph.D. Thesis, University of Jyväskylä (1996)

[Ve 73]   V.E. Viola, Jr., M.M. Minor and C.T. Roche, Nucl. Phys. A **217**, 372 (1973)

[Wa 94]   P.M. Walker, G.D. Dracoulis, A.P. Byrne, B. Fabricius, T. Kibedi, A.E. Stuchberry and N. Rowley, Nucl. Phys. A **568**, 397 (1994)

[WD 01]   P. Walker and G. Dracoulis, Hyper. Int. **135**, 83 (2001)

[WK 87]   P.J.Van Wijnen and W.R.Th. Ten Kate, Nucl. Instr. Meth. A **253**, 351 (1987)

[WS 54]   R.D. Woods and D.S. Saxon, Phys. Rev. **95**, 577 (1954)

[Ye 94]   A.V. Yeremin *et al.*, Nucl. Instr. Methods A **350**, 608 (1994)

[Za 01]   V.J. Zagrebaev *et al.*, Phys. Rev. C **65**, 014607 (2001)